



# Contribution to the modeling of densification in silicate glasses under very high pressures

Ji Xing Meng

## ► To cite this version:

Ji Xing Meng. Contribution to the modeling of densification in silicate glasses under very high pressures. Other [cond-mat.other]. Université de Rennes, 2013. English. NNT : 2013REN1S116 . tel-01184925

**HAL Id: tel-01184925**

**<https://theses.hal.science/tel-01184925>**

Submitted on 18 Aug 2015

**HAL** is a multi-disciplinary open access archive for the deposit and dissemination of scientific research documents, whether they are published or not. The documents may come from teaching and research institutions in France or abroad, or from public or private research centers.

L'archive ouverte pluridisciplinaire **HAL**, est destinée au dépôt et à la diffusion de documents scientifiques de niveau recherche, publiés ou non, émanant des établissements d'enseignement et de recherche français ou étrangers, des laboratoires publics ou privés.



**THÈSE / UNIVERSITÉ DE RENNES 1**  
*sous le sceau de l'Université Européenne de Bretagne*

pour le grade de  
**DOCTEUR DE L'UNIVERSITÉ DE RENNES 1**

*Mention : MÉCANIQUE*

**Ecole doctorale Sciences de la Matière**

présentée par

**Ji Xing MENG**

Préparée à l'unité de recherche LARMAUR ERL CNRS 6274  
Laboratoire de Recherche en Mécanique Appliquée  
de SPM Université de Rennes 1

---

**Contribution à la  
modélisation de la  
densification des  
verres silicatés sous  
très hautes pressions**

**Thèse soutenue à Rennes  
le 15 Juillet 2013**

devant le jury composé de :

**Eric LE BOURHIS**

Professeur, Université de Poitiers/  
Rapporteur

**Yann MARCO**

Maître de Conférences, HDR, ENSTA  
Bretagne/ Rapporteur

**Jean-Christophe SANGLEBOEUF**

Professeur, Université de Rennes 1/  
Examineur

**Ludovic CHARLEUX**

Maître de Conférences, Université de  
Savoie/ Examineur

**Jean-Pierre GUIN**

CR CNRS, Université de Rennes 1/  
Co-directeur de thèse

**Vincent KERYVIN**

Professeur, Université de Bretagne-Sud/  
Directeur de thèse



# ACKNOWLEDGEMENT

I would like to express my gratitude to all those who gave me the possibility to complete this degree. Thanks to my laboratory LARMAUR, Laboratoire de Recherche en Mécanique Appliquée de l'Université de Rennes 1, and laboratory LIMATB, Laboratoire d'Ingénierie des Matériaux de Bretagne De l'Université de Bretagne-Sud.

First and foremost I offer my sincerest gratitude to my supervisor, Prof. Vincent KERYVIN, who has supported me throughout my thesis with his patience and knowledge. Thank you for always helping me see the positive or negative sides and outcomes of my work, even when simulations were not going as planned. It was a privilege to work with such an excellent mentor, and a good friend as well.

I would like to thanks my co-supervisor, Prof. Philippe PIVLIN and Dr. Jean-Pierre GUIN. Thank you for your great help and encouragement when I face difficulties. Thanks to Prof. Jean-Christophe SANGLEBOEUF, who offered me great help to cover the tough things to go on my study in Rennes and Lorient. Thanks to Prof. Tanguy ROUXEL for your great help to start my research work in France and thanks for your kind advice and helpful discussions.

I would like to thank my PH.D. defence committee, including Prof. Eric LE BOURHIS and Prof. Yann MARCO, who served as rapporteurs and as well as Prof. Jean-Christophe SANGLEBOEUF who served as examiners, and my director Prof. Vincent KERYVIN and Co-director Dr. Jean-Pierre GUIN.

Since I have spent three and half years in France, one year in Rennes and two and half years in Lorient. I can not forget to thank Prof. Ludovic CHARLEUX, Mr. Eric ROBIN, Mr. Vincent BURGAUD, Ms. Dainele de MOREL, Prof. Hongli MA, Dr. Yifan NIU, Dr. Kun HAN, Dr. Guang YANG, Dr. Yann GUEGUEN, Dr. Pathikumar SELLAPPAN, Dr. Phillipe BRAMMER, Dr. Madina TCHIKOU, Dr. Charbel MOUSSA, Ngoc-Hiep LE, and Dr. Lu CHEN, Bin LI, Bo FAN, Bai XUE, Dr. Peng ZHANG, Dr. Yang ZENG, Dr. Qi ZHAO and everyone at university of Rennes 1 for their help or guidance. I would like to thanks Prof. Pierre-Yves Manach, Prof. Vincent Picandet, Dr. Javier RODRIGUEZ GARCIA, Dr. Faiza BOUMEDIENE, Dr. Khelifi HAMID, Dr. Yann GUEVEL and Pierre TRONET, Anthony JEGAT, Jean-Sébastien Brest and everyone from LIMATB of University of Bretagne-Sud, for their great help and guidance.

Finally I would especially like to thank my wife Xiao-Ning MO, for her encouragement, friendship and love, my parents and my parents in law for their love and support over years. Thanks to all of my family members. Thank you very much for your sincerely love and support!

# Table of Contents

<b>Table of Contents.....</b>	<b>v</b>
<b>List of Tables.....</b>	<b>viii</b>
<b>List of Figures.....</b>	<b>ix</b>
<b>Résumé long du manuscrit.....</b>	<b>xii</b>
<b>Introduction.....</b>	<b>xvii</b>

## Chapter 1

<b>Densification Mechanism in Glasses: A Review.....</b>	<b>1</b>
<b>Contents.....</b>	<b>3</b>
<b>1.1 Introduction.....</b>	<b>4</b>
<b>1.2 Glass composition and structures.....</b>	<b>5</b>
1.2.1 Silica Glass.....	5
1.2.2 Silicate glasses.....	7
1.2.3 Boric oxide glass.....	7
1.2.4 Germanate glasses.....	8
1.2.5 Chalcogenide and chalcahalide glasses.....	8
1.2.6 Bulk metallic glasses.....	8
<b>1.3 Densification experiments.....</b>	<b>10</b>
1.3.1 Densification under high-pressure.....	11
1.3.1.1 <i>Definition of densification</i> .....	11
1.3.1.2 <i>Archimedes methods for measuring density</i> .....	11
1.3.1.3 <i>Techniques of high-pressure</i> .....	12
1.3.1.4 <i>Densification behavior under high-pressure</i> .....	16
1.3.2 Indentation and Densification.....	24
1.3.2.1 <i>Indentation and Cracks</i> .....	24
1.3.2.2 <i>Quantitative evaluation of indentation-induced densification</i> .....	25
1.3.3 Shock Wave Compression and Structure.....	26
1.3.3.1 <i>Densification and shock compression</i> .....	26

1.3.3.2 First sharp diffraction peak study.....	27
<b>1.4 Densification and materials' properties.....</b>	<b>29</b>
1.4.1 Sound velocities and refractive index.....	29
1.4.2 Bulk modulus, elastic modulus and shear modulus.....	30
1.4.3 Poisson's ratio and the high pressure densification.....	33
1.4.4 Densification and Raman spectroscopy.....	35
<b>1.5 Modeling of densification.....</b>	<b>37</b>
1.5.1 Molecular-dynamic simulation.....	37
1.5.2 Finite element method (FEM).....	37
<b>1.6 Discussion and prospect.....</b>	<b>42</b>
1.6.1 Effect of time and temperature .....	42
1.6.2 Intermediate-range order interpretation.....	42
<b>1.7 Summary.....</b>	<b>44</b>
<b>References.....</b>	<b>46</b>

## Chapter 2

### Deformation Model of Silica Glass under Hydrostatic Pressure.....53

<b>Contents.....</b>	<b>55</b>
<b>2.1 Introduction.....</b>	<b>56</b>
<b>2.2 Hydro pressure experiments.....</b>	<b>56</b>
2.2.1 In-situ hydro-static experiments.....	58
2.2.2 ex-situ hydro-static experiments.....	61
2.2.3 Extracting data from literature sources.....	62
<b>2.3 Models.....</b>	<b>72</b>
2.3.1 Deformation process.....	72
2.3.2 Constitutive equations (small strain).....	73
2.3.2.1 Yield function.....	73
2.3.2.2 Flow rule.....	75
2.3.3 Implementation.....	78
2.3.3.1 Numerical model.....	78
2.3.3.2 Co-rotational framework.....	78
2.3.4 Verification.....	80
<b>2.4 Identification and numerical results.....</b>	<b>84</b>
2.4.1 Numerical tools .....	84

2.4.2 Strategy of identification.....	84
2.4.3 Assumptions and results.....	85
2.4.3.1 <i>Linear assumption and results</i> .....	85
2.4.3.2 <i>Atan(<math>P</math>) function assumption and Results</i> .....	94
2.4.3.3 <i>Avrami equation assumption and Results</i> .....	101
<b>2.5 Conclusion and discussion.....</b>	<b>109</b>
<b>References.....</b>	<b>115</b>
 <b>Conclusion.....</b>	 <b>116</b>



# List of Tables

<b>Table 1.1</b> Single Bond Strength for Oxides.....	6
<b>Table 1.2</b> Composition and basic properties of inorganic glasses.....	6
<b>Table 1.3</b> Densification research progress from 1950s-2010s.....	10
<b>Table 1.4</b> Experimental Data for Glasses.....	20
<b>Table 1.5</b> Summary of models in densification.....	41
<b>Table 2.1</b> In-situ experiments' data and its derivative.....	66
<b>Table 2.2</b> In-situ experiments' data of fully densified silica.....	68
<b>Table 2.3</b> Ex-situ hydrostatic experiments data.....	70
<b>Table 2.4</b> Simulation results of in-situ experiments.....	85
<b>Table 2.5</b> Simulation results of ex-situ experiments.....	89
<b>Table 2.6</b> Reverse analysis results basing on linear hardening rule.....	92
<b>Table 2.7</b> Reverse analysis results basing on Atan(P) hardening rule.....	100
<b>Table 2.8</b> Reverse analysis results basing on JMAK hardening rule.....	108
<b>Table 2.9</b> Reverse analysis results.....	114

# List of Figures

<b>Figure 1.1</b> (a) Atomic structures representation of $\text{SiO}_2$ glass. (b) Basic unit of $\text{SiO}_2$ . (c) Definition of the bond angle $\beta$ and the torsion angles $\alpha_1$ and $\alpha_2$ .....	5
<b>Figure 1.2</b> (a) Configuration of the boroxol ring. (b) Three-dimensional representation of the random network model of the structure of $\text{B}_2\text{O}_3$ glass consisting of $\text{B}_3\text{O}_6$ boroxol groups and $\text{BO}_3$ triangles. B and O atoms are shown as red and turquoise, respectively.....	7
<b>Figure 1.3</b> Presentation of structure: (a) Normal crystal metals and (b) Bulk metallic glass...	9
<b>Figure 1.4</b> Density gradient method slowly miscible liquids with different Densities .....	12
<b>Figure 1.5</b> (a) Schematic diagram of compression apparatus. S- specimen; C- Carbology inserts. (b) Schematic of anvil assembly. (c) High pressure alumina cell “belt” densification apparatus. (d) High pressure silver chloride cell “belt” densification apparatus.....	13
<b>Figure 1.6</b> (a) The high pressure testing machine and the multi-stage loading set-up used to insure pure hydrostatic loading. (b) Schematic experimental setup at X17B2, NSLS, for simultaneous pressure-volume-temperature equation-of-state and sound-velocity measurement. The thick arrows indicate the top and bottom anvils that can be advanced or retracted to minimize stress.....	15
<b>Figure 1.7</b> Relative increase of density of glasses.....	16
<b>Figure 1.8</b> Hydrostatic pressure compression below 10 GPa.....	17
<b>Figure 1.9</b> Pressure dependence of density of $\text{SiO}_2$ glass.....	18
<b>Figure 1.10</b> Pressure dependence of the density of fully densified $\text{SiO}_2$ glass at room temperature.....	19
<b>Figure 1.11</b> Densification under high pressure.....	22
<b>Figure 1.12</b> Schematic illustration of the procedure for measuring the indentation volume before and after annealing.....	25
<b>Figure 1.13</b> Raman spectra of densified silica glasses after single shock reverberations. Values next to sample numbers are peak pressures in GPa during shock loadings and densities in $\text{Mg/m}^3$ after loadings.....	27
<b>Figure 1.14</b> Structure factor, $S(Q)$ , of silica glass at various pressures measured during decompression together with those 8.5 GPa and 10.9 GPa.....	28
<b>Figure 1.15</b> Sound velocities in $\text{SiO}_2$ glass as a function of pressure.....	30
<b>Figure 1.16</b> Variations with pressure, closed symbols for loading and open symbols for unloading for $\text{GeSe}_2$ . (a) $V_p$ , (b) $V_s$ , (c) Poisson’s ratio and (d) elastic moduli.....	31

<b>Figure 1.17</b> Poisson's ratio of SiO <sub>2</sub> glass as a function of pressure. Black square are increasing pressure and red circles are on decreasing pressure.....	33
<b>Figure 1.18</b> The maximum densification and Poisson's ratio among different inorganic glasses.....	33
<b>Figure 1.19</b> Raman shift and densification under pressure in SiO <sub>2</sub> glass at room temperature. Solid symbols are Raman shift data and open symbols are densification data from relevant published articles.....	35
<b>Figure 1.20</b> Constitutive model for the densification of fused silica.....	38
<b>Figure 1.21</b> Comparing load-displacement curves for different $\alpha$ and Y. (a) for small $\alpha$ at Y=4.04 GPa; (b) for large $\alpha$ at Y=4.04 GPa; (c) for different Y at $\alpha=0.06$ ; (d) fitting to indentation data.....	39
<b>Figure 1.22</b> Elliptic yield criterion for amorphous silica. $p$ denotes the pressure, $p_c$ denotes the threshold of densification pressure, $q$ denotes the equivalent shear stress in compression ( $\sqrt{3}\tau_e$ ), $q_c$ denotes the critical threshold of equivalent shear stress.....	40
<b>Figure 1.23</b> Densification map: left, experiment results; right, finite element results.....	40
<b>Figure 1.24</b> Schematic of tetrahedral network of GeO <sub>2</sub> glass with corner shared GeO <sub>4</sub> tetrahedral units. The arrows show the bending of the Ge-O-Ge angles and rotation of the tetrahedral used to produce the densified structure.....	43
<b>Figure 1.25</b> Continues and non-continues densification processes.....	44
 <b>Figure 2.1</b> Comparison of pressure-density measurements for SiO <sub>2</sub> glass below 10 GPa.....	62
<b>Figure 2.2</b> In-situ compression experiments of SiO <sub>2</sub> glass: Density changes with hydro-static pressure.....	63
<b>Figure 2.3</b> Hydrostatic in-situ experiments data: a) pressure vs density; b) pressure vs volume changes; c) pressure vs relative displacement; d) pressure vs loading time.....	67
<b>Figure 2.4</b> In-situ experiments' data: pressure vs relative density. Green square (Pristine sample, Sato et al.); Red point (Fully densified sample, Wakabayashi et al.); Blue dot line (linear fit fully densified data); Pink dash dot line (estimate the start pressure where blue dot line meets Sato's data).....	69
<b>Figure 2.5</b> Ex-situ experiments: Permanent densification vs hydro-static pressure. Densification error is $\pm 0.05\%$ . The first black dot vertical line (left) shows where densification begin; the right black dot line shows where the saturation may begin; blue dash line show the tendency of saturation of densification.....	70
<b>Figure 2.6</b> Elastic properties change with hydro-static pressure. Black square--Young's modulus; red point--bulk modulus; blue triangle--hear modulus.....	71

<b>Figure 2.7</b> Deformation behavior of silica under high pressure.....	72
<b>Figure 2.8</b> Illustration of pure hydro-static pressure deformation model.....	75
<b>Figure 2.9</b> A sketch of co-rotation frame.....	79
<b>Figure 2.10</b> Simple tension test: stress vs strain.....	80
<b>Figure 2.11</b> Simple tension test: densification vs tensile stress.....	81
<b>Figure 2.12</b> Simple shear test: stress vs strain.....	81
<b>Figure 2.13</b> Simple shear test: densification vs von Mises shear stress.....	82
<b>Figure 2.14</b> Simple compression test: stress vs strain.....	82
<b>Figure 2.15</b> Simple compression test: densification vs compressive stress.....	83
<b>Figure 2.16</b> The sketch of identification process.....	84
<b>Figure 2.17</b> Linear assumption of densification.....	85
<b>Figure 2.18</b> Hydrostatic pressure test: Pressure vs Volumes change. Simulation (loading and unloading) vs experiments (Sato, pristine sample; Wakabayashi, fully densified sample).....	86
<b>Figure 2.19</b> Hydrostatic pressure test: Pressure vs Densification.....	86
<b>Figure 2.20</b> Hydrostatic pressure test: Predictions of elastic moduli with pressure.....	87
<b>Figure 2.21</b> Hydrostatic pressure test: Predictions of Poisson's ratio with pressure.....	88
<b>Figure 2.22</b> Hydrostatic pressure test: Jacobian vs Applied pressure.....	88
<b>Figure 2.23</b> Reverse analysis: (a) Pressure vs time; (b) Densification vs Time.....	89
<b>Figure 2.24</b> Densification at different maximum pressure (8 GPa, 12 GPa, 20 GPa, and 25 GPa, corresponding to Ji's experimental data).....	90
<b>Figure 2.25</b> Hydrostatic pressure test: Densification vs Maximum applied pressure (Ji's experimental data, error is $\pm 0.005$ ), Euler framework.....	91
<b>Figure 2.26</b> Hydrostatic pressure test: Elastic moduli vs Maximum applied pressure (Ji's experimental data).....	91
<b>Figure 2.27</b> Hydrostatic pressure test: Poisson's ratio vs Maximum applied pressure (Ji's experimental data).....	92
<b>Figure 2.28</b> The changes of moduli vs densification.....	93
<b>Figure 2.29</b> Illustration of Atan (P) assumption.....	94
<b>Figure 2.30</b> Use Atan (P) function to fit Ji's permanent densification vs pressure.....	94
<b>Figure 2.31</b> Hydrostatic pressure test: Pressure vs Volumes change. Simulation (loading and unloading) vs experiments (Sato, pristine sample; Wakabayashi, fully densified sample).....	95
<b>Figure 2.32</b> Hydrostatic pressure test: Pressure vs Densification.....	95
<b>Figure 2.33</b> Hydrostatic pressure test: Predictions of elastic moduli with pressure.....	96
<b>Figure 2.34</b> Hydrostatic pressure test: Predictions of Poisson's ratio with pressure.....	97
<b>Figure 2.35</b> Hydrostatic pressure test: Jacobian vs Applied pressure.....	97
<b>Figure 2.36</b> Densification at different maximum pressure (Atan(P) assumption. 8 GPa, 12 GPa, 20 GPa, and 25 GPa, corresponding to Ji's experimental data).....	98
<b>Figure 2.37</b> Hydrostatic pressure test: Densification vs Maximum applied pressure (Ji's experimental data, error is $\pm 0.005$ ).....	99
<b>Figure 2.38</b> Hydrostatic pressure test: Elastic moduli vs Maximum applied pressure.....	99
<b>Figure 2.39</b> Hydrostatic pressure test: Poisson's ratio vs Maximum applied pressure, Euler framework.....	100

<b>Figure 2.40</b> Avrami type plots.....	101
<b>Figure 2.41</b> Hydrostatic pressure test: Pressure vs Volumes change. Simulation (loading and unloading) vs experiments (Sato, pristine sample; Wakabayashi, fully densified sample).....	102
<b>Figure 2.42</b> Hydrostatic pressure test: Pressure vs Densification.....	103
<b>Figure 2.43</b> Hydrostatic pressure test: Elastic moduli vs Pressure.....	103
<b>Figure 2.44</b> Hydrostatic pressure test: Predictions of Poisson's ratio with pressure.....	104
<b>Figure 2.45</b> Hydrostatic pressure test: Jacobian vs pressure.....	104
<b>Figure 2.46</b> Densification at different maximum pressure (8 GPa, 12 GPa, 20 GPa, and 25 GPa, corresponding to Ji's experimental data).....	105
<b>Figure 2.47</b> Hydrostatic pressure test: Densification vs Maximum applied pressure (Ji's experimental data, error is $\pm 0.005$ ).....	106
<b>Figure 2.48</b> Hydrostatic pressure test: Elastic moduli vs Maximum applied pressure (Ji's experimental data).....	106
<b>Figure 2.49</b> Hydrostatic pressure test: Poisson's ratio vs Maximum applied pressure.....	107
<b>Figure 2.50</b> Elastic moduli vs densification.....	107
<b>Figure 2.51</b> Poisson's ratio vs densification.....	108
<b>Figure 2.52</b> Hydrostatic pressure test: Volume changes vs Pressure.....	109
<b>Figure 2.53</b> Hydrostatic pressure test: Densification changes vs Pressure.....	110
<b>Figure 2.54</b> Hydrostatic pressure test: Bulk modulus changes vs Pressure.....	110
<b>Figure 2.55</b> Hydrostatic pressure test: Shear modulus changes vs Pressure.....	111
<b>Figure 2.56</b> Hydrostatic pressure test: Young's modulus changes vs Pressure.....	112
<b>Figure 2.57</b> Hydrostatic pressure test: Poisson's ratio changes vs Pressure.....	112
<b>Figure 2.58</b> Hydrostatic Pressure Case: Densification and Raman shift change with pressure.....	113
<b>Figure 2.59</b> Percentages of Si atoms coordinated four (squares), five (circles), and six (triangles), to oxygen. The cutoff distance for coordination was set to 2.1 Å and error bars were evaluated by changing the cutoff distance by $\pm 0.1$ Å.....	113

# Résumé long du manuscrit

En raison de leur compacité atomique relativement faible par rapport à leurs homologues cristallins, les verres subissent une densification significative (augmentation permanente de la densité) sous des pressions hydrostatiques élevées.

En effet, la densité de la silice amorphe peut être augmentée de 20 % et celle du verre à vitre de 6 %, quand une pression suffisamment élevée est appliquée.

Les modifications permanentes de la densité des verres silicatés ne sont en général pas accessibles *via* des essais mécaniques macroscopiques (comme l'essai de compression) en raison de la fragilité du matériau. Au contraire, l'essai de compression hydrostatique sur de petits volumes de matériau entrave considérablement la possibilité de fissuration: des déformations permanentes peuvent être observées sans fissuration lorsque les possibles effets parasites de cisaillement sont absents. Ces essais donnent généralement, après la décharge (*ex situ*), des informations sur les changements de densité.

La combinaison de ces essais avec des techniques de spectroscopie physique (diffraction des rayons X, spectroscopie Raman, Brillouin), par exemple dans une cellule à enclume diamant, permet de suivre *in situ* les changements dans la structure de la silice (ordre à court et à moyenne distance).

Cependant, d'un point de vue de la modélisation mécanique, la réponse mécanique *in situ* de l'essai est partielle car seules les informations de pression sont connues, pas la densité, pendant l'essai.

Les progrès récents en expérimentation ont permis d'obtenir la réponse mécanique *in situ* de l'essai de compression hydrostatique (courbe pression- changements de volume). Les expériences de Sato et Funamori (Phys. Rev. Lett. 2008) ont été menées jusqu'à 60 GPa avec une cellule à enclume diamant à température ambiante. La densité de l'échantillon de verre de silice a été déterminée *in situ* à partir des intensités de rayons X transmis mesurés pour l'échantillon et pour certains matériaux de référence. Ils ont relié leur expérience à l'évolution de la structure de la silice par des méthodes d'absorption des rayons X et des techniques de diffraction. Ils ont constaté que le verre de silice se comporte comme un seul polymorphe amorphe ayant une structure de coordinence quatre (pour l'atome de silicium) en dessous de 10 GPa.

Des changements irréversibles dans l'ordre à moyenne distance commencent à environ 10 GPa (dénommé densification), jusqu'à 25 GPa. Cela correspond à une transformation irréversible et progressive à partir d'une phase amorphe de faible densité à une phase amorphe à haute densité. Cette dernière phase est caractérisée par une augmentation de la distribution

statistique des anneaux à 4 et 3 tétraèdres de  $\text{SiO}_4$  avec une diminution de l'angle inter-tétraédrique.

D'un point de vue plus mécanique, les mécanismes de déformation, entre 0 et 25 GPa, peuvent être représentés comme suit.

- En dessous d'un seuil de pression, le comportement est purement élastique.
- Au-dessus d'un second seuil de pression, ci-après dénommé pression de saturation, le comportement est à nouveau purement élastique.
- Entre ces deux pressions, la densification se développe en augmentant la pression appliquée (durcissement). Il y a également une augmentation significative des modules d'élasticité avec le niveau de densification.

Avant cette récente avancée en expérimentation, la modélisation de la déformation permanente dans des verres était basée sur des essais mécaniques contraints qui font qu'il est possible de développer des champs de déformation permanente stables sans rompre ou même se fissurer. Il s'agit, par exemple, le cas des essais de dureté ou de rayage.

Pour des températures bien en deçà de la transition vitreuse, selon la littérature, la formation de l'empreinte résiduelle résulte de l'apport concomitant de deux mécanismes de déformation: densification et glissement plastique.

Des modèles de comportement ont été développés afin de clarifier cette question sur la dureté du verre. Ils peuvent impliquer la plasticité isochore (ci-après dénommé plasticité) - étant donc incapables de prédire la densification ! -, la densification et la plasticité et même le durcissement.

Ces modèles sont souvent basés sur la description correcte de l'indentation instrumentée, qui enrichit l'essai de dureté en donnant accès à la courbe de charge en fonction de la pénétration. Ces nouvelles données sont utilisées pour suggérer des lois de comportement plus réalistes d'une manière simple.

Le test d'indentation est hétérogène par nature et par conséquent, les simulations numériques par la méthode des éléments finis sont généralement utilisées pour estimer les propriétés des matériaux *via* la courbe de charge en fonction de la pénétration et de l'empreinte résiduelle.

Ces paramètres matériels sont ensuite estimés en utilisant une procédure d'identification. Ces modélisations ont été proposées ces quinze dernières années, notamment dans les œuvres clés de Lambropoulos (J. Am. Ceram. Soc., 1997) et Kermouche *et al.* (Acta Mater., 2008). Ces deux modèles supposent que la combinaison de la pression et du cisaillement provoquent une déformation permanente (densification et la plasticité).

Au final, dans toutes les modélisations, l'attention a été portée principalement sur le rôle du cisaillement sur le processus de déformation permanente. Il semble que différents modèles

permettent de décrire quantitativement la courbe charge-déplacement en indentation instrumentée. On remarque également que certains modèles ne considèrent pas le comportement de durcissement comme celui de densification. Par ailleurs, aucun modèle ne tient compte de la saturation de la densification ainsi que les changements dans les paramètres d'élasticité avec la densification.

Surtout, il faut noter que peu d'attention a été portée à la modélisation de ce qui se passe sur l'axe hydrostatique, c'est-à-dire de ne considérer que la seule pression.

Le but de ce mémoire est donc de se concentrer sur le processus de densification seul sous de très hautes pressions hydrostatiques, avec un nouveau modèle de comportement permettant de tenir compte de l'apparition de la densification au delà d'un seuil de pression, de l'augmentation de la pression appliquée, de sa saturation au delà d'un second seuil de pression, et des changements dans les paramètres d'élasticité couplés avec le processus de densification. Nous limitons les pressions appliquées à des niveaux inférieurs à 25 GPa pour éviter les transformations de phase non liées à la seule densification. Le choix est fait de se placer dans le cadre de la mécanique des milieux continus plutôt que d'utiliser des modélisations mésoscopiques discrètes, comme la dynamique moléculaire, afin de permettre, dans un avenir proche, la simulation d'essais plus compliqués, tels que l'indentation ou rayure, nécessitant un grand nombre d'atomes et de grandes durées de simulation, encore inaccessibles à ce jour avec des modèles mésoscopiques.

Le mémoire est organisé comme suit.

Le premier chapitre, une étude bibliographique, est dédié à la description des verres inorganiques étudiés (verres silicatés, verres au bore, verres de germanates, verres de chalcogénures, verres métalliques) et à leur comportement sous très hautes pressions. L'historique des expériences (conditions d'essai, discussion scientifiques voire polémiques) est tout d'abord rappelé dans des conditions quasi-hydrostatiques mais aussi lors d'essais d'indentation, de rayage ou encore de dynamique (chocs et impacts).

Les conséquences de la densification sont ensuite décrits en termes de propriétés mécaniques (célérités des ondes acoustiques, paramètres d'élasticité) et de changement de comportement physique étudié par des techniques de spectroscopie de diffusion Raman et Brillouin.

Les techniques de modélisation sont ensuite abordées aux échelles atomiques (dynamique moléculaire) et macroscopique (milieux continus et simulations éléments finis). Enfin, les modifications structurales du réseau vitreux à courte et moyenne distance sont décrites en lien avec les différentes étapes de la densification.



Le second chapitre décrit le nouveau modèle de comportement envisagé pour modéliser la densification sous très hautes pressions dans le verre de silice.

Pour cela, nous utilisons les données expérimentales *ex situ* de Rouxelet *al.* (J. Appl. Phys. 2010) pour estimer les paramètres matériels figurant dans nos équations de comportement. Plusieurs types d'écrouissage sont envisagés (linéaire, non-linéaire). Les différents mécanismes sont clairement décrits étape par étape.

Nous avons implémenté notre modèle de comportement dans le code de calcul par éléments finis Abaqus/Standard *via* une routine UMAT. Nous décrivons l'ensemble des équations en petites transformations du fait de l'utilisation d'une configuration corotationnelle pour les écrire, avant de passer à la configuration déformée.

Nous présentons ensuite une simulation par éléments finis de l'essai de compression hydrostatique. Enfin, après avoir décrit la méthode inverse retenue, nous identifions nos paramètres matériels inconnus à partir des données expérimentales *in situ* de Sato et Funamori (Phys. Rev. Lett., 2008).

La comparaison entre simulations numériques et résultats expérimentaux est très bonne, ce qui nous permet de valider notre modèle, en particulier avec un écrouissage non linéaire.

Une perspective immédiate à ce travail est de s'intéresser maintenant aux couplages entre pression et cisaillement, densification et plasticité, et ce pour décrire les essais plus complexes d'indentation et de rayage. Une autre perspective est d'utiliser le modèle proposé pour le verre de silice pour d'autres verres silicatés afin d'étudier l'effet de modificateurs de réseau sur les mécanismes de densification et de glissement plastique.

# Introduction

It is well known that the density of glasses, such as silica, silicate glasses, boric oxide glass, germanate glasses, chalcogenide and chalcogen halide glasses, and bulk metallic glasses can be increased under high pressures [Bridgman 1953, Rouxel 2008]. In particular, amorphous silica ( $\text{SiO}_2$ ) densifies permanently under hydrostatic pressure [Bridgman 1953, Meade 1987, Zha 1994, Sato 2008], indentation [Peter 1970, Yoshida 2005], shock loading [Sugiura 1997] or neutron irradiation [Katayama 2005]. As a matter of fact, the density of amorphous silica can be increased by up to 20% and that of window glass by 6%, when a sufficiently high hydrostatic pressure is applied [Ji 2006, Rouxel 2008, Sato 2008].

Previous studies showed that densification plays a major role in amorphous silica whereas volume conservative shear flow predominates in bulk metallic glasses [Yoshida 2005]. Permanent modification in silica glass density is uneasy to investigate via unconstrained macroscopical testing (such as the compression test) because of the material brittleness. As far as we know, high pressure investigations have mostly focused on the subtle structural changes occurring at the atomic scale and were limited to very few glass systems among which silica is by far the most documented one [Rouxel 2008]. Moreover, data on the post-decompression density change are especially scarce, either because specimens fragmented during the test—which means that the loading was not perfectly hydrostatic—or because the specimens were too small. Therefore, to clarify the deformation behavior of glass under high pressure and from a modeling point to study this case are of paramount interest to get insight into the mechanism of inelastic deformation observed in glasses at room temperature.

Tracing back to the pioneering work of Bridgman and Simon [Bridgman 1953], silica presented a permanent densification behavior by measuring the densities before and after compression, and reached 6-7 percentage increase in density subjected to a pressure of 200 kilobars at room temperature. Following this work, Cohen and Roy [Roy 1961, Cohen 1961] reported a density increase of 7 percent at only 55 kilobars, and pointed out that from 20 to 160 kilobars, densification of silica glass at room temperature was a linear function of pressure by using the refractive index as a probe for densification. Afterwards, Wier and Spinner [Wier 1962], commented on Cohen and Roy's results and pointed out that there was no simple direct correspondence between refractive index and density. Replying to Wier's question, Cohen and Roy

pointed out the fact that shear played an important role in the kinetics of densification [Cohen 1962]. Mackenzie [Mackenzie 1963a, Mackenzie 1963b], used Diamond anvil cell loading apparatus with different confining media (alumina or silver chloride) to study the role of shear, time and temperature. Interestingly, they found ~16 percent densification, which was much bigger than that obtained by Bridgman and Cohen, for silica under 80 kilobars pressure at 300°C by using alumina cell. And he concluded that densification resulting from compression of silica glass in the rigid state depends on the external shear inherent to the particular apparatus and technique. Meanwhile, Christiansen et al. [Christiansen 1962], found a force distribution induced heterogeneous of densification from the samples' center to its boundaries. Furthermore, Arndt [Arndt 1969], studied the effect of impurities on densification of silica glass and demonstrated that densification of vitreous silica under identical experimental conditions produces different results, depending on the nature and relative concentrations of different kinds of impurities.

In the 1980's, Mao-Bell type diamond cells were used in combination with Brillouin- and Raman-scattering physical spectroscopies to measure the static compression of fused silica [Grimsditch 1984]. Grimsditch used Brillouin scattering to show that an irreversible change in the longitudinal sound velocity took place between 10-17 GPa and indicated the existence of a new form of amorphous SiO<sub>2</sub>, which is stable at atmospheric pressure. Grimsditch felt that it deserved the label “amorphous polymorph”. Afterward, Meade and Jeanloz [Meade 1987] measured the static compression of fused silica above 10 GPa, and they found that the bulk modulus increased sharply at high hydrostatic pressure (~11 GPa). They inferred that at high pressure the compression mechanisms were similar at equivalent volumes and thus the increase in bulk modulus was due to the transition between relaxed and unrelaxed moduli. Furthermore, Meade et al. used x-ray diffraction to measure the first sharp diffraction peak of SiO<sub>2</sub> glass, and found that the coordination of Si. Initially 4 increases between 8 to 28 GPa and reaching six at 42 GPa [Meade 1992]. Later, Zha et al. measured the acoustic velocities and refractive index of SiO<sub>2</sub> glass up to 57.5 GPa by Brillouin scattering in diamond cells at room temperature. They found that both longitudinal and transverse velocities increased sharply between 12 and 23 GPa, and the bulk velocity followed a trend similar to coesite at higher pressures [Zha 1994].

More recently, Rouxel et al., used octahedral multi-anvil apparatus (OMAA) to carry out more ideal hydro-static pressure experiments [Ji 2007, Rouxel 2008]. They

obtained whole samples that not break after decompression for pressures as high as 25 GPa and measured the densities [Ji 2007]. More recently, Sato and Funamori, developed synchrotron x-ray absorption and diffraction techniques to measure the in-situ behavior of Silica under high pressure up to 100 GPa [Sato 2008, Sato 2010]. They succeeded in measuring the densities up to 50 GPa. Wakabayashi et al., studied the compression behavior of fully densified SiO<sub>2</sub> glass up to 9 GPa at room temperature and clarified that the glass behaved in an elastic manner by optical-microscope observation, x-ray diffraction and Raman scattering measurements [Wakabayashi 2011].

From a more mechanistic point of view, the deformation mechanisms, between 0 to 25 GPa, may be depicted as follows [Bridgman 1953, Cohen 1962, Zha 1994, Rouxel 2008, Sato 2008, Wakabayashi 2011]. Below a threshold pressure, the behavior is purely elastic. Above a second threshold pressure, further referred to as saturation pressure, the behavior is once again purely elastic. In between these two pressures, densification occurs and develops by increasing the applied pressure and the elastic moduli increase with the densification level.

At the same time, molecular dynamic simulations and finite element analysis have been used to explore the densification mechanisms in amorphous silica. For molecular dynamic simulations, Tse et al. used a two body potential model to study the structure of amorphous SiO<sub>2</sub> at ambient pressure and found that the Si coordination number with oxygens in the network increases from 4 to about 5 in the material taken at 15 GPa and reaches 6 at higher pressures [Tse 1992]. Valle et al. draw the same conclusion [Valle 1996]. For finite element analysis, constitutive models were developed to clarify this issue with respect to the hardness of glass [Yasui 1982, Lambropoulos 1997, Kermouche 2008]. In Yasui and Imaoka's work, they introduced a densification factor into their Mohr-Coulomb type modeling to study different alkali content Na<sub>2</sub>O-SiO<sub>2</sub> glasses [Yasui 1982]. Lambropoulos et al. discussed a constitutive model describing the permanent densification of fused silica under large applied pressures and shear stresses. Their constitutive law is assumed to be rate-independent and uses a yield function coupling hydrostatic pressure and shear stress, a flow rule describing the evolution of permanent strains after initial densification [Lambropoulos 1997]. Recently, Kermouche et al. developed an elliptic yield criterion to establish a new constitutive law to model the plastic deformation of amorphous silica [Kermouche 2008]. A set of material properties was determined by

comparing experimental load-displacement indentation curves to from their finite simulations. Their results show good agreement with the indentation-induced densification maps obtained by Perriot et al. [Perriot 2006].

In all these models, attention has been paid mainly on the role of shear on the permanent deformation process. It appears, from the survey of these constitutive equations and the numerical simulations made with them, that different models allow one to fit the load-displacement curve in instrumented indentation. It is worth pointing out that, some models do not consider hardening-like behavior of densification [Imaoka 1976, Lambropoulos 1997]. Moreover, no model takes into account the saturation in densification as well as the changes in elastic parameters with densification. Meanwhile, not much effort has been devoted to what takes place on the hydrostatic axis during hydrostatic compression.

The purpose of this work is to review the densification behavior of glass under very high pressure and clarify the deformation process under pressure of silica. Furthermore, recent advances in experimental testing have made it possible to obtain the *in situ* mechanical response of hydrostatic compression experiments (curve pressure-volume changes). A new constitutive equation is established to portray the deformation process including densification, hardening, saturation of densification, and changes in elastic moduli below 25 GPa.

This thesis is organized as follows:

- Chapter 1 presents an overview of the physical and mechanical properties of glasses with a specific focus on the fundamental deformation mechanisms of densification and shear flow in glasses. Based on the glass compositions of interest, we give a clear densification research progress from its foundation and controversial topics, and apparatus technical developments and their achievements, microscopic evidence with structure transformation analysis, molecular-dynamics simulations and numerical finite element methods study of its deformation and densification mechanisms. Finally, we summarize the universal densification phenomenon and discuss the intricate but promising interplay between the elasticity, plasticity, densification, hardening and saturation mechanisms during the glasses deformation process.
- Chapter 2 firstly presents the useful experimental information both of *ex situ* and *in situ* experiments, and then extracts the data for our simulations. Then we establish our constitutive equations step by step from simple to complex

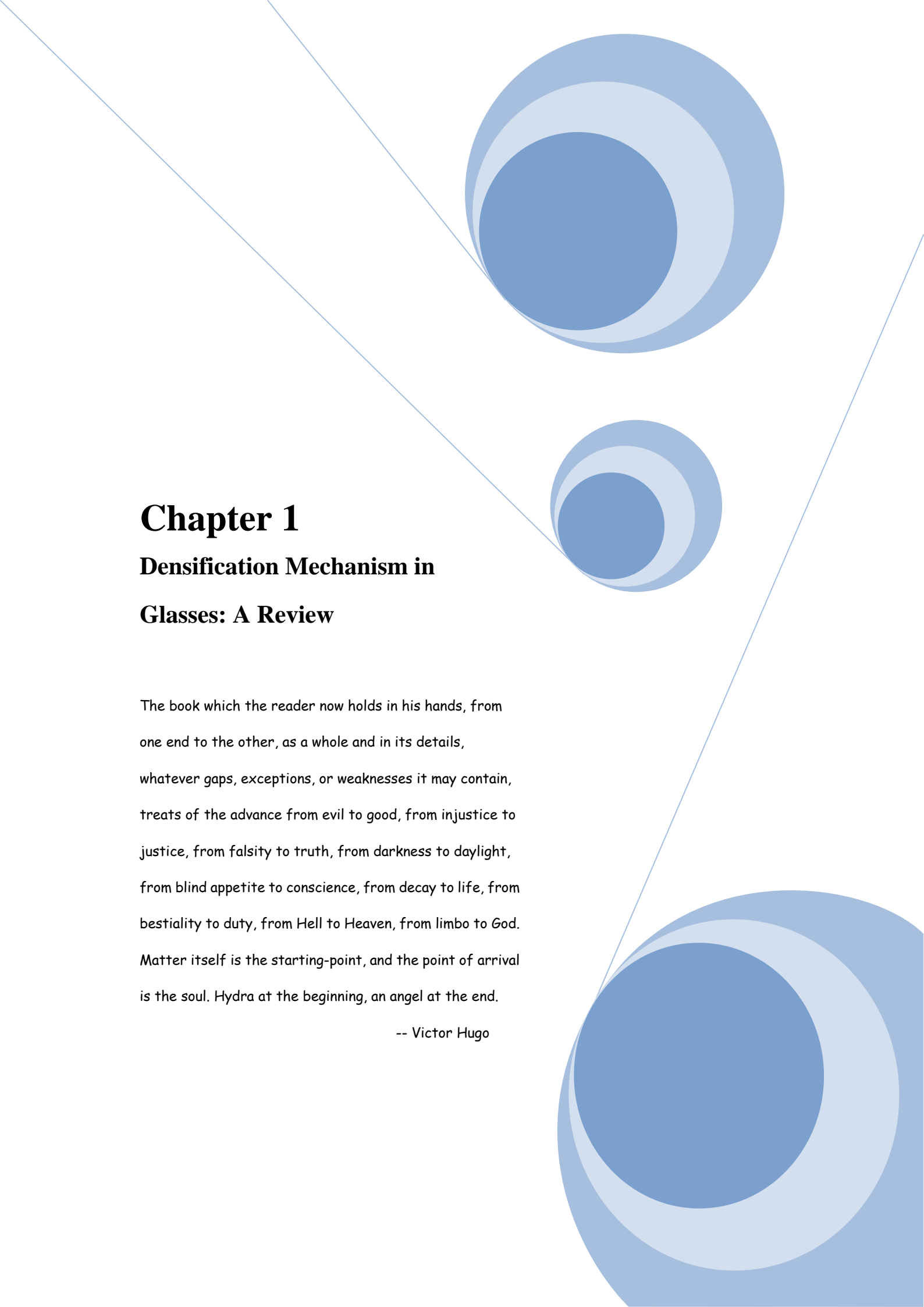
by means of the yield function and flow rule. Then we implement the numerical model via the subroutine UMAT into ABAQUS (FE software). Our numerical results are compared with the *ex situ* experimental data and *in situ* experimental data. Three different hardening rules (one linear hardening and two non-linear hardening laws) are used in our simulations. Reverse analysis is employed to identify some parameters of the models. It is shown that our models have good agreement with both *in situ* and *ex situ* experimental results.

- 1) [Arndt 1969] J. Arndt. *Effect of impurities on densification of silica glass*. J. Am. Ceram. Soc. **52**, 285 (1969).
- 2) [Bridgman 1953] P. W. Bridgman, and I. Simon. *Effects of very high pressures on glass*. J. Appl. Phys., **24**, 405 (1953).
- 3) [Christiansen 1962] E. B. Christiansen, S. S. Kistler, and W. B. Gogarty. *Irreversible compressibility of silica glass as a means of determining the distribution of force in high-pressure cells*. J. Amer. Ceram. Soc., **45**, 172 (1962).
- 4) [Cohen 1961] H. M. Cohen, and R. Roy. *Effects of ultrahigh pressure on glass*. J. Amer. Ceram. Soc., **44**, 523 (1961).
- 5) [Cohen 1962] H. M. Cohen, and R. Roy. *Reply to “comments on ‘Effects of ultrahigh pressure on glass’ ”*. J. Am. Ceram. Soc., **45**, 398 (1962).
- 6) [Grimasditch 1984] M. Grimasditch. *Polymorphism in amorphous SiO<sub>2</sub>* Phys. Rev. Lett., **52**, 2379 (1984).
- 7) [Ji 2007] H. Ji. *Mecanique et physique de l’indentation du verre*. Thesis, Devant l’Universite de Rennes 1, No d’ordre: 3686 (2007).
- 8) [Katayama 2005] Y. Katayama, Y. Inamura. *Structure studies on liquids and glass under high pressure and high temperature*. Nuclear Instruments and Methods in Physics Research B, **238**, 154 (2005).
- 9) [Kermouche 2008] G. Kermouche, E. Barthel, D. Vandembroucq, P. Dubujet. *Mechanical modeling of indentation-induced densification in amorphous silica*. Acta Mater., **56** 3222 (2008).
- 10) [Lambropoulos 1996] J. C. Lambropoulos, S. Xu, and T. Fang. *Constitutive law for the densification of fused silica, with applications in polishing and microgrinding*. J. Am. Ceram. Soc., **79** [6], 1441 (1996).
- 11) [Mackenzie 1963a] J. D. Mackenzie. *High-pressure effects on oxide glasses: I, Densification in rigid state*. J. Amer. Ceram. Soc., **46**, 461 (1963).

- 12) [Mackenzie 1963b] J. D. Mackenzie. *High-pressure effects on oxide glasses: II, Subsequent heat treatment*. J. Amer. Ceram. Soc., **46**, 470 (1963).
- 13) [Meade 1987] C. Meade, and R. Jeanloz. *Frequency-dependent equation of state of fused silica to 10 GPa*. Phys. Rev. B, **35**, 236 (1987).
- 14) [Meade 1992] C. Meade, R. J. Hemley, and H. K. Mao. *High-pressure x-ray diffraction of SiO<sub>2</sub> glass*. Phys. Rev. Lett., **69**, 1387 (1992).
- 15) [Perriot 2006] A. Perriot, D. Vandembroucq, and E. Barthel, V. Martinez, L. Grosvalet, C. Martinet, and B. Champagnon. *Raman microspectroscopic characterization of amorphous silica plastic behavior*. J. Am. Ceram. Soc., **89** [2] 596 (2006).
- 16) [Rouxel 2008] T. Rouxel, H. Ji, T. Hammouda, and A. Moréac. *Poisson's ratio and the densification of glass under high pressure*. Phys. Rev. Lett., **100**, 225501 (2008).
- 17) [Sato 2008] T. Sato, and N. Funamori. *Sixfold-coordinated amorphous polymorph of SiO<sub>2</sub> under high pressure*. Phys. Rev. Lett., **101**, 25502 (2008).
- 18) [Sato 2010] T. Sato, and N. Funamori. *High-pressure structural transformation of SiO<sub>2</sub> glass up to 100 GPa*. Phys. Rev. B, **82**, 184102 (2010).
- 19) [Sato 2011] T. Sato, N. Funamori, and T. Yagi. *Helium penetrates into silica glass and reduces its compressibility*. Nature Commun., **2**, 345 (2011).
- 20) [Sugiura 1997] H. Sugiura, R. Ikeda, K. Kondo, and T. Yamadaya. *Densified silica glass after shock compression*. J. Appl. Phys., **81** (4), 1651 (1997).
- 21) [Tse 1992] J. S. Tse, D. D. Klug, and Y. L. Page. *High-pressure densification of amorphous silica*. Phys. Rev. B, **46**, 5933 (1992).
- 22) [Valle] R. G. D. Valle, and E. Venuti. *High-pressure densification of silica glass: A molecular-dynamics simulation*. Phys. Rev. B, **54**, 3809 (1996).
- 23) [Wakabayashi] D. Wakabayashi, N. Funamori, T. Sato, and T. Taniguchi. *Compression behavior of densified SiO<sub>2</sub> glass*. Phys. Rev. B, **84**, 144103 (2011).
- 24) [Weir 1962] C. E. Weir, and S. Spinner. *Comments on "Effects of ultrahigh pressure on glass"*. J. Am. Ceram. Soc., **45**, 196 (1962).
- 25) [Yasui 1982] I. Yasui, and M. Imaoka. *Finite element analysis of indentation on glass (II)*. J. Non-Cryst. Solids, **50**, 219 (1982).
- 26) [Yoshida 2005] S. Yoshida, J. C. Sangleboeuf, and T. Rouxel. *Quantitative evaluation of indentation-induced densification in glass*. J. Mater. Res., **20**, 3404 (2005).
- 27) [Zha 1994] C. S. Zha, R. J. hemley, H. K. Mao, T. S. Duffy, and C. Meade.

*Acoustic velocities and refractive index of SiO<sub>2</sub> glass to 57.5 GPa by Brillouin scattering.* Phys. Rev. B **50**, 13105 (1994).





# Chapter 1

## Densification Mechanism in Glasses: A Review

The book which the reader now holds in his hands, from one end to the other, as a whole and in its details, whatever gaps, exceptions, or weaknesses it may contain, treats of the advance from evil to good, from injustice to justice, from falsity to truth, from darkness to daylight, from blind appetite to conscience, from decay to life, from bestiality to duty, from Hell to Heaven, from limbo to God. Matter itself is the starting-point, and the point of arrival is the soul. Hydra at the beginning, an angel at the end.

-- Victor Hugo

The glass world which the scientists now study in our life, from one dimension to three dimensions, as a whole and in its details, whatever compositions, structures, advantages or weaknesses it may contain, treats of the advance from superficial to profound, from deformation to mechanisms, from falsity to truth, from assumptions to theories, from blind to clarity. Mechanism itself is the predominant-point, and the point of arrival is the soul. Review at the beginning, rule at the end.

## Contents

<b>1.1 Introduction.....</b>	<b>4</b>
<b>1.2 Glass composition and structures.....</b>	<b>5</b>
1.2.1 Silica Glass.....	5
1.2.2 Silicate glasses.....	7
1.2.3 Boric oxide glass.....	7
1.2.4 Germanate glasses.....	8
1.2.5 Chalcogenide and chalcohalide glasses.....	8
1.2.6 Bulk metallic glasses.....	8
<b>1.3 Densification experiments.....</b>	<b>10</b>
1.3.1 Densification under high-pressure.....	11
1.3.1.1 Definition of densification.....	11
1.3.1.2 Archimedes methods for measuring density.....	11
1.3.1.3 Techniques of high-pressure.....	12
1.3.1.4 Densification behavior under high-pressure.....	16
1.3.2 Indentation and Densification.....	24
1.3.2.1 Indentation and Cracks.....	24
1.3.2.2 Quantitative evaluation of indentation-induced densification.....	25
1.3.3 Shock Wave Compression and Structure.....	26
1.3.3.1 Densification and shock compression.....	26
1.3.3.2 First sharp diffraction peak study.....	27
<b>1.4 Densification and materials' properties.....</b>	<b>29</b>
1.4.1 Sound velocities and refractive index.....	29
1.4.2 Bulk modulus, elastic modulus and shear modulus.....	30
1.4.3 Poisson's ratio and the high pressure densification.....	33
1.4.4 Densification and Raman spectroscopy.....	35
<b>1.5 Modeling of densification.....</b>	<b>37</b>
1.5.1 Molecular-dynamic simulation.....	37
1.5.2 Finite element method (FEM).....	37
<b>1.6 Discussion and prospect.....</b>	<b>42</b>
1.6.1 Effect of time and temperature .....	42

---

1.6.2 Intermediate-range order interpretation.....	42
<b>1.7 Summary.....</b>	<b>44</b>
<b>References.....</b>	<b>46</b>

## 1.1 Introduction

Plasticity in metals, ceramics, polymers and metallic glasses is of paramount importance both in engineering and science research from a fundamental point of view. The inelastic deformation at the macroscopic and microscopic scales of glasses present a great interest to physicists, material scientists and engineers [Taylor 1949, Marsh 1964, Primak 1975, Varshneya 1994, Zarzycki 1991]. Shear flow, densification, and hardening, the most important aspects standing for the inelastic properties of glasses, are issues, yet to be understood.

In particular, pressure induced changes in the structure and properties of glasses, such as fused silica, silicate glasses, boric oxide glass, germinate glasses, chalcogenide and chalcohalide glasses, and bulk metallic glasses, is an important and challenging issue in contact mechanics and condensed-matter physics [Bridgman 1953, Rouxel 2007]. Numerous experimental and theoretical studies have revealed that  $\text{SiO}_2$  glass shows anomalous behavior such as elastic softening with increasing pressure up to 2-5 GPa [Grimsditch 1984, Zha 1994] and permanent densification by applying a pressure more than 10 GPa [Bridgman 1953, Grimsditch 1984, Meade 1987, Zha 1994, Rouxel 2008, Sato 2008]. Moreover, indentation [Peter 1970, Yoshida 2005], shock wave compression [Sugiura 1997], or neutron irradiation [Katayama 2005] experiments all show the densification behavior in silica. At the same time, molecular dynamic simulations [Valle 1996, Liang 2007] and finite element analysis [Xin 2000, Kermouche 2008] are used to explore the densification mechanism in amorphous silica, which might help us for further understanding. For the sake of understanding the deformation behavior, it is important to holistically summarize the accumulated data over the past decade or so.

In this chapter, our purpose is to present an overview of the physical and mechanical properties of glasses especially with a specific focus on the fundamental deformation mechanism of densification and shear flow in glasses. Based on the interesting glass composition and structures, we give a clear densification research progress from its foundation and controversial topics, and apparatus technical developments and their achievements, microscopic evidence with structure transformation analysis, molecular-dynamics simulations and numerical finite element methods study of its deformation and densification mechanism. Finally, we summarize the universal densification phenomenon and discuss the intricate but promising hotspot which involves the elasticity, plasticity, densification, hardening and saturation during the glasses deformation process.

## 1.2 Glass composition and structures

Inorganic glasses are spectacular materials to study from a fundamental point of view as they pose challenging and as yet unsolved problems in the field of condensed matter physics and solid mechanics [Greaves 2007]. Silicate glasses, borosilicate glasses, germanate glasses, chalcogenide and chalcogen halide glasses, polymer glasses, and bulk metallic glasses have been investigated from a densification point of view. From a historical standpoint silicate glasses are the most ancient materials known to mankind, have been found predominantly amongst all the used inorganic glasses, and indeed offer important insight into the physical-mechanical-chemical research in the last 60 years. Normally, the composition, the static atomic structure and some basic material properties of inorganic glasses draw attention to researchers. Following, we select some typical glasses to recommend helping us having a good understanding of them.

### 1.2.1 Silica glass

Among all the previous research, pure silica glass (vitreous silica, fused silica) is the most used glass for its main property of transparency in the visible light, and also since it has a great refractoriness, a high chemical resistance to corrosion (particularly to acids), a very low electrical conductivity, a near-zero ( $\sim 5.5 \times 10^{-7} / ^\circ\text{C}$ ) coefficient of thermal expansion, and good UV transparency. In most cases, (there are around 20 ways for obtaining amorphous silica!) silica glass is obtained by melting high-purity quartz crystals or beneficiated sand at temperatures in excess of  $2000^\circ\text{C}$  [Varshneya 1994].

The structure of silica glass is the simplest of all the glass structures, yet many of the details are not yet fully understood [Wright 1989]. As shown in figure 1.1a, glass consists of slightly distorted  $\text{SiO}_4$  tetrahedral joined to each other at corners. The basic unit is shown in figure 1.1b. Each oxygen acting as a bridge between neighboring tetrahedra, and hence is called bridging oxygen, or simply a BO. Nearly 100% of the oxygens are bridging except for some defect sites and for those associated with impurities in commercial specimens. The bond details, especially the bond strength of

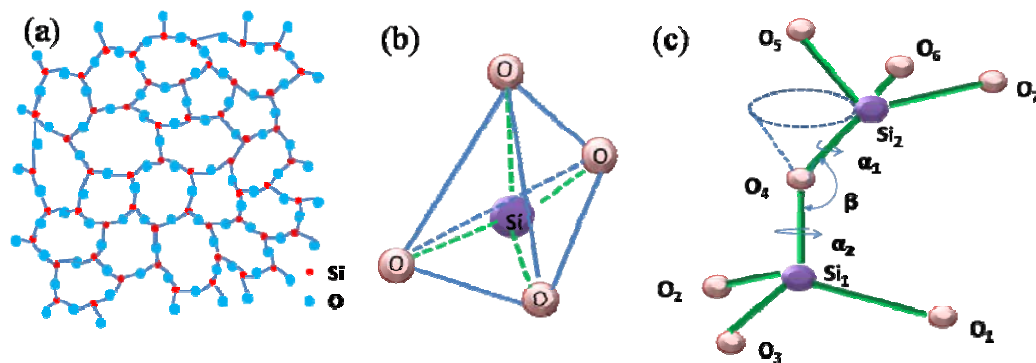


Figure 1.1 (a) Atomic structures representation of  $\text{SiO}_2$  glass. (b) Basic unit of  $\text{SiO}_2$ .

(c) Definition of the bond angle  $\beta$  and the torsion angles  $\alpha_1$  and  $\alpha_2$ .

$\text{Si-O}$ , are presented in Table 1.1. The angle  $\beta$  between two neighboring tetrahedra

( $\text{=Si}_{(1)}\text{-O}_4\text{-Si}_{(2)}\text{=}$  angle) is called the bond angle. Torsion angles  $\alpha_1$  and  $\alpha_2$  are, respectively, the azimuth angle between  $\text{Si}_{(1)}\text{-O}_1$  and  $\text{O}_4\text{-Si}_{(2)}$  when projected on the  $\text{O}_1\text{-O}_2\text{-O}_3$  plane, and the rotation angle about the  $\text{O}_4\text{-Si}_{(2)}$  axis. Mostly, the disorder of the glass structure is ascribed to the variations in the bond angle  $\beta$  and the torsion angles  $\alpha_1$  and  $\alpha_2$ , and to some extent to the variation in bond lengths [Varshneya 1994].

Table 1.1 Single Bond Strength for Oxides [Varshneya 1994]

M in MOx	Valence	Dissociation energy $E_d$ per MOx (kcal)	Coordination number	Single-bond strength (kcal)
B	3	356	3	119
Si	4	424	4	106
Ge	4	431	4	108
Al	3	402-317	4	101-79
B	3	356	4	89
P	5	442	4	111-88
V	5	449	4	112-90
As	5	349	4	87-70
Sb	5	339	4	85-68
Zr	4	485	6	81

For vitreous silica or fused silica, their composition is 100% of  $\text{SiO}_2$ , and the density at room temperature, Poisson's ratio, Young's modulus (E), bulk modulus (K), shear modulus (G), glass transition temperature, and refractive index are listed in table 1.2. Even if, there are small changes in their properties by different processing methods or properties measurements, the basic properties are always convincing.

Table 1.2 Composition and basic properties of inorganic glasses

Chemical systems	Composition (mol.%)	Density $\rho$ (g/cm <sup>3</sup> )	Poisson's ratio $\nu$	Young's modulus E (GPa)	Bulk modulus K (GPa)	Shear modulus G (GPa)	Glass transition temperature $T_g$ (K)	Refractive index n	References
Vitreous silica	$\text{SiO}_2$	2.20	0.15	70	33.3		~1463	1.458	[Rouxel 2007]
	$\text{SiO}_2$	2.20	0.17	74.5		31.9	1373	1.458	[Ji 2007]
Window Glass	72.6 $\text{SiO}_2$	2.514	0.23	71.5		29.1	773		[Ji 2007]
Vitreous borates	$\text{B}_2\text{O}_3$	2.55	0.26	17.1	12.1		541		[Rouxel 2008a]
Germanates	$\text{GeO}_2$	3.63	0.19	43.3	23.28		808	1.608	[Rouxel 2007]
Chalcogenides	$\text{GeSe}_2$	4.2			15	14	658	1.7	[Antao 2008]
	80Se-20Ge ( $\text{GeSe}_4$ )	4.337	0.29	14.8		5.7	435		[Ji 2007]
BMGs	55Zr-30Cu-10Al-5Ni	6.830	0.38	81.4			683		[Ji 2007]

### 1.2.2 Silicate glasses

Silicate glasses usually contain up to 60-70 mol%  $\text{SiO}_2$ . Usual additives include alkaline and alkaline-earth oxides among which  $\text{Na}_2\text{O}$  and  $\text{CaO}$  are the most common in window glass compositions. The alkaline and alkaline-earth oxides are network modifiers; they enter the glass as singly charged cations and occupy interstitial sites. Such elements (P, Al, Ge, Zr, Si, and B) give their names to different oxide glass families with  $T_g$  ranging between 600 and 1300 K and Young's modulus between 30 and 100 GPa [Rouxel 2007].

Some silica-soda glass (10mol.% $\text{Na}_2\text{O}$ , 23mol.% $\text{Na}_2\text{O}$  or 31mol.% $\text{Na}_2\text{O}$ ) [Bridgman 1953], silica-alkali glass (22mol.% $\text{Li}_2\text{O}$ , and 23mol.% $\text{K}_2\text{O}$ ) [Bridgman 1953], Ca-Mg-Na glass (79.6%  $\text{SiO}_2$ ) [Meade 1987] and Some soda-lime glass (window glass, 72.6 $\text{SiO}_2$  -9.8  $\text{Na}_2\text{O}$  -6.0  $\text{CaO}$  -4.3  $\text{K}_2\text{O}$  -2.9  $\text{MgO}$  -2.4  $\text{BaO}$  -2.0  $\text{Al}_2\text{O}_3$ ) [Ji 2006, Rouxel 2008a] are used to investigate their deformation under high-pressure and their densification behavior. Properties of one typical silicate glass, windows glass (WG) used by Ji et al. [Ji 2007], with a density of 2.514 g/cm<sup>3</sup> has a higher Poisson's of 0.23 compared to vitreous silica are listed in Table 1.2.

### 1.2.3 Boric oxide glass

Compared to silicate glasses, in borate glasses the polymerization of the network former,  $\text{B}_2\text{O}_3$ , is different from silica and the modification of the borate glass network does not follow the same rules as silicate glasses. The structure of the simplest borate glass is  $\text{B}_2\text{O}_3$ , where the oxygen coordination around each B is only 3, and hence the basic structure unit is  $\text{BO}_3$  triangle. It is believed that B is slightly above the plane of the three oxygens. Again, all the oxygens are bridging between neighboring triangles. It seems that the glass structure consists, to a large extent, of planar  $\text{B}_3\text{O}_6$ , boroxol rings made of three corner-shared  $\text{BO}_3$  triangles, as shown in figure 1.2 [Greaves

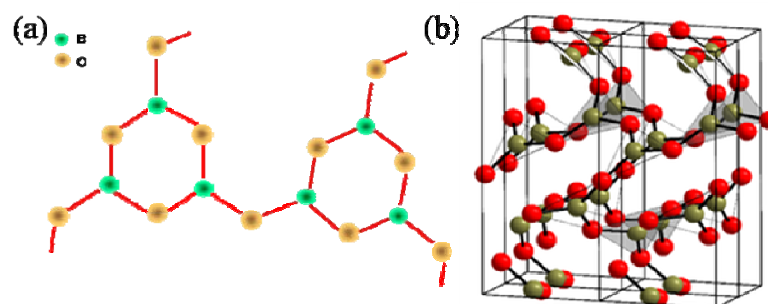


Figure 1.2 (a) Configuration of the boroxol ring. (b) Three-dimensional representation of the random network model of the structure of  $\text{B}_2\text{O}_3$  glass consisting of  $\text{B}_3\text{O}_6$  boroxol groups and  $\text{BO}_3$  triangles. B and O atoms are shown as red and turquoise, respectively. [Varshneya 1994]

2007, Bray 1998, Jellison 1977, Walrafen 1980, Hannon 1995, Youngman 1994]. These rings are connected one to another by a small non-ring population of  $\text{BO}_3$  triangles. Studies demonstrate that ~75% of B atoms need to be in boroxol rings in

order for the structure to be consistent with intermediate-range order (IRO) [Mackenzie 1963a, Miracle 2004] features and indeed the density of  $B_2O_3$  glass [Takada 2003]. Compared to silicate glass,  $B_2O_3$  has a much lower Young's modulus and bulk modulus about 17 GPa and 12 GPa (see in Table 1.2), respectively.

#### 1.2.4 Germanate glasses

$GeO_2$ -based glasses are transparent in the 2-6  $\mu m$  IR wavelength range and exhibit a good chemical durability. According to Hwa and Chao [Hwa 2005], the thermal properties of germanates are comparable with those of silicates, which have smaller cations and anions and thus have a lower IR cutoff. Hence, germanate glasses could be used in high-energy laser applications for their excellent transmission in visible and mid-IR regions. A typical glass of germanate glass is  $GeO_2$ , which has a tetrahedral structure of  $GeO_4$  similar to silica glass.

#### 1.2.5 Chalcogenide and chalcohalide glasses

Chalcogenide and chalcohalide glasses are obtained by melting chalcogen elements (group VI: S, Se, and Te) with one or more of groups V and IV elements which poses a good semiconducting behavior, photoconductivity and IR-transmitting properties. These glasses consist of disordered rings (molecules), chains, sheets, and three-dimensional networks. The bonding is generally covalent, with weak van der Waals attraction between the molecules, chains, etc.

Chalcogenide glasses are either sulfides, selenides or tellurides, mainly of B, As, Sb, P, Si and Ge which play the analogous role of network-formers in oxide glasses. Their inherent structural flexibility is related to two important and rather unique characteristics of chalcogenide glasses: (i) besides a covalent network made of corner- and edge-shared coordination polyhedral, the structure may also contain well-defined molecular units and (ii) glasses can be made with compositions that deviate significantly from stoichiometry enabling the average coordination number and energy gap to be altered in a controlled way. The typical used chalcogenide glasses in densification research are  $GeSe_2$  and  $GeSe_4$ . Their properties are given in table 1.2.

#### 1.2.6 Metallic glasses

Metallic glasses, with superior strength and hardness, and excellent corrosion and wear resistance, have arisen great interesting to many scientists in the past two decades. Compared to traditional crystalline metals' long-range order (figure 1.3a), metallic glasses do not have the long-range order and no crystalline boundaries, but have a topological arrangement of atoms inside which present an intermediate-range order is present, as shown in figure 1.3b.



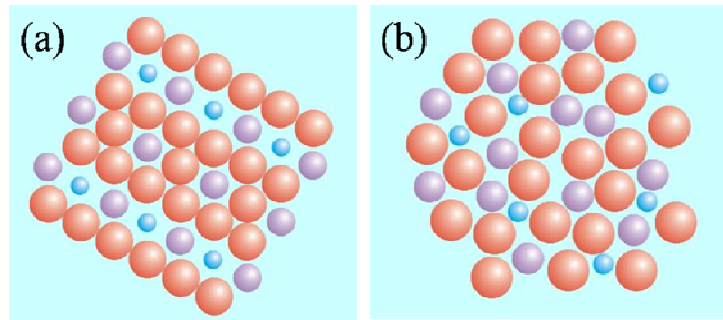


Figure 1.3 Presentation of structure: (a) Normal crystal metals and (b) Bulk metallic glass.

Recently, scientists have found some pressure-densification behavior of  $\text{Zr}_{55}\text{Cu}_{30}\text{Al}_{10}\text{Ni}_5$  and  $\text{Ce}_{75}\text{Al}_{25}$  [Rouxel 2008, Zeng 2010]. The low maximum densification percent may be attributed to its high atomic packing density.

### 1.3 Densification experiments

From the 1950s to the 2010s, works on densification have made great progress.

Table 1.3 Densification research progress from 1950s-2010s.

Period	Experimental Technologies	Research Progress	References
1950s	Carboloy compression apparatus (CCA)	Densification phenomena at high pressure	[Bridgman 1953]
1960s	Opposed-anvil type apparatus(OAA)	Saturation of densification	[Cohen 1961], [Mackenzie 1963a] [Mackenzie 1963b]
	“Belt apparatus” (BA)	Role of time, temperature, pressure and with applied shear	
	High temperature compression	Local densification under indentation	
	Vickers indentation	Hardness measurement	
1970s	Indentation	Densification hand cracks in indentation Densification linked to the decrease of inter bond polarizability	[Peter 1970], [Hagan 1979]
1980s	Diamond anvil cell (Mao-Bell type diamond) Brillouin- and Raman-scattering	Irreversible changes in longitudinal sound velocity under high pressure Bulk modulus increases sharply at hydrostatic pressures in silica glasses Metastable states of amorphous silica	[Grimsditch 1984]
1990s	Neutron-diffraction Shock compression	First shape diffraction peak (FSDP) shows the modification in the intermediate-range order Anomalous changes in slopes between longitudinal and transverse sound velocities in the low-pressure region (around 3 GPa) Pressure dependence of sound velocities, refractive index, bulk modulus and Poisson's ratio up to 57.5 GPa in silica glass	[Suaman 1991], [Meade 1987], [Zha 1994], [Polian 1993]
2000s	Octahedral multi-anvil apparatus (OMAA) X-ray diffraction and synchrotron radiation AFM Develop synchrotron x-ray and diffraction techniques	Intermediate-range order change due to bond rotation and tetrahedral structure distortion causing densification in GeO <sub>2</sub> glass Quantitative estimation of indentation-induced densification in glass Pressure dependence of the FSDP position Low density amorphous phase to High density amorphous phase transition Network rigidity changes in GeSe <sub>2</sub> glass at high pressure A direct correlation between Poisson's ratio and the maximum post-decomposition density among 3D-OD glasses Measuring the density and structure of SiO <sub>2</sub> glass under high pressure up to 207GPa An elastic deformation manner for fully densified silica under 9 GPa	[Ji 2007], [Rouxel 2008a], [Kermouche 2008], [Xin 2000], [Sato 2010], [Wakabayashi 2011]

The developments in densification research are shown in Table 1.3. We would like to present a detailed progress in experiments as follows: (i) densification under high-pressure with experimental achievements and the basic densification behavior; (ii) densification and indentation, which give us a way to survey the densification phenomena in inorganic deformation process, as well as to understanding the elastic, plastic and hardening behaviors; (iii) densification under shock wave compression, which focus on the instant impact and the hysteresis effect of densification; (iv) synchrotron x-ray absorption and diffraction techniques which provide a way to measure the density and structure of SiO<sub>2</sub> in in-situ experiments.

### 1.3.1 Densification under high-pressure

#### 1.3.1.1 Definition of densification

Historically, the first and most predominant work on densification at the first period (1950s) is provided by Bridgman and Simon [Bridgman 1953, Bridgman 1955]. According to their original work, they designed a Carboly inserted compression apparatus which could reach as high as 20 GPa for quasi hydro static pressures. After a series of high pressures experiments, they found that glasses behave in a perfectly elastic manner at low pressures, while at higher pressure permanent densification occurred. For vitreous silica, they found that before 8-10GPa the silica glass exhibit elastic behavior, while after the threshold pressure irreversible density increase happened up to as high as 20 GPa. Although, their experimental technology could not provide a pure hydro static state causing a lot of fragments of vitreous glass under compression, they found an appreciable permanent density increase about 7.5% compared to the original glass and 17.5% percent of maximum densification in some fragments.

Therefore, this density permanent increase phenomena of glass under high pressure is a typical irreversible behavior of inorganic glasses referred to as densification. Usually, scientists use the changing of density compare to its original density as the densification factor, which correlate to the change in volume, as shown in function 1.1.

$$\text{Densification factor } \alpha = \frac{\Delta\rho}{\rho_0} = \frac{\rho - \rho_0}{\rho_0} \quad (1.1)$$

Where  $\rho_0$ ,  $\rho$  are the original density and actual density,  $\Delta\rho$  is the permanent changes in density compression.

#### 1.3.1.2 Archimedes methods for measuring density

The densities of the samples before and after compression were obtained by means of a density gradient method consisting in learning the samples float in a mixture of two liquids as shown in figure 1.4. For instance, Bridgman and Simon used tetrabromoethane,  $\rho=2.95 \text{ g/cm}^3$  and carbon tetrachloride,  $\rho=1.45\text{g/cm}^3$ , and Ji and Rouxel et al., see figure 1.4, using iodobenzene,  $\rho=3.32 \text{ g/cm}^3$  and methylene iodide,  $\rho=1.83 \text{ g/cm}^3$  to determine the densities of samples. Besides, by means of image analysis, using high resolution images of the specimens taken prior to- and after-testing one can reach an accuracy density better than  $0.001 \text{ g/cm}^3$ .

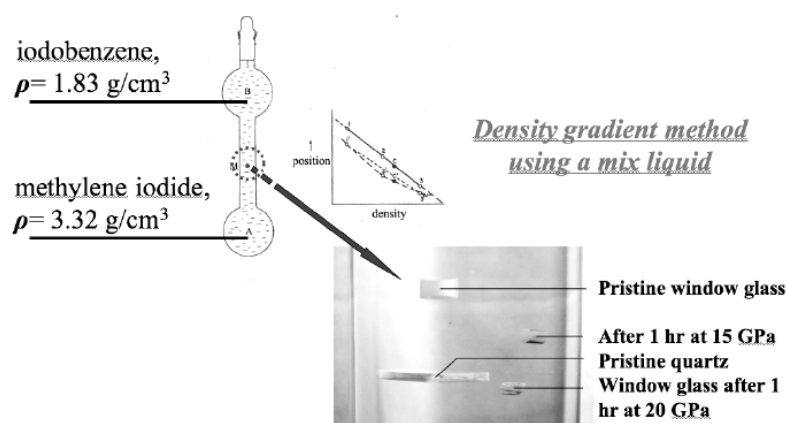


Figure 1.4 Density gradient method slowly miscible liquids with different densities (Ji 2007).

### 1.3.1.3 Very high-pressure techniques

- Very high-pressure techniques in 1950s

When working in the range of pressures above 5 GPa, it becomes difficult to operate strictly under hydrostatic conditions because of the limitations imposed by the mechanical properties of the materials used for the pressure transmitting media. Fortunately, Bridgman and Simon designed a Carboly insert compression apparatus (CCA, as shown in Figure 1.5a), using a 75-ton hydraulic press to apply loads on small and thin disks to explore the very high pressure (as high as 20 GPa) effect on glass. Their initial work discovered the densification behavior of glass by using CCA apparatus, but some shortage of their experiment were easy to be found as follows. (i) Although, the dies were made of Carboly (Young's modulus around 90 GPa), with very low compressibility, they presented a non-uniform distribution of stress over the contact area under the load. (ii) The normal stress at the center of the disk was lower than average (total load divided by the total area of the disk) and the radial tangential (shearing) stresses have their largest values near the periphery. Therefore, no homogeneous deformation happened on their samples but left fragments after stress released.

In summary, in these years, hydro static apparatus turns up. The shortage of the machine is the unbalance distribution of pressure and the great influence of shear.

- Very high-pressure techniques in 1960s

Keeping in mind the difference in the stress fields between the center and outside edge of the anvil surfaces on Bridgman and Simon's investigation, Christiansen et al., designed and constructed a multi-ring apparatus, as shown in figure 1.5b [Ernsberger 1968, Christiansen 1962], to survey the irreversible compressibility of silica glass as a means of determining the distribution of force in high-pressure cells. According to their work, they obtained the approximate force distributions over the cells used in the radioactive decay studies. Two types of cells were used in their investigation compared with Bridgman's work, and they showed that it is misleading to use an

average method to calculate the pressure and density from the fragments, but and that one must consider the pressure distribution from the center to the edge on the compressed samples to study the high pressure effect. Using pipestone disks coated with metallic gold-bronze pressure cell, they succeeded in producing a symmetrical compression of the disks with a low densification (maximum on the edge ~8%), while using silver chloride- modified or lead-modified pressure cell, they found unsymmetrical load phenomena and reached a much higher permanent densification (maximum on the edge ~14.09%). It is worthy to mention that their method provides us a way to determine the influence of shear as well as to study force distribution on the disks by using different types of pressure cells.

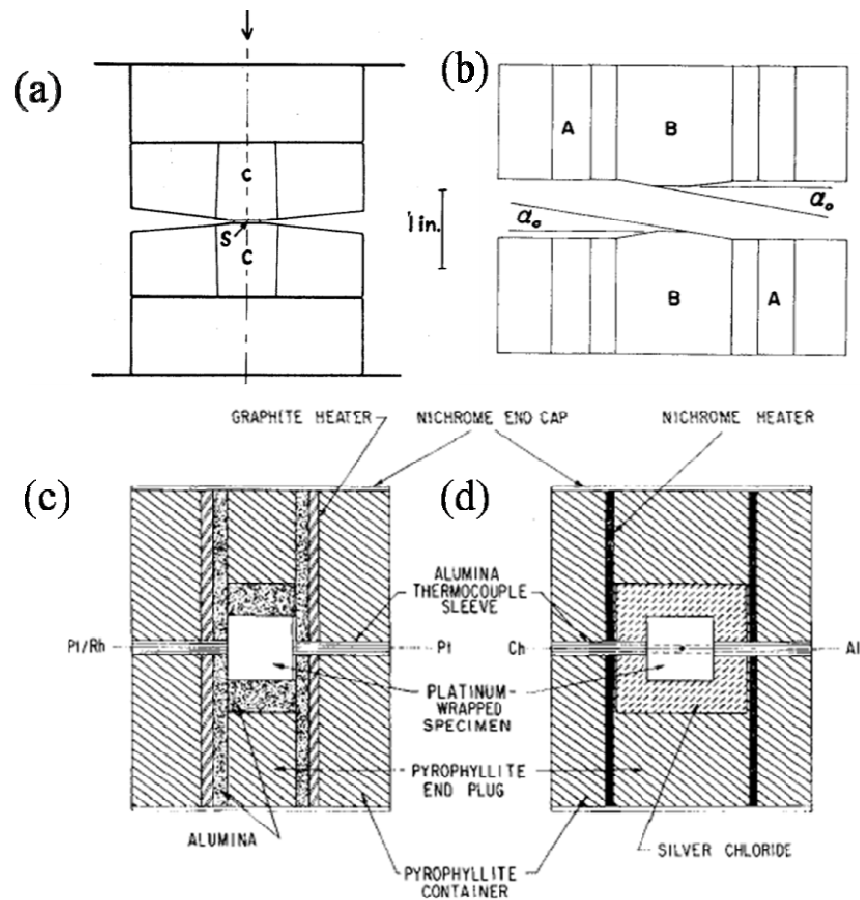


Figure 1.5 (a) Schematic diagram of compression apparatus. S- specimen; C- Carbobloy inserts.[Bridgman 1953] (b) Schematic of anvil assembly. [Ernsberger 1968] (c) High pressure alumina cell "belt" densification apparatus. [Mackenzie 1963a] (d) High pressure silver chloride cell "belt" densification apparatus. [Mackenzie 1963a]

Facing the controversy of densification process between Bridgman, Cohen, Christianse, et al., Mackenzie used a high-pressure "belt" apparatus [Hall 1960] using two types of cells as shown in figure 1.5c and figure 1.5d. The specimen was placed in the center of the pyrophyllite cell and separated from the graphite or Nichrome resistance heater by two different types of materials. As shown in figure 1.5c, the first type was stainless steel or alumina, hard pressure-transmitting medium, which

represented the largest departure from ideal hydrostatic condition. The second class of pressure-transmitting materials used consisted of isopentane, silicone oil and silver chloride, as shown in figure 1.5d, representing a closer approach to hydrostatic behavior or a condition of minimum shear. In general, this apparatus helped Mackenzie to carry out densification experiments on some desired pressures and temperatures to explain the time, temperature, pressure and shear roles during the densification process.

In short, these techniques focus on understanding the pressure distribution impact and trying to decrease the influence of shear. From now, scientist confirmed the elastic deformation process below the densification threshold between 8-10 GPa, and pointed out there will be a maximum densification value as high as to 20 GPa.

- Very high-pressure techniques in 1980s – 1990s

With the technology development, Grimsditch, Meade, Polian, Zha, et al. [Grimsditch 1984, Polian 1986, Meade 1987, Meade 1992, Polian 1993, Zha 1994], used Mao-Bell-type diamond cell apparatus (DAC) to carry out very high pressure experiments. The basic characteristic of the Mao-Bell type DAC is that the ring has a small opening which can be used for Brillouin-scattering spectroscopy. Especially, 135° scattering geometry in the diamond-anvil cell overcome the very high pressure (higher than 40 GPa) experiment's sound velocities transverse problem, used in Zha's investigation work and gave a clear evidence of the acoustic velocities and refractive index effect under high pressure in silica glass.

At the same time, x-ray diffraction methods are used to study the structure changing of silica under very high pressure. Meade et al, measured the x-ray structure factor  $S(Q)$  for SiO<sub>2</sub> glass up to 42 GPa in the diamond-anvil cell. Average pair correlation functions at high pressure reveal significant changes in the nearest neighbor geometry of the glass with compression [Meade 1992].

These techniques help scientists to measure the sound velocities and refractive index of the samples to ultra high pressure up to 57 GPa, and confirm the densification saturation pressure to be around 25-27 GPa. Furthermore these techniques helped us to discover the polymorphism in SiO<sub>2</sub> glass under ultra high pressure. The unsolved problem is how to get the accurate density of the samples for in-situ experiments after pressure higher than 10 GPa.

- Very high-pressure techniques in 2000s

Recently, high pressure experiments were performed in an octahedral multi-anvil apparatus (OMMA) using a Walker module [Ji 2006, Rouxel 2008a, Rouxel 2008b] and following the procedure described elsewhere [Walker 1990, Hammouda 2003], as shown in figure 1.6a. According to this work, most specimens came out in one piece suggesting that the pressure device induced very little shear up to 25 GPa.

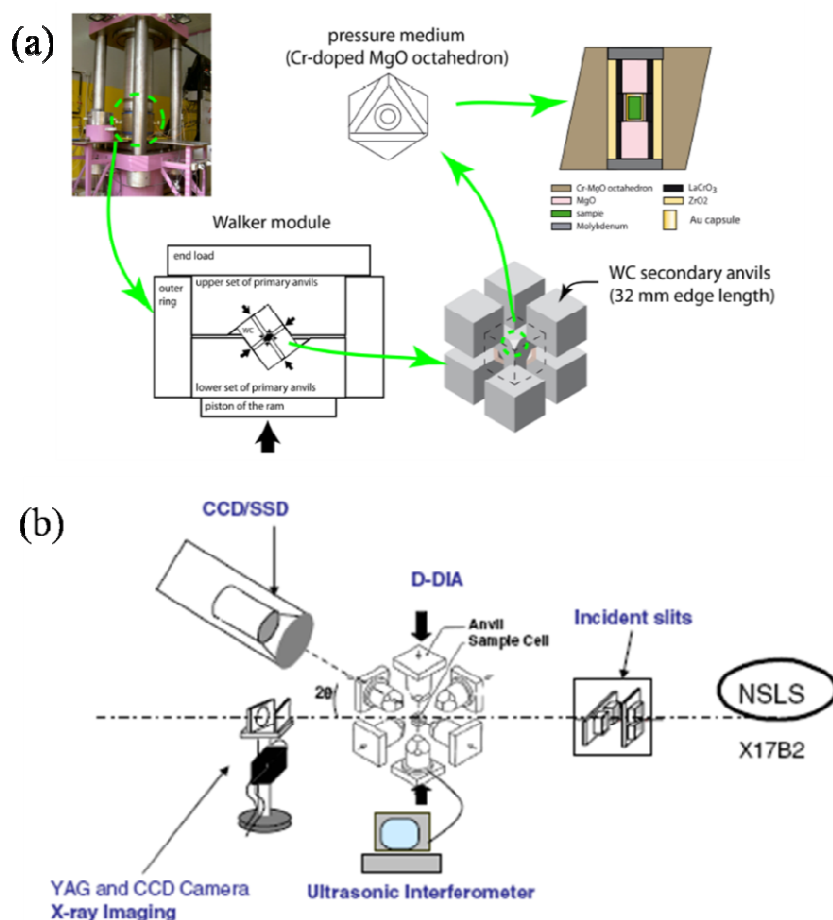


Figure 1.6 (a) The high pressure testing machine and the multi-stage loading set-up used to insure pure hydrostatic loading. [Rouxel 2008b] (b) Schematic experimental setup at X17B2, NSLS, for simultaneous pressure-volume-temperature equation-of-state and sound-velocity measurement. The thick arrows indicate the top and bottom anvils that can be advanced or retracted to minimize stress.[Antao 2008]

Antao et al. [Antao 2008], used ultrasonic measurements at pressure, performed using a DIA-type (see figure 1.6b), large volume apparatus (SAM85) in conjunction with in situ energy-dispersive x-ray techniques, as shown in figure 1.6b. This apparatus can provide a minimum observing in the shear-wave velocity, associated anomalous behavior in specify Poisson's ratio, and changes in elastic moduli.

Furthermore, Sato and Funamori, et al [Sato 2008, Sato 2010], developed synchrotron x-ray absorption and diffraction techniques for measuring the density and structure of SiO<sub>2</sub> glass at high pressures as high as 100 GPa. Wakabayashi et al. [Wakabayashi 2011], studied the compression behavior of fully densified SiO<sub>2</sub> up to 9 GPa at room temperature and found an elastic behavior and the increase in bulk modulus vis-a-vis non densified on samples.

In general, in 2000s, the techniques can provide entire samples after high pressure decompression up to 25 GPa. Sato et al., developed such a technique to get the in-situ experimental density of silica under very high pressure. Therefore, using these apparatus, it will help us to understand the densification mechanism.

### 1.3.1.4 Densification behavior under high-pressure

#### ● Silicate glass family

##### 1) Vitreous glass

In Bridgman and Simon's work, a threshold pressure near 10~12 GPa was observed in silica glass: below the threshold no effect of densification took place and above the threshold densification level increased sharply [Bridgman 1953, Bridgman 1955]. It is worthy to mention that they used the nominal pressure to calculate their high pressure and used a floating method to obtain the sample or fragments' density. According to their work, densification of vitreous glass will reach a maximum value about 6-7% for the center fragments when a pressure as high as 20 GPa (nominal). More importantly, they obtained the density of the vitreous silica at the edge as high as  $2.61\text{g/cm}^3$ , as compared with  $2.22\text{ g/cm}^3$  of original (17.5% increase, see table 1.4), quite close to the density of quartz ( $2.65\text{g/cm}^3$ ). The irreversible increase of density with pressure is shown in figure 1.7. However, x-ray diffraction measurements performed indicating that compaction proceeds at the atomic scale leaving the short-range order of the basic structural units unchanged. Besides, an appreciate increase in the permanent effect is found at higher temperatures. For example, the maximum permanent densification pressure drops from 20 GPa at room temperature to 17 GPa at  $150^\circ\text{C}$  [Bridgman 1953].

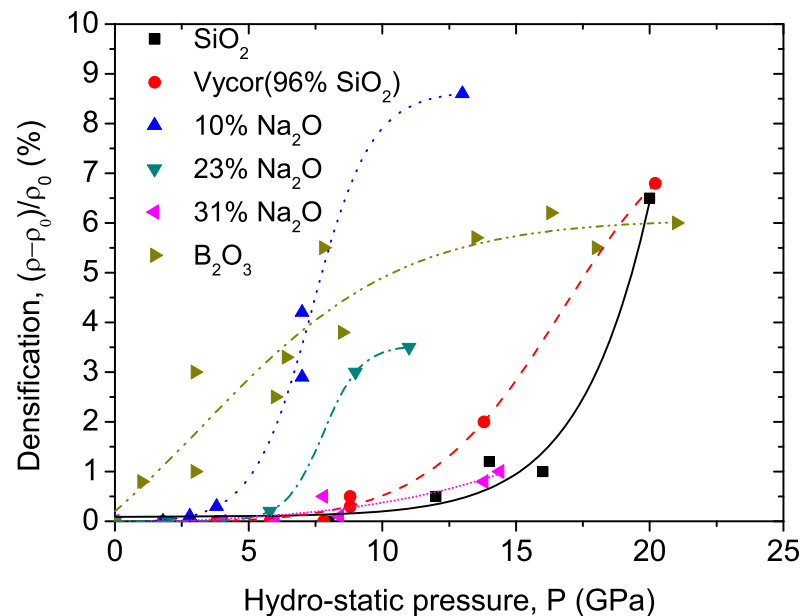


Figure 1.7 Relative increase of density of glasses [Bridgman 1953].

Cohen and Roy used their powdered samples (40-80 $\mu\text{m}$ ) to carry out high pressure experiments [Cohen 1961]. Refractive indices were measured by the oil-immersion technique and densities by the sink-float technique. They found that the 6-7% density



increase found by Bridgman and Simon at a reported 200 kilo bars was achieved in their lab at a pressure of 55 kilo bars at room temperature and found the index of  $\text{SiO}_2$  increase from 1.458 to 1.545 at 200 kilo bars, meaning that silica glass can reach ~18% of densification. Furthermore, at each pressure and temperature the respective glasses studied attained an apparent metastable equilibrium volume in a very short time and they suggested the densification of silica glass may be used as a standard for pressure calibration.

Christiansen, Kistler and Gogarty [Christiansen 1962], used silver chloride- or lead-modified type pressure cells to compare with normal high pressure experiments to study the irreversible compressibility of silica glass as a means for determining the distribution of force. Their investigation is: i) a symmetrically load from center to edge of the disks at lower pressure and ii) an unsymmetrical load at higher pressure. Their work explained the issue why only 6-7% percentage of densification was found by Bridgman and Simon. Besides, they suggested the shearing action was necessary for a permanent increase in density with pressure.

Mackenzie studied the densification of silica glass in rigid state under different conditions of shear [Mackenzie 1963a, Mackenzie 1963b]. In every case of their investigation, densification was much greater under conditions of larger external shear, i.e., with the alumina cell. For example, at 40 kb and 400 °C for 2 minutes densification in an alumina cell was 6.0% whereas none was obtained in their silver chloride cell. At 60 kb and 400 °C, the densification values after 2 minutes in alumina and in silver chloride cells were 12.8 and 5.0% respectively. They presumed that if  $(\Delta V)_e$  is the “elastic” decrease of the specific volume of a glass during compression as given by the measured compressibility and  $(\Delta V)_s$  is the shear-induced volume change after compression, the ratio  $(\Delta V)_s/(\Delta V)_e$  should provide a measure for the variation of the effect of shear with pressure. In general, he considered that densification increased with time, temperature, pressure, and more important with applied shear.

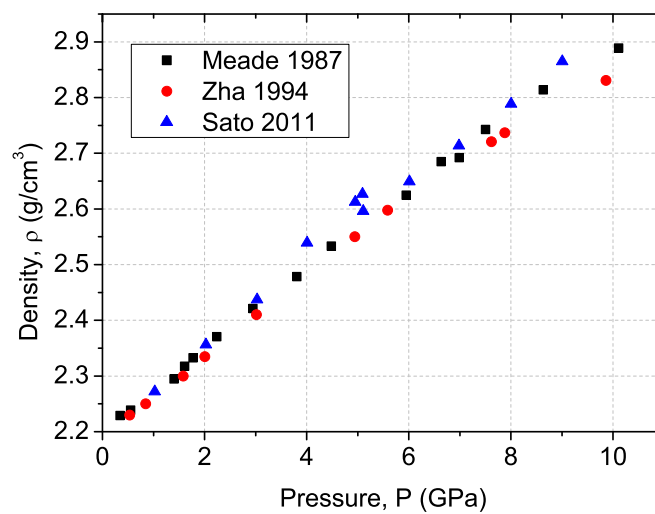


Figure 1.8 Hydrostatic pressure compression below 10 GPa.  
[Meade 1987, Zha 1994, Sato 2011]

Meade et al., calculated density via an elastic behavior and measured the sound velocity [Meade 1987]. In their experiments, irreversible compaction of fused silica is precipitated by shear stresses above 10 GPa. The density changes with pressure are shown in figure 1.8. Zha et al., using Brillouin scattering method in diamond cells, obtained the ultra sonic sound velocity and refractive index of SiO<sub>2</sub> up to 57.5 GPa at room temperature. They presented their accurate measurement of density up to 10 GPa, as shown in figure 1.8.

Recently, Sato et al., developed synchrotron x-ray absorption and diffraction techniques for measuring the density and structure of non crystalline materials at high pressures and have applied them to study the behavior of SiO<sub>2</sub> glass [Sato 2008]. Below 10 GPa, the densities as shown in figure 1.8. It seems the same as Meade and Zha et al., results. Moreover, they measured the densities up to 50 GPa as shown in figure 1.9. The solid line represents the equation of state for six fold coordinated amorphous polymorph of SiO<sub>2</sub> ( $\rho=3.88$  g/cm<sup>3</sup>, bulk modulus  $K_0=190$  GPa). They suggested that SiO<sub>2</sub> glass behave as a single amorphous polymorph having a six fold-coordinated structure at pressure above 40-45 GPa up to at least 100 GPa.

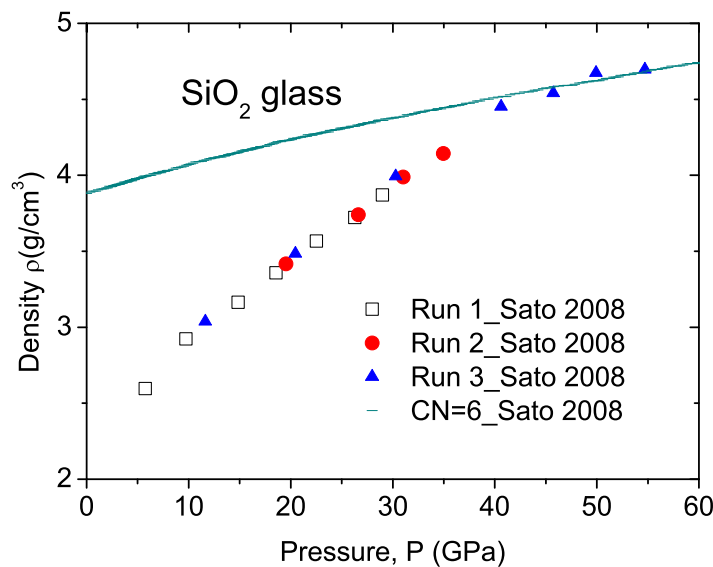


Figure 1.9 Pressure dependence of density of SiO<sub>2</sub> glass [Sato 2008].

Wakabayashi, et al., studied the compression behavior of fully densified SiO<sub>2</sub> glass up to 9 GPa [Wakabayashi 2011] as shown in figure 1.10. They observed a remarkable agreement between the volume data on compression and decompression, and confirmed that the fully densified glass behave in an elastic manner. Furthermore, they used x-ray diffraction and Raman scattering measurements to show the first sharp diffraction peak and the main Raman band of the glass. They suggested that the compaction of interstitial voids dominates in compression mechanisms of densified SiO<sub>2</sub> glass, similar to the case for ordinary of SiO<sub>2</sub> glass took place between 9 and 13 GPa at room temperature.

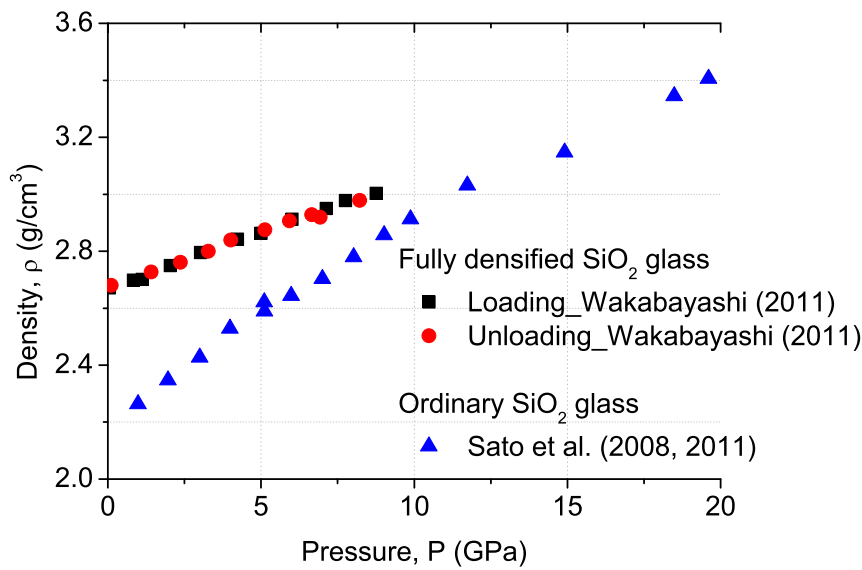


Figure 1.10 Pressure dependence of the density of fully densified  $\text{SiO}_2$  glass at room temperature [Wakabayashi 2011].

## 2) Silica-soda glasses

Silica-soda glasses manufactured with a composition of  $\text{Na}_2\text{O}$  out of silica matrix are considered here. According to Bridgman's work, three glasses with molar percentages 10 percent, 23 percent, and 31 percent  $\text{Na}_2\text{O}$  (see figure 1.7), all have a threshold pressure in the vicinity of 4 GPa [Bridgman 1953]. At the same time, a marked decreasing of the permanent compressibility with increasing content of soda. Evidently, with the increasing number of metallic cations embedded in the interstices of the silica network, a permanent change of the structure becomes more difficult.

## 3) Silica-alkali glasses

The most important characteristic of silica-alkali glasses is that, in the silica network, there are different kinds of alkali cations, such as  $\text{M}_2\text{O}$  ( $\text{M}=\text{Li}, \text{Na}, \text{K}, \text{Rb}, \text{Cs}$ , etc.). The difference of cations with different size involved inside the silica network presents important effect of their densification behavior. Normally, the increasing of cation's size would make a decreasing effect of densification ability. Recently, Ji et al., found that the densification threshold of a Windows glass (a kind of soda-lime glass) was around 8 GPa and its densification saturation value around 6.5% which may be universal to silica-alkali glass family, as listed in Table 1.4.

Table 1.4 Experimental Data for Glasses

Material	Dimension		Apparatus	T (°C)	P (GPa)	$\Delta\rho/\rho_0$ (%)	references
	Diameter	Thickness					
Vitreous Silica	5-8 mm	0.15-0.25 mm	CCA	RT	20	17.5	[8]
SiO <sub>2</sub>		40-80 $\mu$ m		RT	5.5	7	[76]
SiO <sub>2</sub>	0.24 in.	0.006 in.	DAC, lead ring	RT	14	10.97	[14]
SiO <sub>2</sub>	4 mm	7-13 mm	USSA-2000	RT	16	20	[84]
Fused SiO <sub>2</sub>	100 $\mu$ m	10-20 $\mu$ m	DAC, Mao-Bell cell	RT	10	24	[57]
Fused SiO <sub>2</sub>	100 $\mu$ m	10-20 $\mu$ m	DAC, Mao-Bell cell	RT	12.9	25	[57]
Fused SiO <sub>2</sub>	100 $\mu$ m	10-20 $\mu$ m	DAC, Mao-Bell cell	RT	14.6	24	[57]
SiO <sub>2</sub>			DAC, Mao-Bell cell	RT	24	22	[69]
SiO <sub>2</sub>			DAC, Mao-Bell cell	RT	15	20	[69]
SiO <sub>2</sub>			DAC, Mao-Bell cell	RT	16	19.6	[110]
SiO <sub>2</sub>	2 mm		OMAA	RT	20	20	[43]
SiO <sub>2</sub>	10 mm	0.8 mm	Shock loading	RT	21	19	[83]
SiO <sub>2</sub>		40-80 $\mu$ m			16	18	[15][16]
SiO <sub>2</sub>	3.7-4 mm	2 mm	BA	600	10	15	[3]
SiO <sub>2</sub>	2 mm	2 mm	OAA, Al <sub>2</sub> O <sub>3</sub> cell	400	6	14	[52]
SiO <sub>2</sub>	2 mm	2 mm	OAA, AgCl cell	400	6	4	[52]
SiO <sub>2</sub>		40-80 $\mu$ m		300	4	4	[51]
SiO <sub>2</sub>		40-80 $\mu$ m		500	4	10	[51]
SiO <sub>2</sub>	2 mm	2 mm	OAA, AgCl cell	300	4	0	[52]
SiO <sub>2</sub>	2 mm	2 mm	OAA, AgCl cell	500	4	1.5	[52]
Fused silica	2 mm	2 mm.	OAA, Al <sub>2</sub> O <sub>3</sub> cell	500	6	12.32	[52]
Fused silica	2 mm	2 mm	OAA, Al <sub>2</sub> O <sub>3</sub> cell	600	7.5	17	[52]
Fused silica	2 mm	2 mm.	OAA, AgCl cell	500	6	10.5	[52]
Fused silica	2 mm	2 mm.	OAA, AgCl cell	600	8	18.1	[52]
Ca-Mg-Na glass(79.6%SiO <sub>2</sub> )	100 $\mu$ m	10-20 $\mu$ m	DAC, Mao-Bell cell	RT	11.5	5	[57]
Vycor glass			CCA	RT	20	6.8	[8]
Window Glass	1.0 mm	2 mm	OMAA	RT	20	6	[74]
Silica-soda glass(10mol.%Na <sub>2</sub> O)			CCA	RT	13.6	8.7	[8]
Silica-soda glass(23mol.%Na <sub>2</sub> O)			CCA	RT	10.9	3.5	[8]
Silica-soda glass(31mol.%Na <sub>2</sub> O)			CCA	RT	13.8	0.7	[8]
Silica-alkali glass(22mol.% Li <sub>2</sub> O)			CCA	RT	11.2	6.9	[8]
Silica-alkali glass(23 mol.% K <sub>2</sub> O)			CCA	RT	12.8	1.2	[8]
B <sub>2</sub> O <sub>3</sub>			CCA	RT	8	~6	[8]
B <sub>2</sub> O <sub>3</sub>	2 mm	2 mm.	OAA, Al <sub>2</sub> O <sub>3</sub> cell	25-75	11	5	[52]
GeO <sub>2</sub>	2 mm	2 mm	OAA, Al <sub>2</sub> O <sub>3</sub> cell	25	7.5	10	[52]
GeO <sub>2</sub>	2 mm	2 mm.	OAA, Al <sub>2</sub> O <sub>3</sub> cell	25	7.5	10	[52]
GeO <sub>2</sub>	2 mm	2 mm.	OAA, Al <sub>2</sub> O <sub>3</sub> cell	250	7.5	13	[52]
GeO <sub>2</sub>	2 mm	2 mm.	OAA, Al <sub>2</sub> O <sub>3</sub> cell	400	7.5	16	[52]
GeO <sub>2</sub>			MAA	RT	10	11	[77]
GeSe <sub>4</sub>	2 mm	1.9 mm	OMAA	RT	3	1.5	[74]

GeSe <sub>2</sub>			LVMA	RT	9.6	4.8	[1]
F <sub>57</sub> Ba <sub>15</sub> Eu <sub>5</sub> Zr <sub>3</sub>				RT	3	3	[61]
Zr <sub>55</sub> Cu <sub>30</sub> Al <sub>10</sub> Ni <sub>5</sub>	2 mm	2.0 mm	OMAA	RT	20	2	[74]
Ce <sub>75</sub> Al <sub>25</sub>	50 $\mu$ m	50 $\mu$ m * 12 $\mu$ m	DAC	RT	24.4	8.6	[109]

Note: Carboly compression apparatus (CCA) ; opposed-anvil type apparatus (OAA); Multi anvil press apparatus (MAA); Belt type apparatus (BA); Diamond anvil cell (DAC) ;Large volume multi anvil (LVMA) ; Octahedral multi-anvil apparatus (OMAA)

## ● Boric oxide glass

Bridgman and Simon studied vitreous boric oxide under high pressure and found that B<sub>2</sub>O<sub>3</sub> exhibited much higher permanent changes in density in the region of low pressures compared to silica glasses, and there was no observed threshold pressure. Furthermore, they indicated that B<sub>2</sub>O<sub>3</sub> probably had an asymptotic increase of near 6 percent as shown in figure 1.7. Moreover, the reductions in thickness observed with vitreous B<sub>2</sub>O<sub>3</sub> were as much as 58 percent after compression to 200 katm. X-ray diffraction showed a part of vitreous B<sub>2</sub>O<sub>3</sub> became crystal on the surface of the sample during exposure in the moist air after compression. They considered that B<sub>2</sub>O<sub>3</sub> had incomplete volume elasticity even at comparatively low hydrostatic pressures and the compacting seemed to reach saturation at pressures of the order of 10 GPa. Cohen and Roy also demonstrated that B<sub>2</sub>O<sub>3</sub> glass tend to crystallize when subjected to high pressure for several days at room temperature and several hours at temperatures above 300 °C [Cohen 1961]. Mackenzie found the specific volume of densified boron trioxide glasses increased with time at room temperature. Moreover, densification increased with temperature and pressure. The use of higher pressure or temperature was unfeasible for its crystallization.

## ● Germanate glasses

Mackenzie [Mackenzie 1963a, Mackenzie 1963b] carried out a few experiments on germanium dioxide GeO<sub>2</sub>, all in alumina cells. The results together with those of Cohen and Roy, show that similar to silica, densification increased with increasing temperature at any pressure and their densification values increased from 9~10% at room temperature to 16% at the temperature of 400K with the high pressure around 75GPa (as shown in Table 1.4).

## ● Chalcogenide and chalcohalide glasses

Recently, Ji and Rouxel undertook the densification experiments of a GeSe<sub>4</sub> chalcogenide glass by means of an octahedral multi-anvil apparatus using a Walker cell [Rouxel 2008b]. Interestingly, compared with the previous reported work of silicate glass, no observed threshold pressures of GeSe<sub>4</sub> exist during the process with pressure loading which has a saturation of densification about only 1.5% and a very lower saturation pressure around 3 GPa [Rouxel 2008a].

Meanwhile, Antao et al., [Antao 2008] using large-volume multi-anvil apparatus, with simultaneous pressure generation and ultrasonic measurements, observed the effect on shear and compression wave velocities during the densification process in amorphous GeSe<sub>2</sub>. They found that the initial density of the sample was ~4.2 g/cm<sup>3</sup> and the density of the recovered sample after high-pressure ultrasonic study was 4.4 g/cm<sup>3</sup> around 9.5 GPa, which means 4.8% percentage of densification for GeSe<sub>2</sub>.

### ● Bulk metallic glasses (BMG)

Bulk metallic glasses have very high atomic packing density ( $c_g > 0.7$ ) and high Poisson's ratio ( $\nu \sim 0.38$ ), such as Zr<sub>55</sub>Cu<sub>30</sub>Al<sub>10</sub>Ni<sub>5</sub>. The high pressure effect of Zr<sub>55</sub>Cu<sub>30</sub>Al<sub>10</sub>Ni<sub>5</sub> has been explored in the work of Ji and Rouxel in 2008 [Ji 2007, Rouxel 2008a]. They found that the saturation value of densification of Zr-based BMG is about 2%, only 10% of the value of vitreous silica glass at the same condition (room temperature). More recently, Zeng, Jiang, et al., carried out high pressure experiments to Ce<sub>75</sub>Al<sub>25</sub> metallic glass, and found an amorphous to amorphous transition during the densification process between 1.5 GPa and 5 GPa with a large volume reduction of about 8.6% at ambient pressure [Zeng 2010].

In general, appreciating the work done by Bridgman and Simon, Cohen and Roy, Christiansen, Kistler and Gogarty, Mackenzie, Grimsditch, Meade, Polian, Zha, Ji, Rouxel, etc., we can find two kind of densification phenomenon in inorganic glasses, one has threshold and the other not. Normally, silicate glasses have five common features for densification behavior as below.

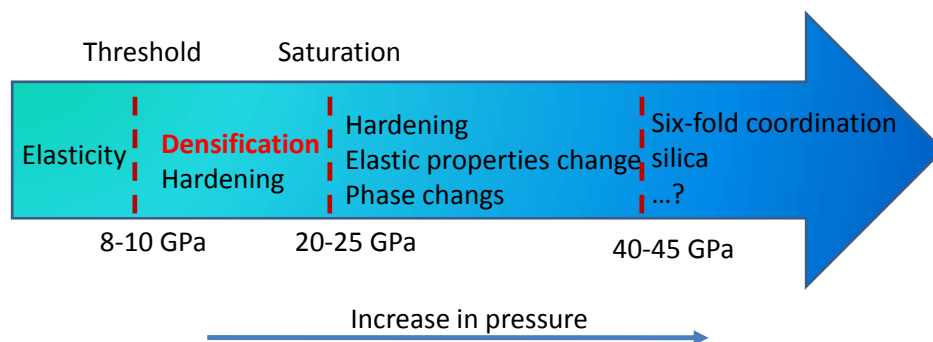


Figure 1.11 Densification under high pressure.

- i) Densification increases with pressure. Permanent densification starts from a threshold pressure and reaches saturation as high as 20% around 20~25 GPa at room temperature.
- ii) Densification kinetics increases with temperature while the saturation is value normally the same as that at room temperature. Annealing experiments show that the volume change will be easier and the density turns to be lower.
- iii) Densification increases with time until reaching the saturation level.

- iv) Impurities (network modifiers) decrease the densification threshold of pressure and make the silica network permanent deformation more difficult. The saturation value of densification is around 6%.
- v) For silica glass, if pressure is higher than 27 GPa, an amorphous phase change will happen [Sato 2008, Sato 2010].

On the other hand, boric oxide glass exhibits a different law of densification under high-pressure loading studies compared to silica glasses, which has three important characteristics as below:

- i) No observed threshold pressure, the permanent change in density begins at a low pressure.
- ii) Asymptotic increase in density up to a value around 6 percent.
- iii) Crystallization under the high-pressure loading.

### 1.3.2 Indentation and densification

#### 1.3.2.1 Indentation and cracks

The ability to form crack-free permanent indentations in glasses at fairly low indenter loads has been attributed to the ‘plasticity’ of glasses which are generally regarded as ideal brittle solids [Hagan 1978]. Some scientists have attributed ‘plastic’ deformation in glasses to (i) densification or compaction of ‘porous and open’ glass structure [Peter 1964, Evers 1967] and (ii) to local and transient heating which modifies the viscosity to accommodate the deformation even at room temperature [Bastick 1950], especially at very rapid loading rates. According to Douglas [Douglas 1958], at the very high shear stresses generated at the moment of sample-indenter contact, the viscosity drops to accommodate the deformation by increasing the contact area till the pressure has dropped to such level that the viscosity rises again to its normal value (pressure induced fluidity).

In detailed studies on the deformation behavior of glasses, Peter has shown that densification beneath the indentation as well as flow of glass is remarkably during indentations [Peter 1970]. According to Peter’s work, the blunter the indenter, the more deformation occurs in terms of densification, and the less in terms of plastic deformation. He observed the deformation of a ‘rosette’ pattern of flow lines during the last stages of the densification process. These flow lines were similar to the slip line systems observed under punch indentations of ideally plastic materials undergoing radial flow [Nadai 1931]. The observation of glass deformation under indenter has been illustrated clearly recognized as lateral cracks and cone cracks by Hagan and Swain [Hagan 1978]. Lateral cracks emanate from the bottom of the deformed zone and are produced during unloading by residual stresses while the cone cracks turning up and propagating in the saucer-shaped fashion towards the surface and removing the flange of the cone. Sometimes these lateral cracks start not at the tip of the cones but at the points on the ‘skirt’ of the cone which may be caused by the frictional forces in the deformation process. For both Vickers and spherical indentations the radial stresses are tensile at or outside the contact circle and at high enough stress levels these can initiate shallow cracks which reflect the symmetry of indenter.

From Hagan’s work, it is clear that small changes in material properties can affect the details of the failure processes beneath an indenter. These, in turn, will have important effects on the wear, abrasion and erosion of these solids. The nature of flow lines that occur in the deformed zone in soda-lime glass under pyramidal indentations has been investigated by Hagan in 1980 [Hagan 1980]. A close examination of the deformed zone show that spiral flow lines meet as they required by the ideal rigid-plastic behavior. Evidence of void or cracks formation at the intersection points or along the flow lines is also presented, along with a possible hardening effect from the suppression of slip at the intersection points of the flow lines.

In summary, inorganic silicate glasses, once densified, a region tends to shrink,



straining the interface between it and the original solid as the network is densified (compacted) to as near the maximum density as possible. Meanwhile, shear flow at some local weakness (provided by the network modifiers) and the subsequent flow are by dilation of the structure in the immediate vicinity of the initiation site.

### 1.3.2.2 Quantitative evaluation of indentation-induced densification

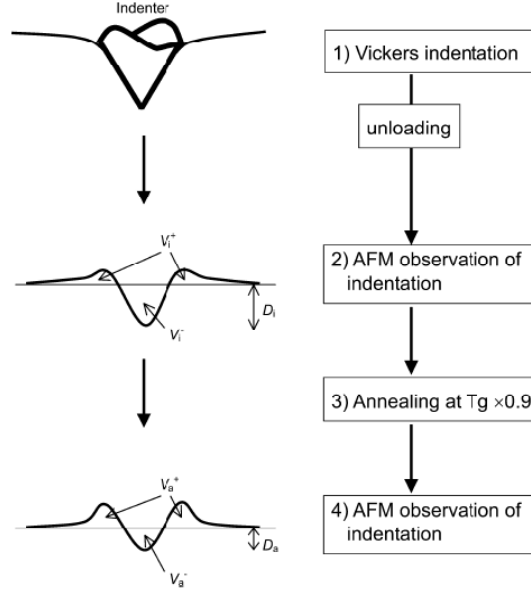


Figure 1.12 Schematic illustration of the procedure for measuring the indentation volume before and after annealing [Yoshida 2005].

Up to now, elasticity, plasticity, hardening and densification may contribute to the deformation of materials, especially under indentation, but the role of their contribution is still confused. A quantitative evaluation of indentation-induced densification in glass method has been brought forward in the work of Yoshida, et al. [Yoshida 2005]. On the assumption that an indentation impression can be partially recovered by thermal annealing [Neely 1968] and based on the fact that the viscous flow kinetics is very slow in comparison to the experimental time, they considered that complete recovery of the densified region under  $0.9 T_g$  and 2 h was feasible.

As shown in figure 1.12, atomic force microscope (AFM) observations can be used to lead a quantitative evaluation of indentation-induced densification. The volume ratio of annealing recovery  $V_R$  as the volume ratio calculation is defined as following

$$V_R = \frac{(V_i^- - V_a^-) + (V_a^+ - V_i^+)}{V_i^-} \quad (1.2)$$

Where indentation volume  $V_i^-$ , and pile up volume  $V_i^+$  are measured before annealing while indentation volume  $V_a^-$ , pile up volume  $V_a^+$  are measured after annealing. Therefore, both the changes of the piling up,  $(V_a^+ - V_i^+)$ , and of the

indentation volumes,  $(V_i^- - V_a^-)$ , are assumed to be constituents of the densified volume [Yoshida 2005].

Using this quantitative evaluation method, they found that all glasses but BMG exhibited densification but to different extents. Densification under a Vickers indenter is thus a general property for silicate glasses. In their investigation, they consider densification contribution 79%, 61% and 41% of the indentation volume in the case of 10 MgO glass, soda-lime glass and 20 CaO glass, respectively. Furthermore, they argue that the compositional variation correlated with the compositional variation of Poisson's ratio. It means that there exist a good correlation between the ratio of densification to the total indentation volume and Poisson's ratio in glass.

Quantitative investigation of densified beneath a Vickers indenter by means of AFM topometry results in a densified volume representing as much as 68% of the post-unloading indentation print of window glass which has the saturation of densification about 6% and that 92% for a-SiO<sub>2</sub> that has a 20% densification under high pressure [Ji 2006]. More recently, Kato [Kato 2010] used quantitative evaluation method to study the crack initiation property. According to their work, the crack resistance has a strong relationship with densification. Glass experiencing larger densification around the indentation shows higher crack resistance. They suggested that densification was assumed to reduce residual stress around the indentation, resulting in an increase in the crack resistance. Anyhow, densification plays a great role in the deformation and cracking phenomena in glass under sharp contact and this quantitative evaluation method may help us to understand its contribution during those processes.

### 1.3.3 Shock wave compression and structure

#### 1.3.3.1 Densification and shock compression

Early studies documented that the material can be densified under static pressure at ambient or high temperature conditions. Compaction begins at 8 to 10 GPa at room temperature, below which the compression remains elastic for some kind of silica glass. The glass also can be densified under shock loading [Zha 1994, Sugiura 1997].

Silica glass (fused silica) and quartz have been extensively studied by shock wave methods. SiO<sub>2</sub> glass behaves as a nonlinear elastic solid under compression to 9-10 GPa [Sugiura 1997, Inamura 2004]. Recovered samples from shock compression at 10-16 GPa show evidence for permanent densification. SiO<sub>2</sub> glass begins to undergo a high-pressure phase transition to a high-density structure at about 16 GPa and this transformation is complete at 30 GPa. At pressures near 70 GPa, discontinuities in shock temperature and sound velocity have been interpreted as shock-induced melting [Zha 1994].

Using multiple shock reverberation method, Sugiura, et al., found repeat densification phenomena of silica glass [Sugiura 1997]. The limit of increase in density was about 2.47 Mg/mm<sup>3</sup> after the first shock loading, while the limit increased to 2.55 Mg/mm<sup>3</sup> after duplicate shock loading. Interestingly, triplicate shock loading

was not so effective for the increase in density. Using Raman spectrum, they found an enhanced line D2 to explicate the inside structure modification of the densified silica glass, as shown in figure 1.13. It means that the history of shock loading is reproduced by similar treatment in static compression, although there are large differences in temperatures between shock compression and static compression followed by heat treatment.

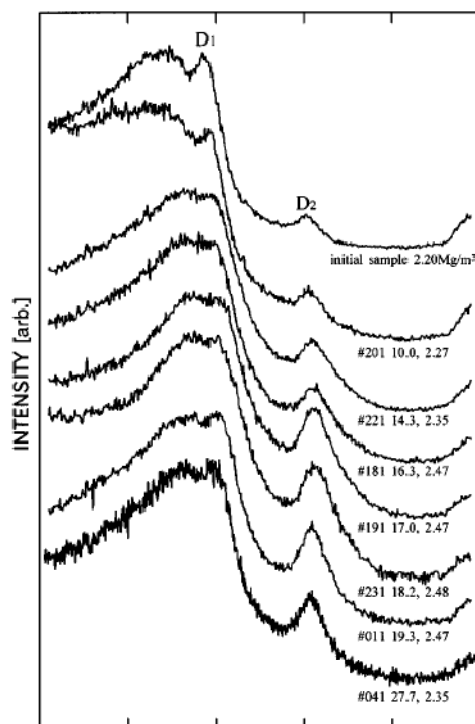


Figure 1.13 Raman spectra of densified silica glasses after single shock reverberations. Values next to sample numbers are peak pressures in GPa during shock loadings and densities in  $\text{Mg/m}^3$  after loadings [Sugiura 1997].

### 1.3.3.2 First sharp diffraction peak study

The irreversible densification of vitreous silicon oxide subjected to pressures above 12 GPa has been well known for several decades. Although Raman spectroscopy shows that the microscopic arrangement of the atoms is radically changed in the densified material, almost no clearly structural information is available. Neutron scattering is one of the most powerful tool to study the structure of amorphous materials, but the limited ability to cover a grand range of wave vectors makes it hard to be applied to unravel the structure information directly. In the early 1990s', Susman, et al., combined neutron-diffraction and molecular-dynamics (MD) together to study the structure changes [Susman 1991]. They found that the static structure by neutron diffraction was in good agreement with those obtained in the MD calculations. Both experiment and MD simulation show that there is no appreciable change in the short-range order (SRO), viz. the  $\text{Si}(\text{O}_{1/2})_4$  tetrahedral, but there is a significant effect on the first sharp diffraction peak (FSDP)- the fingerprint of the

mediate-range order. In their results, the densified vitreous silica, compressed to 16 GPa and its density increase 20% compared to normal ones, show substantial changes in the FSDP: an indication of modification in the intermediate-range order. They argue that the changes in the FSDP are due to increased frustration caused by the decrease in the Si-O-Si bond angle and a shift in the Si-Si and O-O correlations in the range of 4-8 Å toward lower distances.

Recently, Katayama and Inamura used a special method to explore a series high-temperature and high-pressure experiments which were performed on BL14B1 at Sping-8 using a cubic-type multi-anvil press, with a X-ray diffraction apparatus inside [Inamura 2004]. Using synchrotron radiation, they measured the first sharp diffraction peak (FSDP) both in compression with increasing of temperature and decompression process from high temperature to room temperature. According to experiments, as the temperature was increased to 700°C at 8.5 GPa, where 20% densification exhibited, the FSDP became sharp and its position moved to higher momentum transfer place, as shown in figure 1.14.

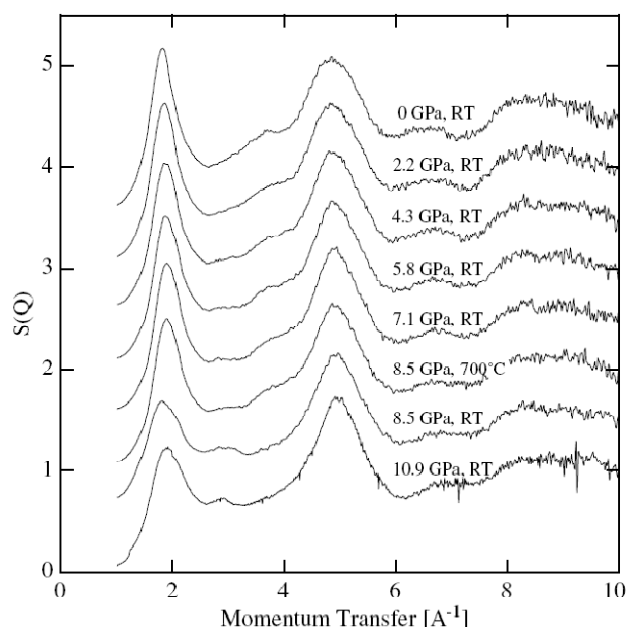


Figure 1.14 Structure factor,  $S(Q)$ , of silica glass at various pressures measured during decompression together with those 8.5 GPa and 10.9 GPa. [Inamura 2004]

The shift of the FSDP indicated that the intermediate structure is thermally relaxed to denser one. According to their work, during the decompression process, the position of the FSDP showed a large hysteresis. As the pressure decreased at room temperature, it moved to a lower momentum transfer but the total shift was smaller than that observed upon compression. Comparing with room temperature high-pressure experiments, they consider the changes of intermediate-range structure were accumulated during the compression and the heating, and the hysteresis is the main cause of the permanent densification. Therefore, they first observed the hysteresis phenomena of densification of silica glass during compression and decompression process covering a wide range of temperature before it crystallized.

## 1.4 Densification and materials' properties

### 1.4.1 Sound velocities and refractive index

Using Brillouin scattering, Polian and Grimsditch, et al., have measured the two independent elastic modulus of a-SiO<sub>2</sub> with increasing and decreasing pressures to 25 GPa [Grimsditch 1984]. They investigated both the longitudinal ( $V_L$ ) and transverse- ( $V_T$ ) sound velocities increase and decrease with pressure. They found that the longitudinal waves and the shear velocity also exhibit irreversible behavior on densification. As we know, in an isotropic material, the bulk modulus  $B$  is related to the density and the longitudinal and transverse velocities through the equation  $B = \rho(V_L^2 - 4V_T^2/3)$ . Following the procedure outlined in Refs [Shimizu 1981] and [Polian 1986], one can write the change in density as  $\rho = \int dP / (V_L^2 - 4V_T^2/3)$ , but only if no irreversibility occurs. Therefore, the bulk modulus changes with pressure during the densification can be determined but it is not possible to perform an integration as a function of pressure because of the thermodynamically irreversible processes which occur during densification. Therefore, they turned to use Clausius-Mossotti expression,  $(n^2 - 1)/(n^2 + 2) = \text{const} \rho$ , to roughly estimate the degree of densification from the determination of the refractive index which yields a densification of 22% at the pressure of 25 GPa.

According to Zha et al., [Zha 1994] acoustic velocities and refractive index of SiO<sub>2</sub> glass have been measured to 57.5 GPa at room temperature by Brillouin scattering in diamond cells. On compression, both longitudinal and transverse modes exhibit an anomalous change in slope in the low pressure region. Between 12 and 23 GPa, the sound velocities increase rapidly, as shown in figure 1.15.

At higher pressures, the bulk velocity follows a trend similar to that expected for coesite. They confirmed previous studies in which the glass was found to exhibit anomalous minima in the longitudinal and transverse velocities around 3 GPa. On decompression from 16 GPa to ambient conditions, the data show an irreversible increase in the acoustic velocities. By compression, there appears to be little hysteresis in the compression data measured at high pressure (26-57.5 GPa). Besides, they found an increase in the intensity of the shear wave on decompression from 57.5 GPa. As the densification process mainly occurs between 10 and 25 GPa, the lack of irreversible changes at pressure higher than 26 GPa is perhaps not unexpected, which

make them believed that the irreversible change of the refractive index must be the result of permanent structural densification. Generally, they found the longitudinal sound velocities were more sensitive to changes in pressure than transverse velocities, and the largest changes in the sound velocities occur between 12 and 23 GPa arising from the permanent densification.

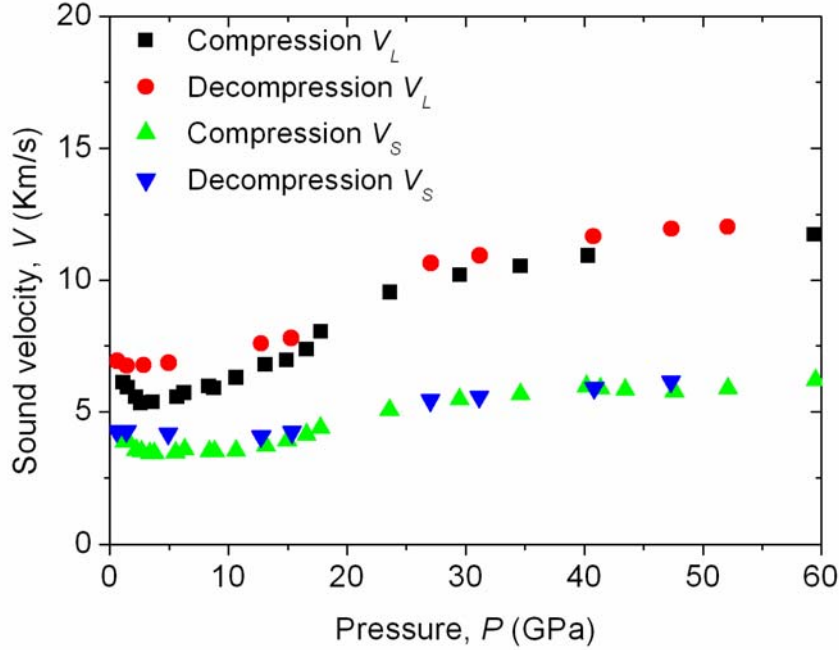


Figure 1.15 Sound velocities in SiO<sub>2</sub> glass as a function of pressure.

#### 1.4.2 Bulk modulus, elastic modulus and shear modulus

Recently, Antao et al., [Antao 2008, Antao 2007] carried out acoustic measurements using synchrotron radiation on glassy GeSe<sub>2</sub> up to 9.6 GPa. In their study, the compressional ( $V_p$ ) and shear ( $V_s$ ) velocities were calculated with measured travel times and sample lengths ( $l$ ) at different pressure using the general relationship  $V_{(p,s)} = l/t_{(p,s)}$ . At 1 GPa, they found the velocities are  $V_s = 1.76$  and  $V_p = 2.52$  km/s. The  $V_p$  increases gradually with pressure while the  $V_s$  anomalously decreases up to 4.5 GPa, and then increase to 9.5 GPa, as shown in figure 1.16a. Comparing to sound velocities investigation on SiO<sub>2</sub>, we can found that SiO<sub>2</sub> glasses exhibit anomalously minima in both longitudinal and transverse wave velocities (Figure 1.13), however, the minimum was observed only for the transverse wave velocities (S wave) at 4 GPa for GeSe<sub>2</sub>. They consider these phenomena attributed to the rigidity of GeSe<sub>2</sub>.

Furthermore, Poisson's ratio, elastic moduli can be obtained directly from the measured velocities by the equations as follows:

$$\begin{cases} \nu = \frac{V_p^2 - 2V_s^2}{2(V_p^2 - V_s^2)} \\ G = \rho V_s^2 \\ K = \rho(V_p^2 - \frac{4}{3}V_s^2) \\ L = \rho V_p^2 \end{cases} \quad (1.3)$$

Where  $\nu$  denotes Poisson's ratio,  $G$  denotes shear modulus,  $K$  denotes bulk modulus, and  $L$  denotes longitudinal modulus.

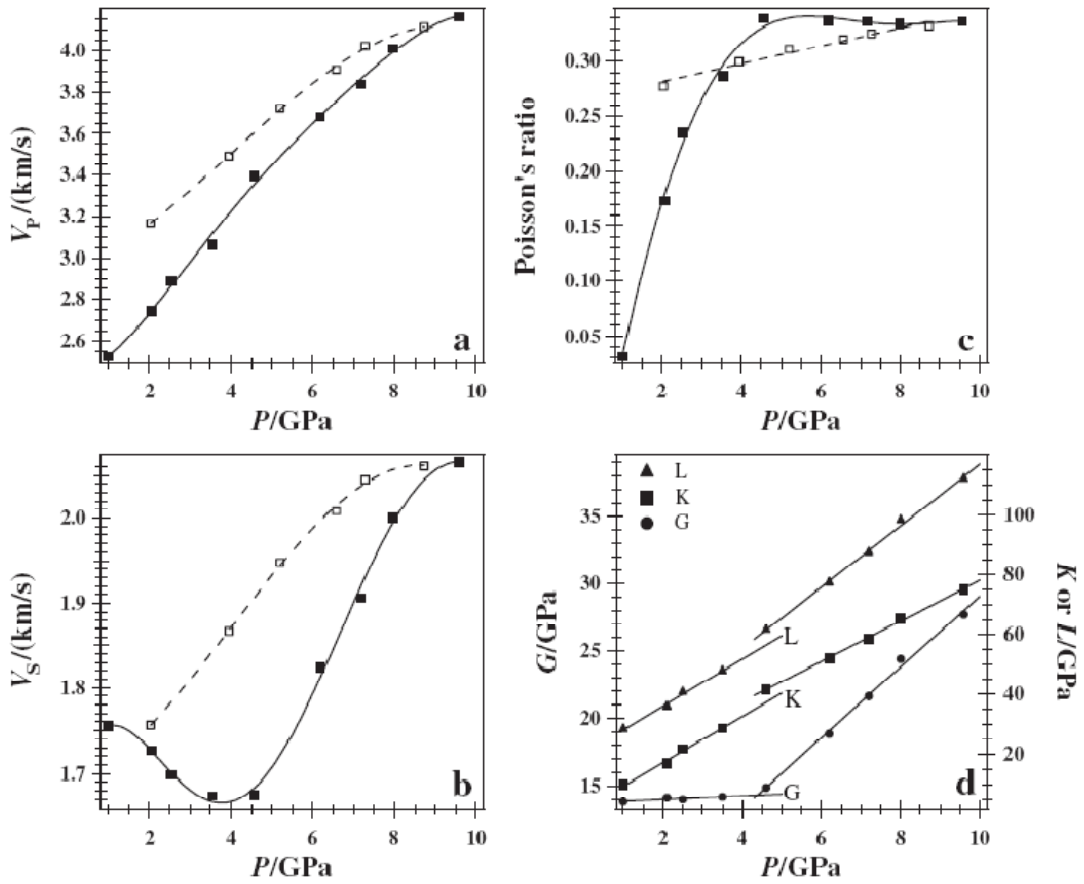


Figure 1.16 Variations with pressure, closed symbols for loading and open symbols for unloading for GeSe<sub>2</sub>. (a)  $V_p$ , (b)  $V_s$ , (c) Poisson's ratio and (d) elastic moduli [Antao 2008].

Antao et al. exhibited the changing tendency of Poisson's ratio and elastic module as shown in figures 1.16c and 1.16d, respectively. They suggested that, this anomalous behavior in Poisson's ratio and discontinuities (slopes not moduli) in

elastic moduli at 4 GPa is indicative of a gradual structural transition in GeSe<sub>2</sub>. This is attributed to a network rigidity minimum originating from a competition between two densification mechanisms. At pressure up to 3 GPa, a conversion from edge- to corner-sharing tetrahedral results in a more flexible network and this is contrasted by a gradual increase in coordination number with pressure, which leads to an overall stiffening of the glass. In general, their work provides important information on interpreting changes in the macroscopic properties of glasses with pressure when combined with structural data.

For SiO<sub>2</sub> glass, Sato and Funamori [Sato 2008], suggested that the estimated bulk modulus was consistent with the pressure dependence of the density. They determined bulk modulus at 50 GPa is 390 GPa by fitting the third-order Birch-Murnaghan equation of state to the density data with constraint from bulk sound velocity data. They also pointed that the bulk modulus cannot be precisely determined solely from the density data. Wakabayashi et al, studied the compression behavior of fully densified SiO<sub>2</sub> glass. The zero-pressure bulk modulus was determined to be  $K_0=60.2$  GPa, with its pressure derivative  $K'_0=4$  (fixed) by fitting a Birch-Murnaghan equation of state to the volume data. This value is good agreement with  $K_0 = 60 - 70$  GPa, obtained by elastic-wave-velocity measurements from Zha et al, [Zha 1994] and Rouxel et al. [Rouxel 2008a]. Moreover, they pointed out that the compression curve (Loading pressure and density curve) of fully densified SiO<sub>2</sub> glass can be expressed by the second-order Birch-Munaghan equation of state. The bulk modulus tends to increase with increasing the degree of densification.



### 1.4.3 Poisson's ratio and the high pressure densification

As mentioned in equation 1.3, Poisson's ratio,  $\nu$ , can be directly obtained from the measured sound velocities. Zha et al. [Zha 1994] measured values start from 0.19 at 0.54 GPa, decrease to  $\sim 0.15$ , then increase to about 0.30~0.35 for SiO<sub>2</sub> glass, and becoming nearly pressure independent above 23 GPa, as shown in figure 1.17.

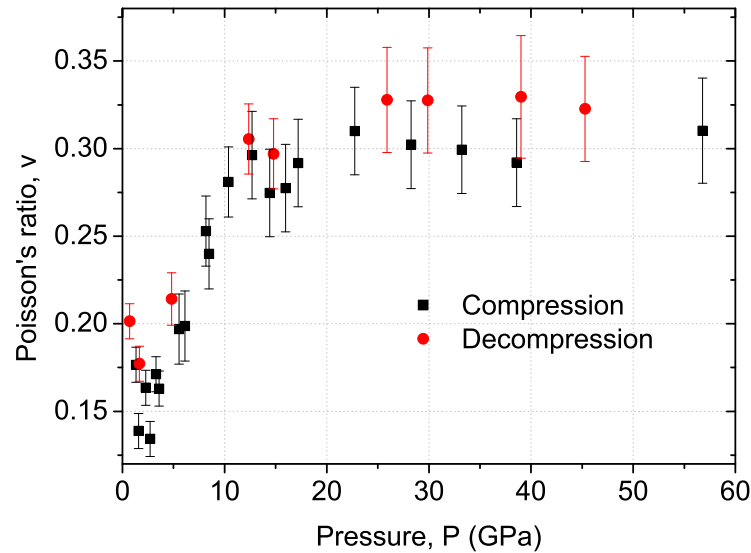


Figure 1.17 Poisson's ratio of SiO<sub>2</sub> glass as a function of pressure. Black square are increasing pressure and red circles are on decreasing pressure. [Zha 1994]

Poisson's ratio is a macroscopic elastic parameter which depends much on the fine details of the atomic packing. Glasses, with different atomic scale networks, exhibit a wide range of Poisson's ratio from 0.1 to 0.4. As a relatively low atomic

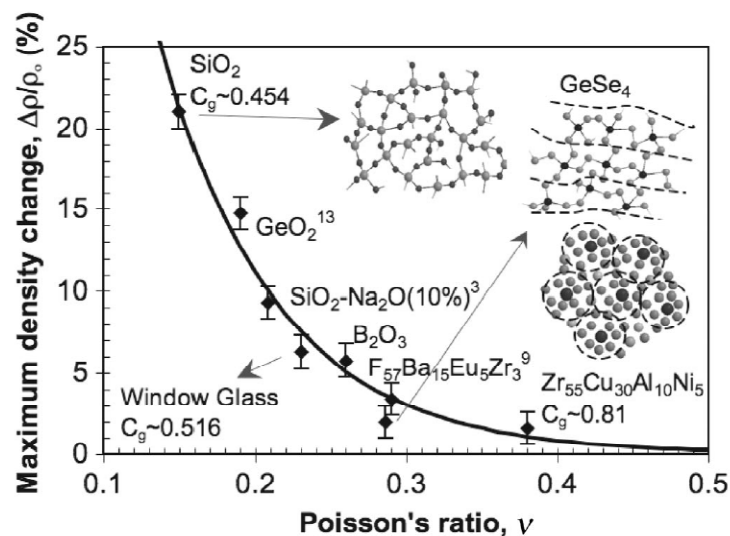


Figure 1.18 The maximum densification and Poisson's ratio among different inorganic glasses [Rouxel 2008a].

packing density ( $C_g = \rho \sum f_i V_i / \sum f_i M_i$ ), glasses present significant densification behavior under high hydrostatic pressure [Rouxel 2007].

According to the work of Rouxel et al., Poisson's ratio is correlated to the glass network connectivity. Previous experimental data show that  $\nu$  decreases monotonically with the mean coordination number ( $\langle n \rangle, n = \sum_i f_i n_i$ , where  $f_i$  and  $n_i$  are the atomic fraction and the coordination number of the  $i$ th constituent, respectively) [Rouxel 2007]. A highly cross linked network, such as amorphous silica has a small Poisson's ratio ( $\nu = 0.15$ ), while weakly correlated network, such as chain-based chalcogenide glasses or cluster-based metallic glass, exhibit much higher values than 0.3 (up to 0.4). It is worthy to note that the lower the atomic packing density is and the larger the volume change the glass experiences under high pressure (1 to 25 GPa) as shown in figure 1.18 [Rouxel 2008a].

### 1.4.4 Densification and Raman spectroscopy

Raman scattering spectroscopy is used to characterize the structure of materials. Grimsditch investigated the Raman spectra of amorphous  $\text{SiO}_2$  up to 17 GPa, and pointed that there exist a new form of amorphous  $\text{SiO}_2$  after high pressure at room temperature [Grimsditch 1984]. Sugiura et al. studied the densification behavior of silica glass by shock compression. They found that the Raman spectra of recovered silica glasses had characteristics of densified silica glass with much higher density [Sugiura 1997]. Perriot et al. have recently characterized the plastic deformation under micro-indentation in amorphous silica [Perriot 2006] which provides a new way to study the changing of densities after indentation. Rouxel et al. [Rouxel 2008a] studied structure changes of amorphous silica, window glass, and chalcogenide glass in high pressure experiments by using the Raman scattering spectroscopy. In the case of amorphous silica, the sharpening of the main band near  $500\text{ cm}^{-1}$  and its shift to higher frequency ( $427\text{ cm}^{-1}$  in the pristine glass and  $511\text{ cm}^{-1}$  after densification under 25 GPa). Deschamps et al. studied the Raman micro-spectroscopy of soda-lime silicate glass under hydrostatic pressure and indentation. The goal of their experiments is to characterize the window glass elasto-plasticity under high hydrostatic pressure and to obtain a Raman  $\leftrightarrow$  pressure calibration curve with the aim of indentation analysis. All the Raman spectra show peak located at 450, 560, 600, 800, 950 and  $110\text{ cm}^{-1}$  [Deschamps 2011]. They confirmed that the bands around 450 and  $560\text{ cm}^{-1}$  are attributed to Si-O-Si symmetric stretching vibration modes which may directly related to its changing of densities. More recently, Wakabayashi et al. investigated the main Raman band position of densified  $\text{SiO}_2$  glass at ambient conditions as a function of synthesis pressure. The zero pressure Raman spectra is about  $440\text{ cm}^{-1}$  and reach  $515\text{ cm}^{-1}$  at 9 GPa [Wakabayashi 2011].

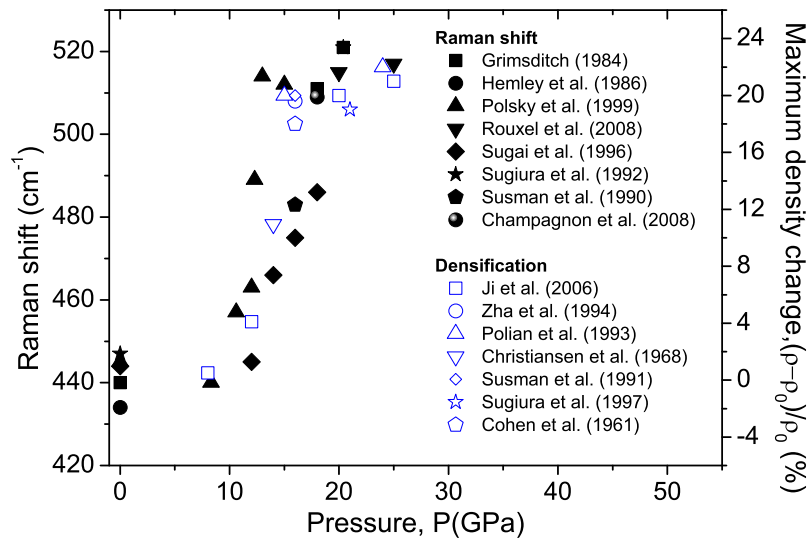


Figure 1.19 Raman shift and densification under pressure in  $\text{SiO}_2$  glass at room temperature.

Solid symbols are Raman shift data and open symbols are densification data from relevant published articles.

We collected the information of Raman scattering experiments in  $\text{SiO}_2$  glass under high pressures as shown in figure 1.19. At zero pressure state the Raman shift is  $\sim 440 \text{ cm}^{-1}$ , and then begin to increase since 8-10 GPa and reach a high value around  $510\text{-}520 \text{ cm}^{-1}$  after  $\sim 17 \text{ GPa}$ . Interestingly, we found that the Raman shift have a similar tendency as densification under high pressures.

## 1.5 Modeling of densification

### 1.5.1 Molecular-dynamic simulation

In order to obtain some insight in the densification mechanisms, scientists have performed molecular-dynamic simulations of a sample of glassy silica subjected to a hydrostatic compression and decompression process. According to several calculations, two-body interaction potentials are as effective as the three-body ones in describing both crystalline and amorphous silica [Tse 1992, Valle 1996].

As far as we know, the first available direct simulation of a compression-decompression process at room temperature was simulated and calculated by Tse et al. using the potential model proposed by van Beest, Kramers, and van Santen [Tse 1992]. They succeeded in using the two-body potential model to study the structure of amorphous  $\text{SiO}_2$  at ambient pressure and had a good agreement with experimental results. They found that the Si coordination number with oxygens in the network increases from 4 to about 5 in the material taken at 15 GPa and reaches 6 at higher pressures. Valle et al. draw the same conclusion [Valle 1996]. Besides, a densification with a volume reduction of about 20% was calculated for samples subjected to pressures of 15 GPa and the oxygen coordination number was 4.2-4.4 after unloading. Furthermore, their calculations suggested that a new crystalline phase forms at about 100 GPa.

Following the previous work, Valle and Venuti adopted the potential of Tsuneyuki et al. [Tsuneyuki 1988] which can reproduce structure, density, compressibility, and vibration frequencies of both the crystalline and amorphous forms of silica. In the densification simulation process, they found a slight increase in the average Si-O bond length accompanied by a decrease in the average angle and Si-O-Si angle and Si-Si separation. The MD results indicate that the increased atomic coordination is the main driving force behind most of the transformations encountered which can be demonstrated by the point where irreversible densification began (>6 GPa) accompanied with a coordination number of Si atoms with O greater than four. They convinced that the high-pressure instability of the tetrahedral network with respect to an increase in coordination, which triggers the irreversible transition from quartz to stishovite, is also the cause of the densification of compressed amorphous silica.

### 1.5.2 Finite element method (FEM)

Densification phenomenon in glasses caused a great interest to scientists. Using finite element method to analyze the densification problem can be traced back to the work of Imaoka and Yasui, but not many studies have been devoted to this issues [Imaoka 1976, Yasui 1982].

In Yasui and Imaoka's work, they solved a plane strain problem (two dimensional) using wedge-shaped indenter to model a series of ideal elastic-plastic  $\text{Na}_2\text{O-SiO}_2$  glasses changing the values of  $\text{Na}_2\text{O}$  from 0, 10%, 15%, 20%, 25% to 35%. They assumed the yield criterion to be of Mohr-Coulomb type (called by them as such). They introduced a densification factor  $\alpha$  into their modeling. Judging from their calculations, the maximum value of  $|\alpha|$  obtained was 0.04 and the values of  $|\alpha|$  were found to decrease as the  $\text{Na}_2\text{O}$  content of the glass was increased. Interestingly, they found  $|\alpha|$  approached to zero when the  $\text{Na}_2\text{O}$  content exceeded 35%, which means that there was no densification for such glasses. Furthermore, they found the value  $|\alpha|$  did not change too much when temperature was changed, which indicating that the  $|\alpha|$  depending only on the structure of the glass.

Based on the classical Drucker-Prager incremental elastoplastic law, Giannakopoulos, Zeng et al. [Zeng 1995, Giannakopoulos 1997] analyzed the pyramid indentation (Vickers and Berkovich indenters) of pressure-sensitive of fused silica and soda-lime glass, which related to the densification process. Although they did not take account into the densification factor, their work of indentation modeling presented a numerical calculation way to analyze the force-depth relationship (loading and unloading  $P-h$  curve), the imprint morphology (e.g., sinking-in, pile-up, cracking, etc.) and the residual stresses, which presenting a good way to interpret the densification mechanism. Besides, they caused an very important question that a good constitute model needed to establish, in order to portray the irreversible and hardening phenomenon of silica glass.

Following, Lambropoulos et al. discussed a constitutive model describing the permanent densification of fused silica under large applied pressures and shear stresses. Their constitutive law is assumed to be rate-independent and uses a yield function coupling hydrostatic pressure and shear stress, a flow rule describing the evolution of permanent strains after initial densification, and a hardening rule describing the dependence of the incremental densification on the levels of applied stresses [Lambropoulos 1996]. Their concepts of yield function, flow rule, normality, and hardening are shown in figure 1.20.

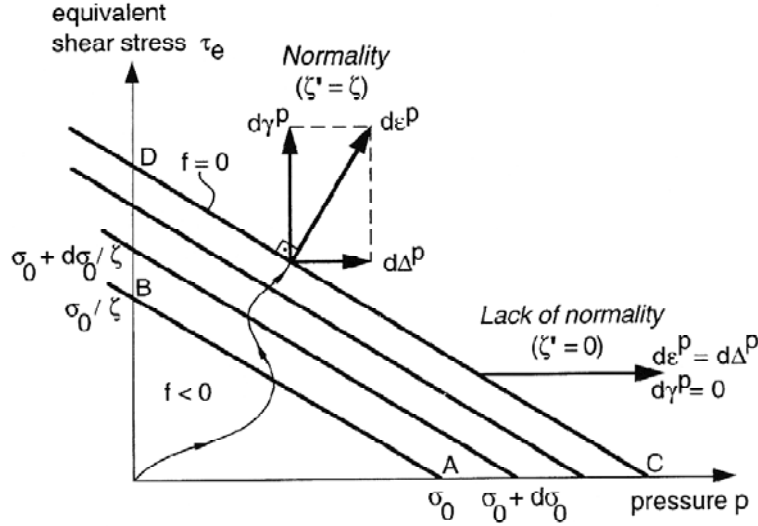


Figure 1.20 Constitutive model for the densification of fused silica [Lambropoulos 1996].

In figure 1.20, yield function describing the densification and flow (i.e., shear deformation) of silica in a stress space. The coordinates are the hydrostatic pressure  $p = -\sigma_m$  and the equivalent shear stress  $\tau_e$ . Lin AB is the initial yield surface. Subsequent two lines are yield surfaces, the current yield surface CD and a loading path. If  $\zeta = \zeta'$ , then normality is satisfied (the plastic strain increment is normal to the yield surface) and both permanent densification and shear flow result. If  $\zeta' = 0$ , then normality is not satisfied. The hardening modulus  $h$  relates increments in pressure to increments in permanent densification, i.e.,  $h = d\sigma_0 / d\Delta^p$ . They applied the constitutive law to determinate the depth of densification layer during polishing or lapping of silica.

Moreover, Xin and Lambropoulos [Xin 2000] assumed that relation of compression and shear is linear and deduced a new yield function as follows

$$f(\sigma_{ij}) = -\alpha\sigma_m + (1-\alpha)\tau_e - Y = 0 \quad (1.4)$$

Here they defined the material densification parameter  $\alpha$  ( $0 \leq \alpha \leq 1$ ) to describe the irreversible phenomenon, where  $\alpha = 0$  state for the material yields only by pure shear and  $\alpha = 1$  means only under hydrostatic compression. In this function,  $Y$  is the shear stress,  $\sigma_m$  is the mean stress and  $\tau_e$  is the equivalent shear stress. By implementing their model to a UMAT module provided by Abaqus, they tested uniaxial compression, constrained uniaxial compression simulation of fused silica. Changing the value of  $\alpha$  from 0 to 0.6, they found that for a small  $\alpha$ , the material became “softer”, but for large  $\alpha$  the material became “harder”. Using Berkovich indentation simulation, they found  $\alpha \approx 0.6$  and  $Y \approx 5.43 \text{ GPa}$  can fit both loading

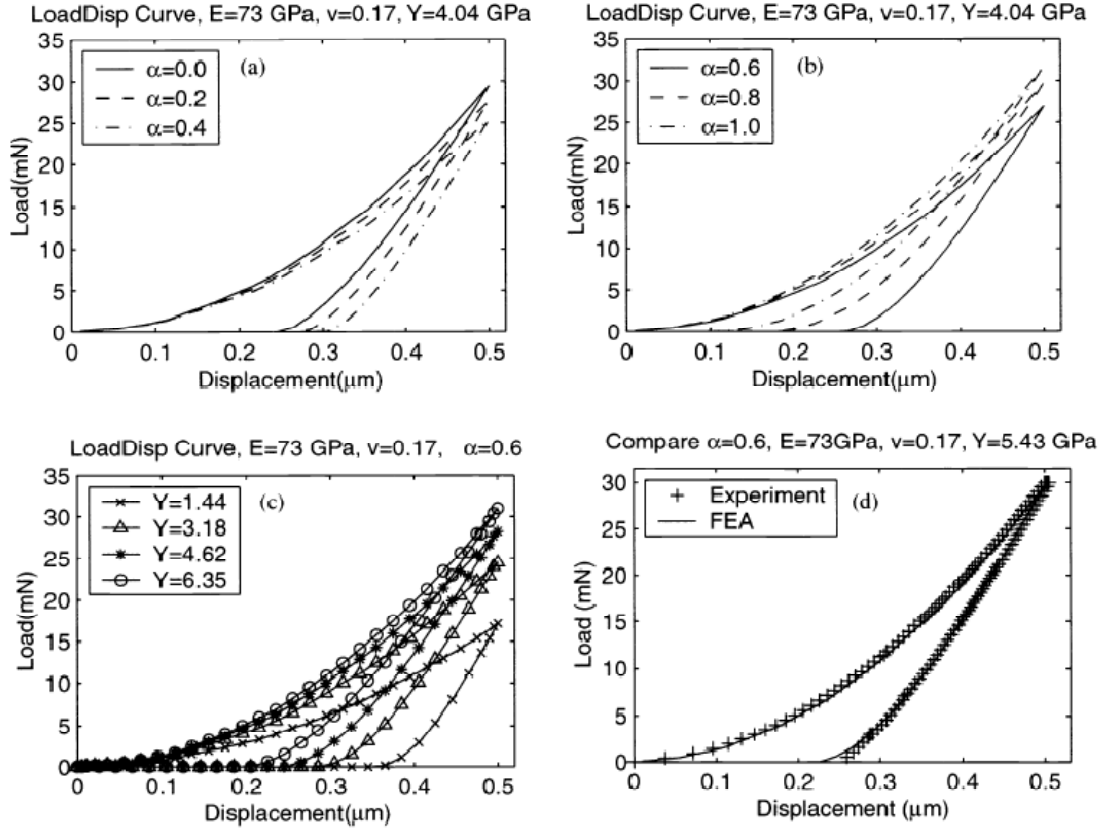


Figure 1.21 Comparing load-displacement curves for different  $\alpha$  and  $Y$ . (a) for small  $\alpha$  at  $Y=4.04$  GPa; (b) for large  $\alpha$  at  $Y=4.04$  GPa; (c) for different  $Y$  at  $\alpha=0.06$ ; (d) fitting to indentation data.[Xin 2000]

and unloading experimental curves well for fused silica and found no pile-up at the edge which agreed with the observations in fused silica experiments as shown in figure 1.21. Furthermore, after introducing the densification parameter, they found that the residual stresses became smaller and the stressed layer became much shallower than the material without densification.

Recently, Kermouche et al. [Kermouche 2008] developed an elliptic yield criterion to establish a new constitutive law to model the plastic deformation of amorphous silica. For negative pressure, they assume a simple von Mises criterion. In

compression ( $p > 0$ ), their proposed yield criterion is  $f(\sigma_{ij}) = \left(\frac{q}{q_c}\right)^2 + \left(\frac{p}{p_c}\right)^2 - 1$

while in tension ( $p < 0$ ), one has  $f(\sigma_{ij}) = q - q_c$  where  $p_c$  and  $q_c$  represent the hydrostatic plastic limit in pure hydro-static state and the shear limit in pure deviatoric state, respectively, as shown in figure 1.22.



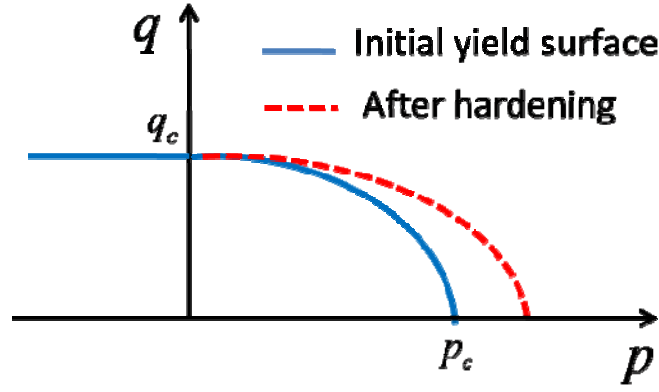


Figure 1.22 Elliptic yield criterion for amorphous silica.  $p$  denotes the pressure,  $p_c$  denotes the threshold of densification pressure,  $q$  denotes the equivalent shear stress in compression ( $\sqrt{3}\tau_e$ ),  $q_c$  denotes the critical threshold of equivalent shear stress [Kermouche 2008].

The model takes into account the densification-induced hardening observed under purely hydrostatic loading with DAC experiments. Based on the reverse analysis with the load-penetration curve of a fused silica glass, they compared their numerical simulations with some indentation results as shown in figure 1.23. They achieved good agreement with the experimental map obtained by Raman microscopy measurements underneath a Vickers indentation [Perriot 2006].

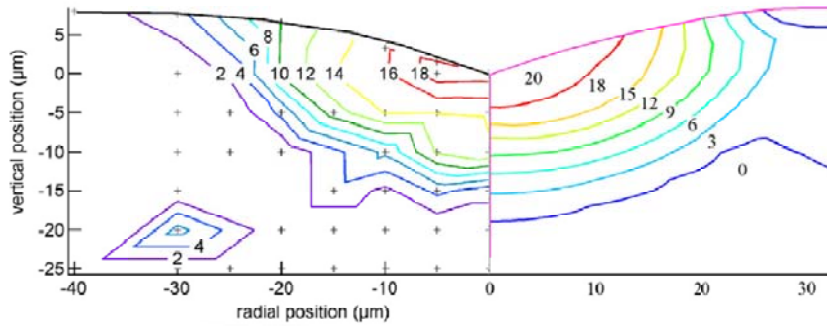


Figure 1.23 Densification map: left, experiment results; right, finite element results [Kermouche 2008].

More recently, Gaerlrab et al.[Gadelrab 2012] using a linear Drucker-Prager model to describe fused silica deformation. Real tip geometry obtained from Atomic Force Microscopy (AFM) is utilized to numerically simulate the area calibration process. Their results indicate a significant discrepancy between the tip area input into their simulation and the one obtained by the calibration process. Unfortunately, their simulation results can not fit the tip metrology obtained by AFM. Therefore, more realistic models are needed to explain the complex deformation process.

In general, what the models have done is shown in Table 1.5.

Table 1.5 Summary of models in densification.

Models	Elasticity	Plasticity	Shear	Densification	Hardening	Densification saturation	Changes in moduli	References
Yasui Imaoka	yes	yes	yes	yes	yes	no	no	Imaoka 1976, Yasui 1982
Giannakopoulos et al.	yes	yes	yes	no	yes	no	no	Giannakopoulos 1997, Zeng 1995
Lambropoulos, Xin et al.	yes	yes	yes	yes	yes	no	no	Lambropoulos 1997, Xin 2000
Kermouche et al.	yes	yes	yes	yes	yes	no	no	Kermouche 2008
Gaerlrah et al.	yes	yes	yes	yes	yes	no	no	Gaerlrah 2012

On the other hand, what is lacking in these models as below:

- i) Saturation of densification,
- ii) Changes in elastic moduli,
- iii) Role of shear on densification,
- iv) Volume conservative plasticity.

## **1. 6 Discussions and prospect**

### **1.6.1 Effect of time and temperature**

The former research results indicate that densification depends on time to some extent. Since fluctuations of temperature and pressure could lead to slight variations in the degree of shear, it is difficult to isolate the effect of time alone. Normally, some seconds duration time in high pressures experiments would reach the permanent densification and no change in Room temperature as long as several years. Meanwhile, annealing the decompression samples several hours would show the densification contribution on the volume change during its deformation, which has been well explored by experiments, such as indentation.

Although, former work shows that temperature will make densification easier at a lower pressure would reach the same percentage as that revealed under room temperature [Mackenzie 1963a, Mackenzie 1963b]. No quantitative measurement of the dependence of the densification rate with temperature is possible as yet. It seems that the activation energies for viscous flow combined with pressure, temperature, time, relaxation are still unexplored.

### **1.6.2 Intermediate-range order interpretation**

The short-range order (SRO) refers to correlations existing between nearest neighbors and is a common feature of most amorphous materials, while intermediate range order (IRO) is defined as the level of structural organization involving distances significantly longer than nearest-neighbor bonds [Bernal 1960, Gaskell 1978, Kotkata 1994]. For silica glass, neutron scattering and Raman scattering studies show that the intermediate-range structure appears as a change in the first and second diffraction peaks which has a linear proportionality to the density [Inamura 1998]. Inamura et al., found that the low-energy dynamics, the Boson peak, had a strong correlation with the changes in intermediate-range structure. According to Mukherjee et al. [Mukherjee 2001], Raman spectroscopy measurements on their retrieved samples quenched from high pressure and high temperature experiments do not show any shifts in Raman peaks indicating a large modification in the IRO in the structure of amorphous silica. It means that six-fold ring structure or equivalently a void structure could be the key structure for the intermediate-range structure of vitreous silica. Besides, Wright, Galeener, et al. [Wright 1992, Galeener 1985], suggested that the shift in Si-O-Si

angle brought about by densification was due to a decrease in the next-nearest neighbor oxygen  $O_{(1)}-O_{(2)}$  distance.

Recently, Sampath et al. [Sampath 2003], studied the intermediate-range order in permanently densified  $\text{GeO}_2$  glass, and argued that densification causes a reduction in the length scale of IRO. The difference structure factors obtained by combining the x-ray and neutron data so as to eliminate one partial structure factor at a time shows the greatest effect when Ge-Ge correlations are eliminated and least when O-O correlations are eliminated. Furthermore, they consider that the reduced length scale results from a decrease in the next-nearest neighbor Ge-O and O-O distance caused by a rotation about the Ge-O-Ge bonds and a distortion of the  $\text{GeO}_4$  tetrahedral, as shown in figure 1.24.

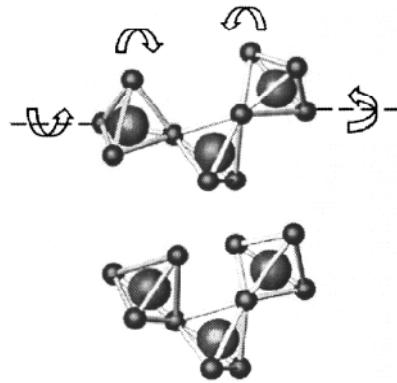


Figure 1.24 Schematic of tetrahedral network of  $\text{GeO}_2$  glass with corner shared  $\text{GeO}_4$  tetrahedral units. The arrows show the bending of the Ge-O-Ge angles and rotation of the tetrahedral used to produce the densified structure [Sampath 2003].

## 1.7 Summary

Since the discovery of the irreversible phenomena in silica glass, a remarkable advances in the densification mechanism of inorganic glasses have been achieved in the last three decades, with the improvement of experimental methods and the development of theoretical analyze. Whether there is a universal law for the densification mechanism to all inorganic glasses and how to interpret the deformation phenomenology that links to the disordered materials are still a great challenge to scientists. Furthermore how to use the deformation properties of glasses to their applications is needed to explore.

In this review, we have retrospected the research work on the densification of inorganic glasses under high pressure and attempted to discover the universal law of densification. One general objective of this review has therefore been encouraged an eclectic and hopefully holistic approach in exploring the physics and mechanics of inorganic glasses.

We highlight 9 important observational principles that emerge from this review:

- (1) Two universal densification phenomena can be summarized as continuous irreversible densification which come into being at the very low pressure and non-continuous irreversible densification which has a threshold of pressure where the irreversible deformation initialized, as shown in figure 1.25.

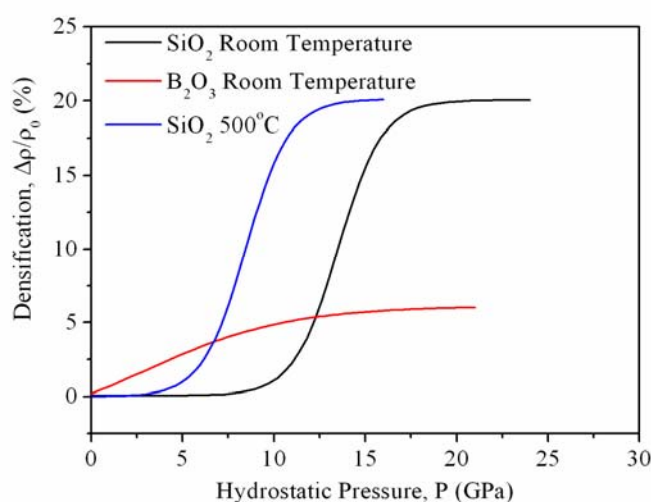


Figure 1.25 Continues and non-continues densification processes.

- (2) Silica glasses are representative research materials which cause a lot of focus on both the experimental and theoretical work. Under very high hydro-static pressure, vitreous silica has a threshold of densification around 8-10 GPa at

room temperature, continuously increasing its density until reaching 20-25 GPa where the saturation of densification process occurs.

- (3) Shear stress plays a great role on the deformation of glasses which mainly controls the induced cracks, but the real role of shear stress and pure pressure separately is still unclear.
- (4) The results of various techniques such as neutron and x-ray diffraction, Brillouin, Raman, and IR spectroscopy, as well as modelling suggest that the densification after compression can be attributed to microscopic structural changes and atomic rearrangements, though the mechanism of the process undergone by amorphous silica is not yet fully understood.
- (5) Temperature has a great impact of the densification, which makes it easier for starting the densification process and lowers the saturation stage pressure, but the saturation of densification is the same, as shown in figure 1.25.
- (6) The investigations demonstrate that both the longitudinal and transverse sound velocities increase and decrease with pressure. They exhibit irreversible behavior on densification.
- (7) Covering a wide interval of values for inorganic glasses, the Poisson's ratio is correlated to the maximum density improvement. The smaller  $\nu$ , the larger densification.
- (8) Based on classic continuum mechanics, models for the densification loading and unloading process have achieved a good agreement with the experimental results. However, their noticeable drawback is forgot the saturation process and the changes in elastic moduli.
- (9) Densification may be due to the reduced length scale of the intermediate range order from a decrease in the next-nearest neighbor R-O and O-O distance caused by a rotation about the R-O-R bonds and a distortion of the RO<sub>4</sub> tetrahedral for SiO<sub>2</sub> or GeO<sub>2</sub>.

## References

- 1) [Antao 2007] S. M. Antao, I. Jackson, B. Li, J. Kung, J. Chen. I. Hassan, R.C. Liebermann, and J. B. Parise, *High-temperature elasticity of magnesioferrite spinel*. Phys. Chem. Miner., **34**, 345 (2007).
- 2) [Antao 2008] S. M. Antao, C. J. Benmore, B. S. Li, L. P. Wang, E. Bychkov, and J. B. Parise. *Network rigidity in GeSe<sub>2</sub> glass at high press.* Phys. Rev. Lett, **100**, 115501 (2008).
- 3) [Arndt 1969] J. Arndt. *Effect of impurities on densification of silica glass*. J. Am. Ceram. Soc., **52**, 285 (1969).
- 4) [Arora 1979] A. Arora, D. B. Marshal, and B. R. Lawn. *Indentation deformation/fracture of normal and anomalous glasses*. J. Non-Cryst. Solids, **31**, 415 (1979).
- 5) [Bastick 1950] R. E. Bastick, J. Soc. Glass Technol., **34**, 69 (1950).
- 6) [Bernal 1960] J. D. Bernal. *Geometry of the structure of monatomic liquids*. Nature, **185**, 68 (1960).
- 7) [Bray 1998] P. J. Bray, and G. L. Petersen, Z. Naturforsch. **53** a, 273 (1998).
- 8) [Bridgman 1953] P. W. Bridgman, and I. Simon. *Effects of very high pressures on glass*. J. Appl. Phys. **24**, 405 (1953).
- 9) [Bridgman 1955] P. W. Bridgman. Proc. Amer. Acad. Arts and Sci., **84**, 112 (1955).
- 10) [Brow 1988] P. K. Brow. *Glass surface modification during ion beam sputtering*. J. Non-Cryst. Solids, **107**, 1 (1988).
- 11) [Cesh 1997] G. Cseh, N. Q. Chinh, P. Tasnádi, P. Szommer, A. Juhász. *Indentation tests for the investigation of the plasticity of glasses*. J. Mater. Sci. **32**, 1733 (1997).
- 12) [Chaboche 1998] J. L. Chaboche, and O. Jung. *Application of a kinematic hardening viscoplasticity with thresholds to the residual stress relaxation*. Int. Journal of Plasticity, **13**, 785 (1998).
- 13) [Chao 2008] W. C. Chao, P. W. Wang, and L. G. Hwa. *Pressure dependence of elastic properties of low-silica calcium alumina-silicate glasses*. J. Non-Cryst. Solids, **354**, 1389 (2008).
- 14) [Christiansen 1962] E. B. Christiansen, S. S. Kistler, and W. B. Gogarty. *Irreversible compressibility of silica glass as a means of determining the distribution of force in high-pressure cells*. J. Amer. Ceram. Soc., **45**, 172 (1962).
- 15) [Cohen 1961] H. M. Cohen, and R. Roy. *Effects of ultrahigh pressure on glass*. J. Amer. Ceram. Soc., **44**, 523 (1961).

- 16) [Cohen 1962] H. M. Cohen, and R. Roy. *Reply to “comments on ‘Effects of ultrahigh pressure on glass’ ”*. J. Am. Ceram. Soc., **45**, 398 (1962).
- 17) [Cohen 1965] H. M. Cohen, and R. Roy. *Densification of glass at very high pressure*. Phys. Chem. Glasses, **6**, 149, 1965.
- 18) [Douglas 1958] R. W. Douglas. *Some Comments on Indentation Tests on Glass*. J. Soc. Glass Technol., **42** [206], 145 (1958).
- 19) [Doye 1996] J. P. K. Doye, and D. J. Wales. *The structure and stability of Atomic Liquids: From clusters to bulk*. Science, **271**, 484 (1996) .
- 20) [Doyoyo 2002] M. Doyoyo. *A theory of the densification-induced fragmentation in glasses and ceramics under dynamic compression*. Int. J. Solids. Structures, **39**, 1833 (2002).
- 21) [Ernsberger 1968] F. M. Ernsberger. *Role of densification in deformation of glasses under point loading*. J. Am. Ceram. Soc., **51**, 545 (1968).
- 22) [Evers 1967] M. Evers. *Plastic deformation of glass with diamond indenters*. Glastechn. Ber., **40** [2], 41 (1967).
- 23) [Fairbairn 2006] E. M. R. Fairbairn, F. L. B. Ribeiro, L. E. Lopes, R. D. Roledo-Filho, and M. M. Silvoso. *Modeling the structural behavior of a dam affected by alkali-silica reaction*. Commun. Numer. Meth. Engng, **22**, 1 (2006).
- 24) [Forest 1999] S. Forest, and P. Pilvin. *Modelling finite deformation of polycrystals using local objective frames*. Z. Angew. Math. Mech., **79**, 199 (1999).
- 25) [Galeener 1985] F. L. Galeener. *A model for the distribution of dihedral angles in SiO<sub>2</sub>-like glasses*. J. Non-Cryst. Solids, **75**, 399 (1985).
- 26) [Gaskell 1978] P. H. Gaskell. *A new structural model for transition metal-metalloid glasses*. Nature, **276**, 484 (1978).
- 27) [Gadelrab 2012] K. R. Gadelrab, F. A. Bonilla, M. Chiesa. *Densification modeling of fused silica under nanoindentation*. J. Non-Cryst. Solids, **358**, 392 (2012).
- 28) [Giannakopoulos 1997] A. E .Giannakopoulos, P. L. Larsson. *Analysis of indentation of pressure-sensitive hard metals and ceramics*. Mech. Mater., **25**, 1 (1997).
- 29) [Greaves 2007] G. N. Greaves, S. Sen. *Inorganic glasses, glass forming liquids and amorphizing solids*. Advances in Physics, **56**: 1, 1-166 (2007).
- 30) [Grimsditch 1984] M. Grimsditch. *Polymorphism in amorphous SiO<sub>2</sub>*. Phys. Rev. Lett. **52**, 2379 (1984).
- 31) [Hagan 1978] J. T. Hagan, and M. V. Swain. *The origin of media and lateral cracks around plastic indents in brittle materials*. J. Phys. D: Appl. Phys., **11**, 2091 (1978).
- 32) [Hagan 1980] J. T. Hagan. *Shear deformation under pyramidal indentations in soda-lime glass*. J. Mater. Sci., **15**, 1417 (1980).
- 33) [Hagan 1979] J. T. Hagan. *Cone cracks around Vickers indentations in fused silica glass*. J. Mater. Sci., **14**, 462 (1979).



- 34) [Hall 1960] H. T. Hall. *Ultra-high pressure, high temperature apparatus: the 'belt.'* Rev. Sci. Instr., **31** [2], 125 (1960).
- 35) [Hannon 1995] A. C. Hannon, A. C. Wright, J. Blackman, and R. Sinclair. *The vibrational modes of vitreous B<sub>2</sub>O<sub>3</sub>: inelastic neutron scattering and modeling studies.* J. Non-Cryst. Solids, **182**, 78 (1995).
- 36) [Hammouda 2003] T. Hammouda. *High-pressure melting of carbonated eclogite and experimental constraints on carbon recycling and storage in the mantle.* Earth Planet Sci. Lett., **214**, 357 (2003).
- 37) [Hemley 1986] R. J. Hemley, H. K. Mao, P. M. Bell, and B. O. Mysen. *Raman spectroscopy of SiO<sub>2</sub> glass at high pressure.* Phys. Rev. Lett., **57**, 747 (1986).
- 38) [Hwa 2005] L. G. Hwa, W. C. Chao. *Velocity of sound and elastic properties of lanthanum gallium-germanate glasses.* Mater. Chem. Phys., **94**, 37 (2005).
- 39) [Imaoka 1976] M. Imaoka, and I. Yasui. *Finite element analysis of indentation on glass.* J. Non-Cryst. Solids, **22**, 315 (1976).
- 40) [Inamura 1998] Y. Inamura, M. Arai, N. Kiramura, S. M. Bennington, and A. C. Hannon. *Intermediate-range structure and low-energy dynamics of densified.* Physica B, **241-243**, 903 (1998).
- 41) [Inamura 2004] Y. Inamura, Y. Katayama, W. Utsumi, and K. I. Funakoshi. *Transformations in the intermediate-range structure of SiO<sub>2</sub> glass under high pressure and temperature.* Phys. Rev. Lett., **93**, 015501 (2004).
- 42) [Jellison 1977] G. E. Jellison, L.W. Panek, P. J. Bray, and G.B.Rouse. *Determinations of structure and bonding in vitreous B<sub>2</sub>O<sub>3</sub> by means of B<sup>10</sup>, B<sup>11</sup>, and O<sup>17</sup> NMR.* J. Chem. Phys., **66**, 802 (1977).
- 43) [Ji 2006] H. Ji, V. Keryvin, T. Rouxel, and T. Hammouda. *Densification of window glass under very high pressure and its relevance to Vickers indentation.* Scripta Mater. **55**, 1159 (2006).
- 44) [Ji 2007] H. Ji. *Mecanique et physique de l'indentation du verre.* Thesis, Devant l'Universite de Rennes 1, No d'ordre: 3686 (2007).
- 45) [Joos 1957] P. Joos. *Microhardness of the Surface of Glass.* Z. Angew. Phys., **9**, 556 (1957).
- 46) [Katayama 2005] Y. Katayama, and Y. Inamura. *Structural studies on liquids and glasses under high pressure and high temperature.* Nuclear Instruments and Methods in Physics Research B, **238**, 154 (2005).
- 47) [Kato 2010] Y. Kato, H. Yamazaki, S. Yoshida, and J. Matsuoka. *Effect of densification on crack under vickers indentation test.* J. Non-Cryst. Solids, **356**, 1768 (2010).
- 48) [Kermouche 2008] G. Kermouche, E. Barthel, D. Vandembroucq, P. Dubujet, Acta Mater., **56** 3222 (2008).
- 49) [Kotkata 1994] M. F. Kotkata, H. T. El-Shair, M. A. Afifi, and M. M. Abdel-Aziz,. *Effect of thallium on the optical properties of amorphous GeSe<sub>2</sub> and GeSe<sub>4</sub> films.*

- J. Phys. D: Appl. Phys., **27**, 623(1994).
- 50) [Lambropoulos 1996] J. C. Lambropoulos, S. Xu, and T. Fang. *Constitutive law for the densification of fused silica, with applications in polishing and microgrinding*. J. Am. Ceram. Soc., **79** [6], 1441 (1996).
  - 51) [Mackenzie 1961] J. D. Mackenzie, and W.F. Claussen. *Crystallization and phase relations of boron trioxide at high pressures*. J. Am. Ceram. Soc., **44**, 79 (1961).
  - 52) [Mackenzie 1963a] J. D. Mackenzie. *High-pressure effects on oxide glasses: I, Densification in rigid state*. J. Amer. Ceram. Soc., **46**, 461 (1963).
  - 53) [Mackenzie 1963b] J. D. Mackenzie. *High-pressure effects on oxide glasses: II, Subsequent heat treatment*. J. Amer. Ceram. Soc., **46**, 470 (1963).
  - 54) [Mackenzie 1963c] J. D. Mackenzie, R. P. Laforce. *High-pressure densification of glass and effect of shear*. Nature, **197**, 480 (1963).
  - 55) [Makishima 1973] A. Makishima, and J. D. Mackenzie. *Direct Calculation of Young's' Modulus of Glass*. J. Non-Cryst. Solids, **12**, 35 (1973).
  - 56) [Marsh 1964] D. M. Marsh. *Plastic Flow and Fracture of Glass*. Proc. Roy. Soc. (London), **282A** [1388], 33-43 (1964).
  - 57) [Meade 1987] C. Meade, and R. Jeanloz. *Frequency-dependent equation of state of fused silica to 10 GPa*. Phys. Rev. B, **35**, 236 (1987).
  - 58) [Meade 1992] C. Meade, R. J. Hemley, and H. K. Mao. *High-pressure x-ray diffraction of SiO<sub>2</sub> glass*. Phys. Rev. Lett., **69**, 1387 (1992).
  - 59) [Meyers 1994] M. A. Meyers. *Dynamic Behavior of Materials* (John Wiley & Sons, New York, 1994).
  - 60) [Miracle 2004] D. B. Miracle. *A structural model for metallic glasses*. Nature Mater., **3**, 697 (2004).
  - 61) [Miyauchi 1999] K. Miyauchi, J. Qiu, M. Shojiya, Y. Kawamoto, and N. Kitamura. *Peculiar high-pressure behavior in permanent densification of fluorozirconate glass*. Mater. Res. Bull. **34**, 1383 (1999).
  - 62) [Mukherjee 2001] G. D. Mukherjee, S. N. Vaidya, and V. Sugandhi. *Direct observation of amorphous apparently first-order phase transition in fused quartz*. Phys. Rev. Lett., **87**, 195501 (2001).
  - 63) [Nadai 1931] A. Nadai, *Plasticity* (McGraw-Hill, New York, 1931).
  - 64) [Neely 1968] J. E. Neely, and J. D. Mackenzie. *Hardness and low-temperature deformation of silica glass*. J. Mater. Sci., **3**, 603-609 (1968).
  - 65) [Perriot 2006] A. Perriot, D. Vandembroucq, and E. Barthel, V. Martinez, L. Grosvalet, C. Martinet, and B. Champagnon. *Raman microspectroscopic characterization of amorphous silica plastic behavior*. J. Am. Ceram. Soc., **89** [2] 596- 601 (2006).
  - 66) [Peter 1964] K. Peter. *Brittle fracture and micro-plasticity of glasses in indentation experiments*. Glastechn. Ber., **37** [7], 333 (1964).
  - 67) [Peter 1970] K. W. Peter. *Densification and flow phenomena of glass in*

- indentation experiments*. J. Non-Cryst. Solids, **5**, 103 (1970).
- 68) [Polian 1986] A. Polian, and M. Grimsditch. *Elastic properties and density of helium up to 20 GPa*. Europhys. Lett., **2**, 849 (1986).
- 69) [Polian 1993] A. Polian, and M. Grimsditch. *Sound velocities and refractive index of densified  $\alpha$ -SiO<sub>2</sub> to 25 GPa*. Phys. Rev. B, **47**, 13979 (1993).
- 70) [Prasad 1993] M. V. N. Prasad, S. Asokan, G. Parthasarathy, S. S. K. Titus, and E. S. R. Gopal, Phys. Chem. Glasses, **34**, 199 (1993).
- 71) [Primak 1975] W. Primak. *The Compacted States of Vitreous Silica* (Gordon and Breach, New York, 1975).
- 72) [Revesz 1972] A. G. Revesz. *Pressure-induced conformational change in vitreous silica*. J. Non-Cryst. Solids, **7**, 77 (1972).
- 73) [Rouxel 2007] T. Rouxel. *Elastic properties and short-to medium-range order in glasses*. J. Am. Ceram. Soc., **90**, 3019 (2007).
- 74) [Rouxel 2008a] T. Rouxel, H. Ji, T. Hammouda, and A. Moréac. *Poisson's ratio and the densification of glass under high pressure*. Phys. Rev. Lett. **100**, 225501 (2008).
- 75) [Rouxel 2008b] T. Rouxel, H. Ji, V. Keryvin, T. Hammouda, and S. Yoshida. *Poisson's ratio and the glass network topology-relevance to high pressure densification and indentation behavior*. Advanced Mater. Res., **39-40**, 137 (2008).
- 76) [Roy 1961] R. Roy, and H. M. Cohen. *Effects of high pressure on glass: a possible piezometer for the 100-kilobar region*. Nature, **190**, 798 (1961).
- 77) [Sampath 2003] S. Sampath, C. J. Benmore, K. M. Lantzky, J. Neuefeind, K. Leinenweber, D. L. Price, and J. L. Yarger. *Intermediate-range order in permanently densified GeO<sub>2</sub> glass*. Phys. Rev. Lett., **90**, 115502 (2003).
- 78) [Sato 2008] T. Sato, and N. Funamori. *Sixfold-coordinated amorphous polymorph of SiO<sub>2</sub> under high pressure*. Phys. Rev. Lett., **101**, 25502 (2008).
- 79) [Sato 2010] T. Sato, and N. Funamori. *High-pressure structural transformation of SiO<sub>2</sub> glass up to 100 GPa*. Phys. Rev. B., **82**, 184102 (2010).
- 80) [Sato 2011] T. Sato, N. Funamori, and T. Yagi. *Helium penetrates into silica glass and reduces its compressibility*. Nature Commun., **2**, 345 (2011).
- 81) [Shimizu 1981] H. Shimizu, E. M. Brody, H. K. Mao, and P. M. Bell. *Brillouin measurements of solid n-H<sub>2</sub> and n-D<sub>2</sub> to 200 kbar at room temperature*. Phys. Rev. Lett., **47**, 128 (1981).
- 82) [Sugiura 1981] H. Sugiura, K. Kondo, A. Sawaoka. *Dynamic response of fused quartz in the permanent densification region*. J. Appl. Phys., **52**, 3375 (1981).
- 83) [Sugiura 1997] H. Sugiura, R. Ikeda, K. Kondo, and T. Yamadaya. *Densified silica glass after shock compression*. J. Appl. Phys. **81** (4), 1651 (1997).
- 84) [Susman 1991] S. Susman, K. J. Volin, D. L. Price, M. Grimsditch, J. P. Rino, R. K. Kalia, P. Vashishta, G. Gwanmesia, Y. Wang, and R. C. Liebermann. *Intermediate-range order in permanently densified vitreous SiO<sub>2</sub>: A*

- neutron-diffraction and molecular-dynamics study*. Phys. Rev. B, **43**, 1194 (1991).
- 85) [Takada 2003] A. Takada, C. R. A. Catlow, and G. D. Price. *Computer synthesis of  $B_2O_3$  polymorphs*. Phys. Chem. Glasses, **44**, 147 (2003).
- 86) [Taylor 1949] E. W. Taylor. Plastic deformation of optical glass. Nature, **163**, 323(1949).
- 87) [Thompson 1978] J. C. Thompson, and K. E. Bailey. *A survey of the elastic properties of some semiconducting glasses under pressure*. J. Non-Cryst. Solids, **27**, 161 (1978).
- 88) [Tse 1992] J. S. Tse, D. D. Klug, and Y. L. Page. *High-pressure densification of amorphous silica*. Phys. Rev. B, **46**, 5933 (1992).
- 89) [Tsuneyuki 1988] S. Tsuneyuki, M. Tsukada, H. Aoki, and Y. Matsui. *First-principle interatomic potential of silica applied to molecular dynamics*. Phys. Rev. Lett., **61**, 869 (1988).
- 90) [Valle 1996] R. G. D. Valle, and E. Venuti. *High-pressure densification of silica glass: A molecular-dynamics simulation*. Phys. Rev. B, **54**, 3809 (1996).
- 91) [Varshneya 1994] A. K. Varshneya. *Fundamentals of Inorganic Glasses* (Academic Press, San Diego, CA, 1994).
- 92) [Vukceovich 1972] M. R. Vukceovich. *A new interpretation of the anomalous properties of vitreous silica*. J. Non-Cryst. Solids, **11**, 25 (1972).
- 93) [Wagner 1967] J. Wagner, and H. Zinko. *Micro-Elastic Behavior During Scratching of Glass and Plexi-Glass*. Glastech. Ber., **40** [2], 44 (1967).
- 94) [Wakabayashi 2011] D. Wakabayashi, N. Funamori, T. Sato, and T. Taniguchi. *Compression behavior of densified  $SiO_2$  glass*. Phys. Rev. B, **84**, 144103 (2011).
- 95) [Walker 1990] D. Walker, M. A. Carpenter, C. M. Hitch. *Some simplifications to multianvil devices for high pressure experiments*. American Mineralogist, **75**, 1020 (1990).
- 96) [Walrafen 1980] G. E. Walrafen, S. R. Samanta, and P. N. Krishnan. *Raman investigation of vitreous and molten boric oxide*. J. Chem. Phys., **72**, 113 (1980).
- 97) [Weir 1962] C. E. Weir, and S. Spinner. *Comments on "Effects of ultrahigh pressure on glass"*. J. Am. Ceram. Soc., **45**, 196 (1962).
- 98) [Wright 1989] A. C. Wright, A. G. Clare, D. I. Grimely, and R. N. Sinclair. *Neutron scattering studies of network glasses*. J. Non-Cryst. Solids, **112**, 33 (1989).
- 99) [Wright 1992] A. C. Wright, B. Bachra, T. M. Brunier, R. N. Sinclair, L. F. Gladden, and R. L. Portsmouth. *A neutron diffraction and MAS-NMR study of the structure of fast neutron irradiated vitreous silica*. J. Non-Cryst. Solids, **150**, 69 (1992).
- 100) [Xin 2000] K. Xin, and J. C. Lambropoulos. *Densification of fused silica: effects on nanoindentation*. Proc. SPIE., **4102**, 112 (2000).
- 101) [Yasui 1982] I. Yasui, and M. Imaoka. *Finite element analysis of indentation*

- on glass (II)*. J. Non-Cryst. Solids, **50**, 219 (1982).
- 102) [Yoffe 1982] E. H. Yoffe. *Elastic stress fields caused by indenting brittle materials*. Philos. Mag. A, **46**, 617 (1982).
- 103) [Yoshida 2005] S. Yoshida, J. C. Sanglebœuf, and T. Rouxel. *Quantitative evaluation of indentation-induced densification in glass*. J. Mater. Res., **20**, 3404 (2005).
- 104) [Youngman 1994] R. E. Youngman, and J. W. Zwanziger. *Multiple boron sites in borate glass detected with dynamic angle spinning nuclear magnetic resonance*. J. Non-Cryst. Solids, **168**, 293 (1994).
- 105) [Zallen 1984] R. Zallen. *Physics of Amorphous Materials* (Wiley, New York, 1984).
- 106) [Zanatta 2010] M. Zanatta, G. Baldi, S. Caponi, A. Fontana, E. Guilioli, M. Krish, C. Masciovecchio, G. Monaco, L. Orsingher, F. Rossi, G. Ruocco, and R. Verbeni. *Elastic properties of permanently densified silica: a Raman, Brillouin light, and x-ray scattering study*. Phys. Rev. B, **81**, 212201 (2010).
- 107) [Zarzycki 1991] J. Zarzycki. *Glasses and Vitreous state* (Cambridge University Press, Cambridge, 1991).
- 108) [Zeng 1995] K. Zeng, A. E. Giannakopoulos, and D. J. Rowcliffe. *Vickers indentations in glass-II. Comparison of finite element analysis and experiments*. Acta Metall. Mater., **43**, 1945 (1995).
- 109) [Zeng 2010] Q. Zeng, Y. Ding, W. L. Mao, W. Yang, S. V. Sinogeikin, J. Shu, H. Mao, and J. Z. Jiang. *Origin of pressure-induced polyamorphism in  $Ce_{75}Al_{25}$  metallic glass*. Phys. Rev. Lett., **104**, 105702 (2010).
- 110) [Zha 1994] C. S. Zha, R. J. hemley, H. K. Mao, T. S. Duffy, and C. Meade. *Acoustic velocities and refractive index of  $SiO_2$  glass to 57.5 GPa by Brillouin scattering*. Phys. Rev. B, **50**, 13105 (1994).



## Chapter 2

### Deformation Model of Silica Glass under Hydrostatic Pressure

Our passions and desires are unruly, but our character subdues these elements into a harmonious whole. Does something similar to this happen in the physical world? Are the elements rebellious, dynamic with individual impulse? And is there a principle in the physical world which dominates them and puts them into an orderly organization?

Rabindranath Tagore



Silica's structure and properties are unclear, but its densification under high pressure has excited scientists' minds. Is there any universal rule to control its deformation behavior? Is the rule rebellious, confused with intricately results? And is there a principle in the physical world which dominates them and indicates them into an orderly formula?

## Contents

<b>2.1</b>	<b>Introduction.....</b>	<b>56</b>
<b>2.2</b>	<b>Hydro pressure experiments.....</b>	<b>56</b>
2.2.1	In-situ hydro-static experiments.....	58
2.2.2	ex-situ hydro-static experiments.....	61
2.2.3	Extracting data from literature sources.....	62
<b>2.3</b>	<b>Models.....</b>	<b>72</b>
2.3.1	Deformation process.....	72
2.3.2	Constitutive equations (small strain).....	73
2.3.2.1	<i>Yield function</i> .....	73
2.3.2.2	<i>Flow rule</i> .....	75
2.3.3	Implementation.....	78
2.3.3.1	<i>Numerical model</i> .....	78
2.3.3.2	<i>Co-rotational framework</i> .....	78
2.3.4	Verification.....	80
<b>2.4</b>	<b>Identification and numerical results.....</b>	<b>84</b>
2.4.1	Numerical tools .....	84
2.4.2	Strategy of identification.....	84
2.4.3	Assumptions and results.....	85
2.4.3.1	<i>Linear assumption and results</i> .....	85
2.4.3.2	<i>Atan(P) function assumption and Results</i> .....	94
2.4.3.3	<i>Avrami equation assumption and Results</i> .....	101
<b>2.5</b>	<b>Conclusion and discussion.....</b>	<b>109</b>
	<b>References.....</b>	<b>115</b>



## 2.1 Introduction

The aim of this chapter is to establish a constitutive equation to portray the nature of densification under high pressure in silica glass, and provide simple and clear explanations about its deformation mechanisms. It is customary to use the term ‘threshold’ to refer to the density where irreversible begins under the applied pressure, and to refer to the body undergoing the deformation of interest as ‘saturate’ where it reaches the maximum permanent density. Such a hydrostatic loading may involve purely elastic, plastic, irreversible, hardening and phase changes behavior. The first part of this chapter deals with the physical achievements on the deformation stages under hydrostatic pressure. The following part starts from basic principles to establish our constitutive equation. Finally, we use a reverse analysis method to identify the parameters of our model and discuss our results.

## 2.2 High pressure experiments

Amorphous silica ( $\text{SiO}_2$ ) densifies permanently under hydrostatic pressure [Bridgman 1953, Meade 1987, Zha 1994, Sato 2008], indentation [Peter 1970, Yoshida 2005], shock loading [Sugiura 1997] or neutron irradiation [Katayama 2005]. Tracing back to the pioneering work of Bridgman and Simon [Bridgman 1953], silica presented a permanent densification behavior by measuring the densities before and after compression, and reached 6-7 percentage increase in density subjected to a pressure of 200 kilobars at room temperature. Following this work, Cohen and Roy [Roy 1961, Cohen 1961] reported a density increase of 7 percent at only 55 kilobars, and pointed out that from 20 to 160 kilobars, densification of silica glass at room temperature was a linear function of pressure by using the refractive index as a probe for densification. Afterwards, Wier and Spinner [Wier 1962], commented on Cohen and Roy’s results and pointed out that there was no simple direct correspondence between refractive index and density. Replying to Wier’s question, Cohen and Roy pointed out the fact that shear played an important role in the kinetics of densification [Cohen 1962]. Mackenzie [Mackenzie 1963a, Mackenzie 1963b], used Diamond anvil cell loading apparatus with different confining media (alumina or silver chloride) to study the role of shear, time and temperature. Interestingly, they found ~16 percent densification, which was much bigger than that obtained by Bridgman and Cohen, for

silica under 80 kilobars pressure at 300°C by using alumina cell. And he concluded that densification resulting from compression of silica glass in the rigid state depends on the external shear inherent to the particular apparatus and technique. Meanwhile, Christiansen et al. [Christiansen 1962], found the force distribution induced discrepancy of densification from the samples' center to its boundaries. Furthermore, Arndt [Arndt 1969], studied the effect of impurities on densification of silica glass and demonstrated that densification of vitreous silica under identical experimental conditions produces different results, depending on the nature and relative concentrations of different kinds of impurities. Therefore, how to get pure high hydrostatic pressure conditions, and how to improve the apparatus and techniques to increase the accuracy of measurements turns out to be the main focus in the following decades.

In the 1980's, Mao-Bell type diamond cells were used in combination with Brillouin- and Raman-scattering physical spectroscopies to measure the static compression of fused silica [Grimsditch 1984]. Grimsditch used Brillouin scattering to show that an irreversible change in the longitudinal sound velocity took place between 10-17 GPa and indicated the existence of a new form of amorphous SiO<sub>2</sub>, which is stable at atmospheric pressure. Grimsditch felt that it deserved the label "amorphous polymorph". Afterward, Meade and Jeanloz [Meade 1987] measured the static compression of fused silica above 10 GPa, and they found that the bulk modulus increased sharply at high hydrostatic pressure (~11 GPa). They inferred that at high pressure the compression mechanisms were similar at equivalent volumes and thus the increase in bulk modulus was due to the transition between relaxed and unrelaxed moduli. Furthermore, Meade et al. used x-ray diffraction to measure the first sharp diffraction peak of SiO<sub>2</sub> glass, and found that the coordination number of Si, initially 4 increases between 8 to 28 GPa and reaching six at 42 GPa [Meade 1992]. Later, Zha et al. measured the acoustic velocities and refractive index of SiO<sub>2</sub> glass up to 57.5 GPa by Brillouin scattering in diamond cells at room temperature. They found that both longitudinal and transverse velocities increased sharply between 12 and 23 GPa, and the bulk velocity followed a trend similar to coesite at higher pressures [Zha 1994]. Recently, Rouxel et al., used octahedral multi-anvil apparatus (OMAA) to carry out more ideal hydro-static pressure experiments [Ji 2007, Rouxel 2008]. They obtained whole samples that not break after decompression for pressures as high as 25 GPa and measured the densities [Ji 2007]. More recently, Sato and Funamori, developed synchrotron x-ray absorption and diffraction techniques to measure the

in-situ behavior of Silica under high pressure up to 100 GPa [Sato 2008, Sato 2010]. They succeeded in measuring the densities up to 50 GPa. Wakabayashi et al., studied the compression behavior of fully densified SiO<sub>2</sub> glass up to 9 GPa at room temperature and clarified that the glass behaved in an elastic manner by optical-microscope observation, x-ray diffraction and Raman scattering measurements [Wakabayashi 2011]. Therefore, the hydrostatic compression apparatus has been improved to provide reliable hydrostatic compression experiments, and Raman, Brillouin light and x-ray diffraction scattering techniques have been developed to obtain accurate density and structure changes under high pressure.

### 2.2.1 In-situ hydrostatic experiments

First of all, for the in-situ hydro-static experiments, three papers came to our attention [Meade 1987; Polian 1993; Zha 1994]. Meade and Jeanloz used optical technique to measure strain in the diamond cell. The samples were compressed in a gasketed Mao-Bell-type diamond cell apparatus (DCA), with a 4:1 methanol-ethanol mixture as the pressure-transmitting medium. Linear strains were measured on three samples at hydrostatic pressures up to 11.6 GPa. They confirmed that at high pressures (around 10 GPa) the long-range disorder in the glass did not fundamentally change the elastic properties of SiO<sub>2</sub> for the tetrahedral structure [Meade 1987]. However, they failed to get information beyond 10 GPa. Afterwards, Polian and Grimditch used Brillouin scattering to investigate the room-temperature densification of hydrostatically compressed fused silica at much higher pressures [Polian 1993]. Irreversible densification was initiated at about 12 GPa and completed at about 20-25 GPa. At very high pressure (up to 40 GPa), they observed no further densification occurred, which manifested the saturation in permanent densification. They studied acoustic wave velocities via Brillouin scattering. Let  $V_L$  and  $V_T$  be the longitudinal and shear wave velocities respectively. They said, there exist a relationship between pressure  $p$  and density  $\rho$  (elastic only):

$$\Delta\rho = \rho(p) - \rho(p_0) = \int_{p_0}^p 1/V_B^2 dp = \int_{p_0}^p (V_L^2 - 4V_T^2/3)^{-1} dp \quad (2.1)$$

However, they found a difference in density between the starting and recovered material for the irreversible change. Then they attempted to use Clausius-Mossotti expression, viz.,

$$(n^2 - 1)/(n^2 + 2) = \text{const} \rho. \quad (2.2)$$

Unfortunately, this equation always predicts an increase in  $n$  as pressure is increased, and there exist contradicts with using equation 2.1. Finally, they gave a rough estimation of the degree of densification which obtained from a determination of the

refractive index is ~22%.

Following, Zha et al. used the Mao-Bell-type Brillouin-scattering diamond cell apparatus (DCA) and measured the longitudinal and transverse velocities and refractive index of SiO<sub>2</sub> up to 57.5 GPa [Zha 1994]. Their results show the sound velocities increase rapidly between 12 and 23 GPa. At higher pressures, the bulk velocity follows a trend similar to that expected for coesite. At 57.5 GPa, the longitudinal velocity of SiO<sub>2</sub> glass is 11.85 ( $\pm 0.51$ ) km/s and the transverse velocity is 6.12 ( $\pm 0.06$ ) km/s. For the decompression from 57.5 GPa, it decrease reversibly to 26 GPa, but displayed an irreversible change when decompressed from 16 GPa to ambient pressure. Therefore, they calculated that a large volume collapse beginning at ~10 GPa, where the pressure induced 4-6 Si-atom coordination change, and reach 19.6% of maximum densification level at 23-26 GPa. Furthermore, they suggested an open question that there were a variety of metastable states available for the amorphous solid at high pressure. However, density measurements of SiO<sub>2</sub> glass were limited to pressure up to about 10 GPa because of experimental difficulties.

The main conclusion from these in-situ experiments may be summarized follows.

- i) There is a threshold for densification pressure around 10 GPa.
- ii) Below this threshold, reversible and elastic changes control the silica deformation behavior under high pressure.
- iii) Beyond this threshold we cannot use the bulk modulus related density function to get the accurate density, but may give some prediction of density by using Clausius-Mossotti expression.
- iv) The maximum densification percent is around 19~22%.
- v) They suggested that silica glass will have amorphous state changes above 26 GPa.

Secondly, as Meade, Polian, Zha et al., did not extract the density of SiO<sub>2</sub> above 10 GPa, Sato and Funamori developed synchrotron x-ray absorption and diffraction techniques to measure the density and structure of Silica at high pressure up to 50 GPa [Sato 2008]. All experiments were conducted with a diamond-anvil cell at room temperature without a pressure transmitting medium. Density measurements were carried out for the sample compressed together with two reference materials (beryllium and aluminum) with a known density by an x-ray absorption method using monochromatic x-rays in Japan. Assuming the thickness of the three materials were the same, densities were determined from the intensities of transmitted x-rays measured for the sample and the reference materials. Structure measurements were carried out by using an x-ray diffraction method with white x-rays, and they discussed the x-ray structure factor  $S(Q)$  and pair distribution function  $g(r)$  which were measured at 50 GPa. They concluded that SiO<sub>2</sub> glass had a six-fold-coordinated

stishovite-like local structure at 50 GPa.

Meanwhile, Benmore et al. investigated the effect of high pressure on the structure of silica glass using high-energy x-ray diffraction up to 43.5 GPa. They pointed that a decrease in the first two peak positions in the real-space pair-distribution functions up to 15 GPa, which indicated an initial shrinkage of the tetrahedral units [Benmore 2010]. Above this threshold pressure the Si-O bond peak shape became asymmetric and the average Si-O bond length and coordination number both increase linearly with pressure.

Considering with the discrepancy from the work of Benmore et al., Sato and Funamori conducted structure measurements of SiO<sub>2</sub> glass under high pressure up to 100 GPa by their energy-dispersive x-ray diffraction method with synchrotron white x rays instead of monochromatic x rays [Sato 2011]. They observed six-fold coordination transform at 27-35 GPa for no significant changes in  $S(Q)$  and  $g(r)$  above 35 GPa, which is a little lower than their former suggestion for 40-45 GPa using monochromatic x rays. They explained that white x rays had relaxed the structure of the samples which caused this inconsistency. Although the discrepancy of the critical six-fold coordination pressure with Benmore et al. and Mead et al. is still unclear, the reason may be due to the hysteresis in the transformation from fourfold- to six-fold- coordination and the difference in stress state during compression and decompression. Furthermore, according to the work of Murakami and Bass who using sound velocity measurements up to 200 GPa, a six-fold-coordination structure may eventually transform to a higher-coordinated structure at above 140 GPa [Murakami 2010].

As a summary to these in-situ experiments' investigations, we can conclude as follows:

- i) There were recently some achievements in obtaining the densities of silica beyond the threshold densification pressure.
- ii) The issue on the effect of transformation kinetics under high pressure is still unsolved, but below 27 GPa there are no phase changes in SiO<sub>2</sub> glass.
- iii) Four-fold coordination structure transform to six-fold coordination structure up to 35-45 GPa.

Interestingly, Wakabayashi et al. studied the compression behavior of fully densified SiO<sub>2</sub> glass up to 9 GPa at room temperature by using a diamond-anvil cell with a mixture of methanol-ethanol as a pressure medium [Wakabayashi 2011]. The fully densified SiO<sub>2</sub> glass was obtained by heating up to 873 K for 10 minutes at 10 GPa, and its zero-pressure density was measured to be  $\rho_0=2.67 \text{ g/cm}^3$  by the Archimedes method (this value corresponds to a 21.3 % increase in density of ordinary one). They observed that there was some remarkable agreement between the volume data on compression and decompression and therefore the glass behaved in an

elastic manner. Furthermore, they determined the zero-pressure bulk modulus to be  $K_0=60.2$  GPa, with its pressure derivative  $K'_0=4$  (fixed), by fitting a second order Birch-Murnaghan equation of state to the volume data. X-ray diffraction and Raman scattering measurements showed that the first sharp diffraction peak (FSDP) and the main Raman band of the glass merge with those of ordinary glass at similar pressure range. Based on these results, they considered that the compaction of interstitial voids dominates in compression mechanism of densified  $\text{SiO}_2$  glass similar to the case of ordinary  $\text{SiO}_2$  glass. Therefore, the occurrence of continuous intermediate states and their elastic behavior may be characteristic of silica before its phase change.

As a summary to the work from Wakabayashi et al. fully densified silica shows an elastic behavior under high pressure before phase change.

### 2.2.2 Ex-situ hydrostatic experiments

Recently, Rouxel et al., used an octahedral multi anvil apparatus (OCDA) to carry out high pressure experiments [Rouxel 2008, Ji 2007]. The high-pressure cell consists of a Cr-doped MgO octahedron which is squeezed between eight converging truncated cubic tungsten carbide anvils. In order to prevent contact between the ceramic parts of the high-pressure assemblies, the starting glass cylinders were raped in 25  $\mu\text{m}$  thick gold foils. It is worthy to point out that unlike previously reported experiments, most specimens came out in one piece, suggesting that the pressure device induced very little shear. Furthermore, the treatment proved to be very homogeneous as illustrated by preliminary micro-Raman scattering investigations along the specimen axis. Density was measured with a better than  $0.001 \text{ g}\cdot\text{cm}^{-3}$  accuracy either by means of density gradient method using two partially miscible liquids (iodobenzene and methylene iodide) or by means of image analysis, using high resolution images of the specimens taken before and after testing. Their experiments show some excellent agreement of densities obtained by the two techniques.

The maximum load pressures for the experiments were 8 GPa, 12 GPa, 20 GPa and 25 GPa, with a densification about 0.5%, 4.1%, 20.0% and 21.6 %, respectively ( $\pm 0.5\%$ ). Furthermore, they confirmed that they observed the saturation densification of silica is about 21% at about 25 GPa. Raman shifts revealed a narrow distribution and a decrease of the Si-O-Si inter tetrahedral angle and a threshold densification pressure at about 8 GPa. Moreover, they used surface acoustic velocity measurements (acoustic microscopy) to obtain the values of elastic properties after decompression, such as bulk modulus, shear modulus and Young's modulus as well as Poisson's ratio. It is important to point out that the bulk modulus will reach values as high as 73.5

GPa after decompression from 25 GPa.

### 2.2.3 Extracting data from literature sources

- In-situ experiments below 8-10 GPa

Below 8-10 GPa, the compression of SiO<sub>2</sub> glass is elastic under hydrostatic stress. We extract the in-situ experiments data from the literatures published by Meade et al. [Meade 1987], Zha et al. [Zha 1994], Sato et al. [Sato 2008, Sato 2011], pressure-density relation as shown in Figure 2.1.

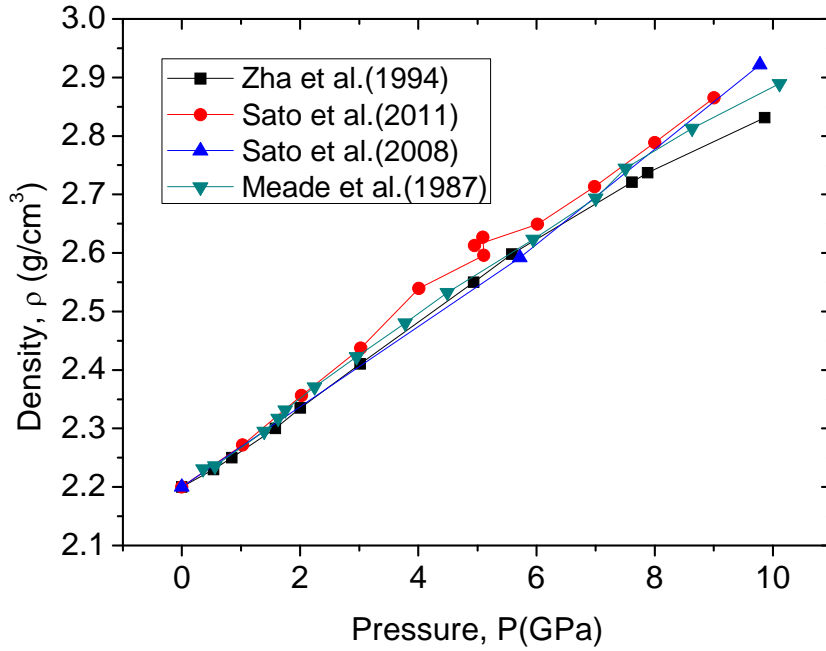


Figure 2.1 Comparison of pressure-density measurements for SiO<sub>2</sub> glass below 10 GPa.

The original density of silica is about 2.20 g/cm<sup>3</sup>, and it will reach 2.85-2.95 g/cm<sup>3</sup> at 10 GPa during the compression process. From figure 2.1, we can find that all density data have a linear increase with pressure. The red circle data [Sato 2011] are a little above the others from 3 GPa. The black square data [Zha 1994] are a little below at the pressure 10 GPa. This discrepancy may come from their different measurements techniques. After all, the elastic relation between pressure and density is clear and credible.

- In-situ experiments up to 55 GPa

We extract the data from Sato's work [Sato 2008, Sato 2011], combine all the data together, as shown in Figure 2.2.



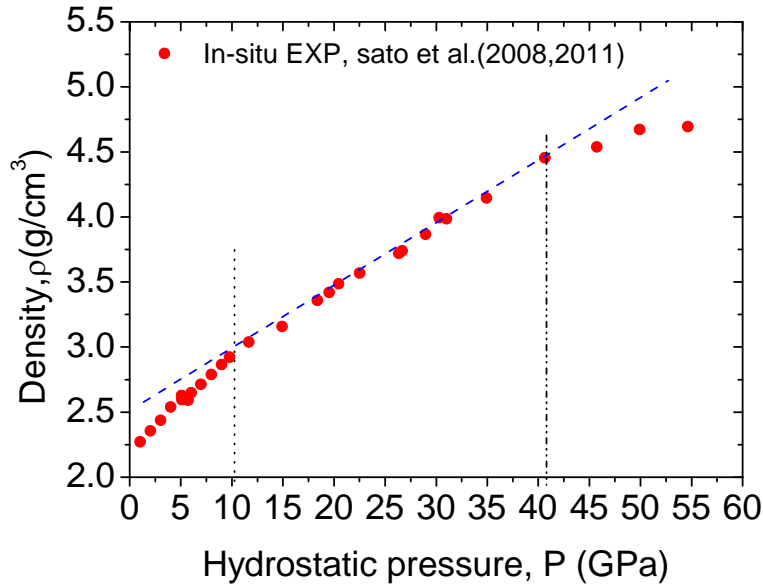


Figure 2.2 In-situ compression experiments of SiO<sub>2</sub> glass:  
Density changes with hydro-static pressure.

In figure 2.2, the original density of SiO<sub>2</sub> is 2.20 g/cm<sup>3</sup>, then it increases greatly and almost linearly from 10 to 40 GPa, and then relatively slower above 40 GPa. Finally it will reach 4.69 g/cm<sup>3</sup> at the pressure of 55 GPa.

In order to get rid of the impact of phase changes, we select the density-pressure data up to 25 GPa (below 27 GPa) from their original data. The data has been listed in table 2.1. These data we need to model are path dependent, so we first need to transfer density-pressure relation to displacement-pressure relation.

In order to derive the deformation-pressure relation from density-pressure relation, we have to choose as the “strain” measure because of the large strains at stake.

### Strain in one dimension [from “ABAQUS Theory Manual”, chapter 1.4.2]

In general, strain measures used in general motions are most simple understood by first considering the concept of strain in one dimension and then generalizing this to arbitrary motions by using polar decomposition theorem just derived. In order to have a measure of deformation—the stretch ratio  $\lambda$ . In fact,  $\lambda$  is itself an adequate measure of “strain” for a number of problems. To see where it is useful and where not, first notice that the unstrained value of  $\lambda$  is 1.0. The basic idea is the strain is zero at  $\lambda=1$ . In one dimension, along some “gauge length”  $dX$ , we define strain as a function of the stretch ratio,  $\lambda$ , of that gauge length:

$$\varepsilon = f(\lambda) \quad (2.3)$$

The objective of introducing the concept of strain is that the function  $f$  is chosen for convenience. To see what this implies, suppose  $\varepsilon$  is explained in a Taylor

series about the unstrained state:

$$\varepsilon = f(1) + (\lambda - 1) \frac{df}{d\lambda} + \frac{1}{2!} (\lambda - 1)^2 \frac{d^2 f}{d\lambda^2} + \dots \quad (2.4)$$

We must have  $f(1) = 0$ , so  $\varepsilon = 0$  at  $\lambda = 1$ . In addition, we choose  $df/d\lambda = 1$  at  $\lambda = 1$ , so that for small strains we have the usual definition of strain as “change in length per unit length.” This ensures that, in one dimension, all strain measures defined in this way will give the same order of approximation when strains are small (because then the higher-order terms in the Taylor series are all negligible)—regardless of the magnitude of any rigid body rotation. Finally, we required that  $df/d\lambda > 0$  for all physical reasonable values of  $\lambda$  (that, is of all  $\lambda > 0$ ) so that strain increases monotonically with stretch; therefore, to each value of stretch corresponds a unique value of strain. The choice of  $df/d\lambda > 0$  is arbitrary: we could equally well choose  $df/d\lambda < 0$ , implying that the strain is positive in compression when  $\lambda < 1$ .

With these reasonable restrictions ( $f = 0$  and  $df/d\lambda = 1$  at  $\lambda = 1$ , and  $df/d\lambda > 0$  for all  $\lambda > 0$ ), many strain measures are possible, and several are commonly used. For instance:

**i) Nominal strain (Biot’s strain):**  $f(\lambda) = \lambda - 1$ .

In a uniformly strained uniaxial specimen, where  $l$  is current and  $l_0$  the original gauge length, this strain is measured as  $l/l_0 - 1$ .

**ii) Logarithmic strain:**  $f(\lambda) = \ln \lambda$ .

This strain measure is commonly used in metal plasticity. One motivation for this choice in this case is that, when “true” stress (force per current area) is plotted against log strain, tension, compression and torsion test results coincide closely. The elastic part of strain can be assumed to be small.

**iii) Green’s strain:**  $f = \frac{1}{2}(\lambda^2 - 1)$ .

This strain measure is convenient computationally for problems involving large motions but small strains, because its generalization to a strain tensor in any

three-dimension motion can be computed directly from the deformation gradient without requiring for principal and their directions.

**Strain in general three-dimensional motions** [from “ABAQUS Theory Manual”, chapter 1.4.2].

Having defined the basic concept of “strain” in one dimension, we now turn to generalize the idea to three dimensions. It is worth remarking that the familiar “small-strain” measure used in most elementary elasticity books,

$$\underline{\varepsilon} = \frac{1}{2} \left( \frac{\partial \underline{u}}{\partial \underline{x}} + \left[ \frac{\partial \underline{u}}{\partial \underline{x}} \right]^T \right) \quad (2.5)$$

is useful only for small displacement gradients—that is, both the strain and the rotations must be small for the strain measure to be appropriate. As we will use corotational framework to solve large strain deformation later, we can use small strain framework (see. Figure 2.9).

The hydrostatic compression test has the following kinematics. For three-dimension deformation case, each point has its Eulerian representation  $\underline{x}$  as below:

$$\underline{x} = \underline{X} + \lambda \begin{bmatrix} 1 \\ 1 \\ 1 \end{bmatrix}_B \quad \underline{X} \quad (2.6)$$

Where  $\underline{x}$  and  $\underline{X}$  denote the initial and final position vectors. For linear

strain:  $\lambda = \frac{l - l_0}{l_0} = \frac{\Delta l}{l_0}$ , when  $\Delta l$  is the difference between  $l$  and  $l_0$ . Simply

in transformation gradient

$$\underline{F} = \frac{\partial \underline{x}}{\partial \underline{X}} = \begin{bmatrix} 1 + \lambda & & \\ & 1 + \lambda & \\ & & 1 + \lambda \end{bmatrix}_B \quad (2.7)$$

Then  $\det |\underline{F}| = (1 + \lambda)^3 = \frac{V}{V_0} = \left( \frac{l}{l_0} \right)^3 = \left( 1 + \frac{\Delta l}{l_0} \right)^3$ . Where  $V_0$  and  $V$  are the original

volume of the object and the transformed volume, respectively. We define  $J = \frac{V}{V_0}$  as

the ratio of deformed to initial volumes equation, known as the Jacobian. We consider the mass conservation during the deformation process,  $\rho V = \rho_0 V_0$ , then we can get:

$$\Delta l = l_0 \exp\left(\frac{\ln J}{3}\right) - 1 \quad (2.8)$$

Thus, we can transfer the density-pressure relation to displacement-pressure relation from  $\Delta l = l_0 \exp\left(\frac{\ln J}{3}\right) - 1 = l_0 \exp\left(\frac{\ln(\rho_0 / \rho)}{3}\right) - 1$ . The transfer data as show in table 2.1.

Table 2.1 In-situ experiments' data [Sato 2008, Sato 2011] and its derivative.

Error of density is about  $\pm 0.05 \text{ g/cm}^3$ .

Pressure P (GPa)	Density $\rho \text{ (g/cm}^3\text{)}$	Relative density ( $\rho/\rho_0$ )	J	Relative density, $\ln J$ (-)	Displace- ment $\Delta l$ (-)	Simulat- ion Time (t)
1.0239	2.2720	1.0327	0.9682	0.0322	-0.0106	0.06588
2.0261	2.3561	1.0709	0.9337	0.0685	-0.022	0.13936
3.0283	2.4372	1.1078	0.9026	0.1024	-0.0335	0.207
4.0087	2.5393	1.1542	0.8663	0.1434	-0.0466	0.2879
5.1089	2.5959	1.1799	0.8474	0.165	-0.0536	0.33099
5.0925	2.627	1.1940	0.8374	0.1773	-0.0574	0.35406
5.7216	2.5921	1.1782	0.8487	0.1640	-0.0532	0.32812
6.013	2.6490	1.2041	0.8304	0.1857	-0.0600	0.37025
6.9825	2.7135	1.2334	0.8107	0.2097	-0.0675	0.41649
8.0010	2.7886	1.2675	0.7889	0.2371	-0.0759	0.46862
9.0032	2.8650	1.3022	0.7678	0.2641	-0.0842	0.51971
9.7809	2.9217	1.3280	0.7529	0.2837	-0.0902	0.55646
11.6559	3.0375	1.3807	0.7242	0.3226	-0.1019	0.62872
14.9226	3.1586	1.4357	0.6965	0.3616	-0.1135	0.70039
18.3827	3.3594	1.5270	0.6548	0.4233	-0.1316	0.81158
19.5230	3.4186	1.5539	0.6435	0.4408	-0.1366	0.8426
20.4703	3.4869	1.5849	0.6309	0.4605	-0.1423	0.8776
22.5193	3.5693	1.6224	0.6163	0.4839	-0.1489	0.9186
26.3466	3.7200	1.6909	0.5914	0.5252	-0.1606	0.9904
26.6752	3.7406	1.7002	0.5881	0.5307	-0.1621	1.000

Then we can get the loading time-pressure relation by use the pressure displacement divide its maximum displacement, shown below.

$$\ln J \rightarrow \Delta l \begin{bmatrix} \Delta l \min = 0 \rightarrow t \\ \downarrow \\ \Delta l \max \rightarrow \end{bmatrix} \Leftrightarrow \begin{bmatrix} 0 \\ t \\ 1 \end{bmatrix}$$

Then we obtain the displacement-pressure and time-pressure data in table 2.1, and we plot these data in figure 2.3.

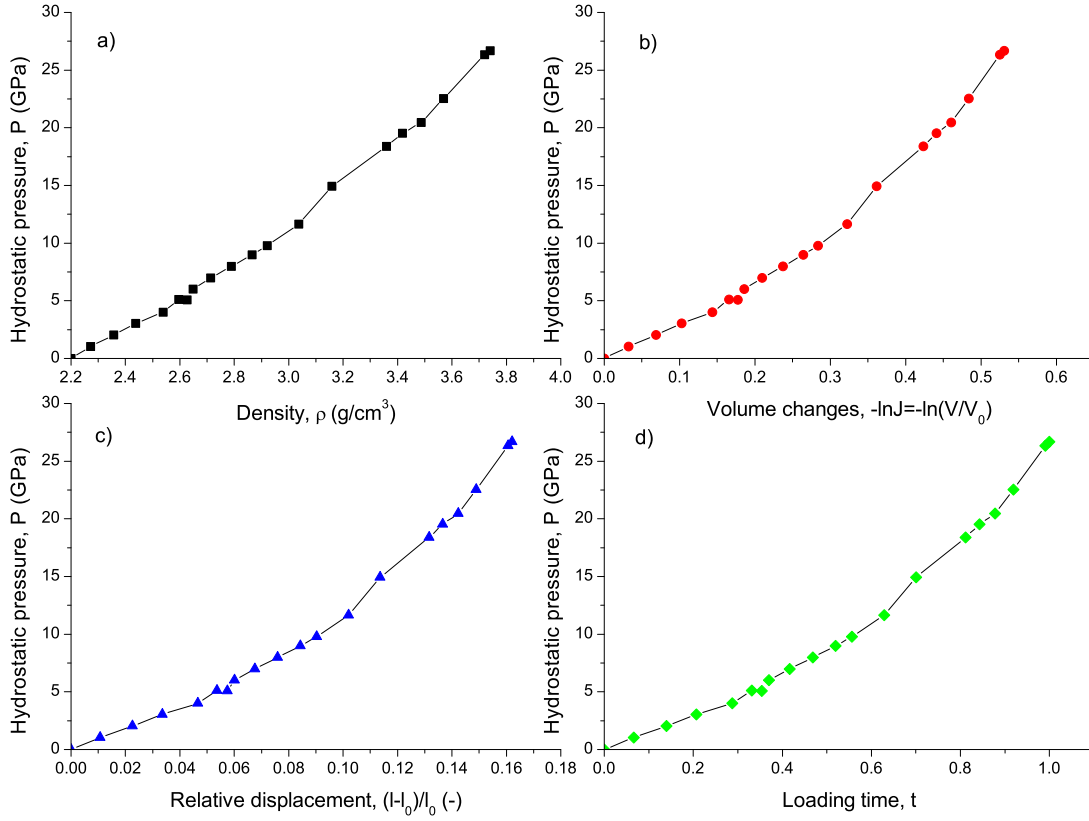


Figure 2.3 Hydrostatic in-situ experiments data: a) pressure vs density [Sato 2008, Sato 2011]; b) pressure vs volume changes; c) pressure vs relative displacement; d) pressure vs loading time.

● In-situ experiment data: fully densified experiment

Wakabayashi et al., studied the compression behavior of densified  $\text{SiO}_2$  glass [Wakabayashi 2011]. The volume changes ( $V/V_0$ ) were determined by measuring the change in size of the sample with optical-microscope images. X-ray diffraction measurements carried out by using an angel-dispersive method with 25 keV monochromatic x rays and an imaging plate detector at BL-18C of Photon Factory (Tsukuba, Japan). The zero-pressure density of the glass was measured as  $\rho_0 = 2.67 \text{ g/cm}^3$  by Archimedes method. Error in their zero-pressure density measurements may be as  $\pm 0.05 \text{ g/cm}^3$ . As the fully densified glass behaves in an

elastic manner, we extract the compression and decompression data from the literature, then combine these data together as shown in table 2.2. Then we use equation 2.8 to derive the relative density of fully densified sample ( $\ln J'$ ) and then transfer it to relative density of pristine  $\text{SiO}_2$  glass ( $\ln J$ ). Then get  $J'$  and  $J$  as shown in table 2.2.

Table 2.2 In-situ experiments' data of fully densified silica [Wakabayashi 2011]. Error of density is about  $\pm 0.05 \text{ g/cm}^3$ . P-- hydrostatic pressure;  $\rho$ --density;  $\ln J$  (-)—Relative density to pristine  $\text{SiO}_2$  glass;  $\ln J'$  (-) Relative density to fully densified  $\text{SiO}_2$ ;  $J$ —Jacobian (pristine  $\text{SiO}_2$  sample);  $J'$ --(fully densified sample).

P (GPa)	$\rho$ ( $\text{g/cm}^3$ )	$-\ln J$ (-)	$-\ln J'$ (-)	$J'$	$J$
0.02367	2.67114	0.19541	0.0000	1.00000	0.8225
0.76547	2.69763	0.20571	0.0103	1.01035	0.81407
1.07323	2.69886	0.20616	0.01075	1.01081	0.8137
1.39678	2.72186	0.21465	0.01924	1.01942	0.80683
1.96496	2.74848	0.22438	0.02897	1.02939	0.79901
2.32008	2.75752	0.22766	0.03225	1.03278	0.79639
2.95139	2.79206	0.24011	0.0447	1.04572	0.78654
3.2197	2.7908	0.23966	0.04425	1.04525	0.78689
4.00095	2.83441	0.25517	0.05976	1.06158	0.77479
4.15878	2.83345	0.25483	0.05942	1.06122	0.77505
4.94792	2.86052	0.26434	0.06893	1.07136	0.76772
5.07418	2.8683	0.26705	0.07164	1.07427	0.76563
5.94223	2.90884	0.28109	0.08568	1.08945	0.75496
6.64457	2.92701	0.28731	0.0919	1.09626	0.75028
6.8971	2.91577	0.28347	0.08806	1.09205	0.75317
7.04703	2.94395	0.29308	0.09767	1.1026	0.74596
7.76515	2.97477	0.3035	0.10809	1.11415	0.73823
8.19129	2.97444	0.30339	0.10798	1.11402	0.73831
8.69634	2.99776	0.3112	0.11579	1.12276	0.73257

In this case, we transfer the relative density from fully densified to pristine sample ones. Then we can take these data as unloading process data which can be used to verify our modeling. Combine these data with Sato's compression data, we can portray an loading and unloading figure as shown in figure 2.4.

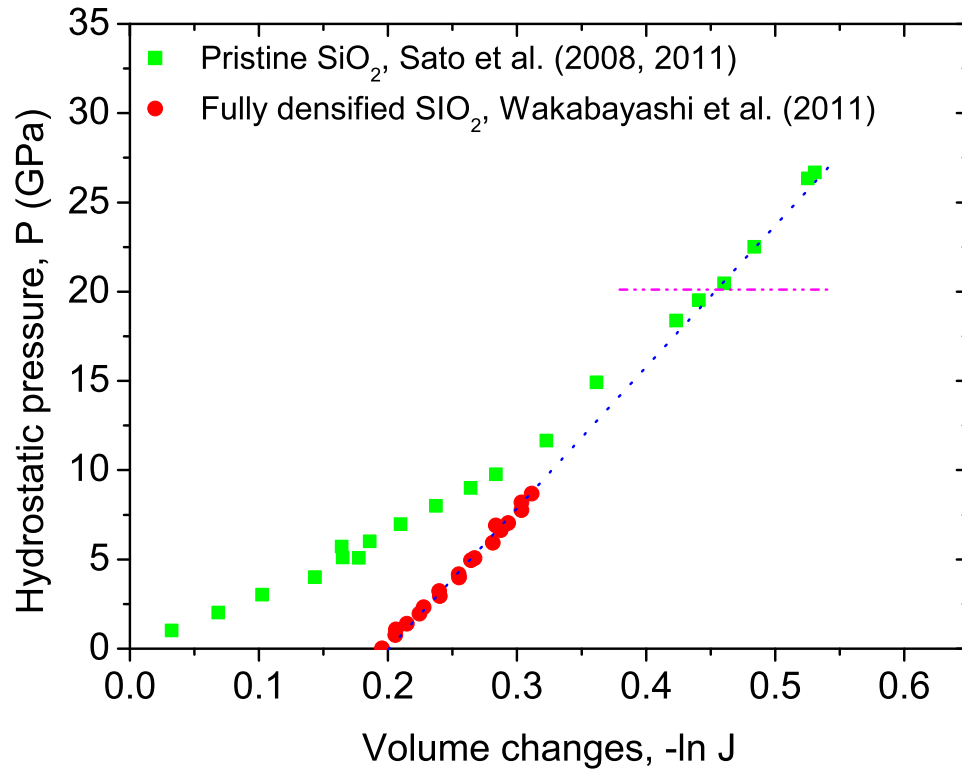


Figure 2.4 In-situ experiments' data: pressure vs relative density. Green square (Pristine sample, Sato et al.); Red point (Fully densified sample, Wakabayashi et al.); Blue dot line (linear fit fully densified data); Pink dash dot line (estimate the start pressure where blue dot line meets Sato's data).

In figure 2.4, it is interesting to point out that the in-situ compression data and decompression data from different experiments turn to be like one continuous loading and unloading experiment. The blue dot line shows the linear tendency of decompression data. The cross point of the pink dash dot line and blue dot line is the pressure when loading and unloading meets. That means the cross point pressure is the saturation pressure around 20 GPa.

● Ex-situ experiments data

Ex-situ experiments data are from Ji's doctorate thesis [Ji, 2007] and Rouxel's published literatures [Rouxel 2008, Rouxel 2010]. It is worth to pointing out that most of their samples are entire bulk after decompression, suggesting that their experiments' pressure device induced little shear. They confirmed that the saturation pressure is about 25 GPa and maximum density change is 21%. The densification error is  $\pm 0.05\%$ . The first black dot vertical line (left) shows where densification begins; the right black dot line shows where the saturation may begin; blue dash line shows the tendency of saturation of densification. Moreover, acoustic velocity tests allow us to extract the elastic properties as shown in table 2.3 and figure 2.6.

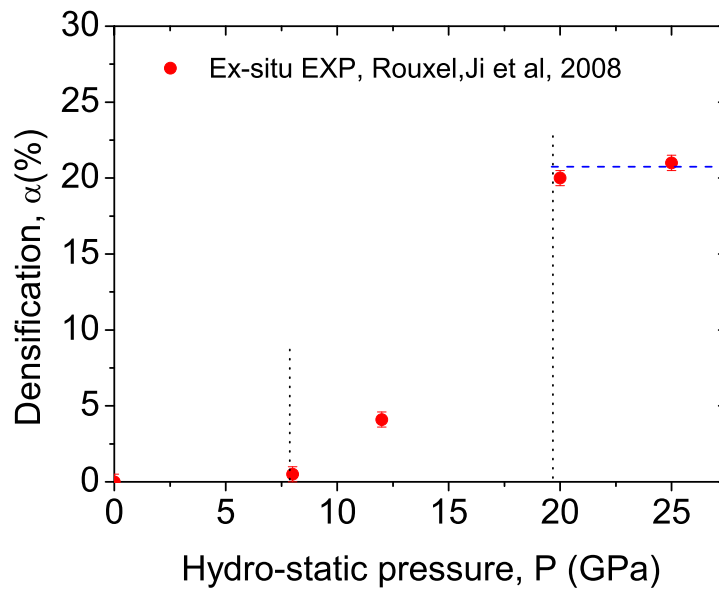


Figure 2.5 Ex-situ experiments: Permanent densification vs hydro-static pressure.

Densification error is  $\pm 0.05\%$ . The first black dot vertical line (left) shows where densification begin; the right black dot line shows where the saturation may begin; blue dash line show the tendency of saturation of densification.

Table 2.3 Ex-situ hydrostatic experiments data [Ji 2007, Rouxel 2008, Rouxel 2010]

Pressure P (GPa)	Density (g/cm <sup>3</sup> )	Densification (%)	$\rho/\rho_0$	$\ln(\rho/\rho_0)=-\ln J$	E (GPa)	$\nu$	B (GPa)	G (GPa)
0	2.20	0	1	0	74.5	0.15	35.48	32.39
8.0	2.211	0.5	1.005	0.005	--	--	--	--
12.0	2.29	4.1	1.041	0.040	75.9	0.149	36.04	33.03
20.0	2.64	20	1.20	0.182	104.5	0.212	60.47	43.11
25.0	2.66	21	1.21	0.191	109	0.252	73.25	43.53

In figure 2.6 we plot the change of modulus ( $M/M_0$ ,  $M$  denotes the elastic modulus at pressure  $P$ , and  $M_0$  denotes the initial elastic modulus.), such as Young's modulus, bulk modulus and shear modulus. From figure 2.6, we can see that before



the pressure of 12 GPa, the modulus almost no increase or increase very slightly. However, after 20 GPa, bulk modulus increase sharply which is very different to the slight increase in Young's modulus and shear modulus.

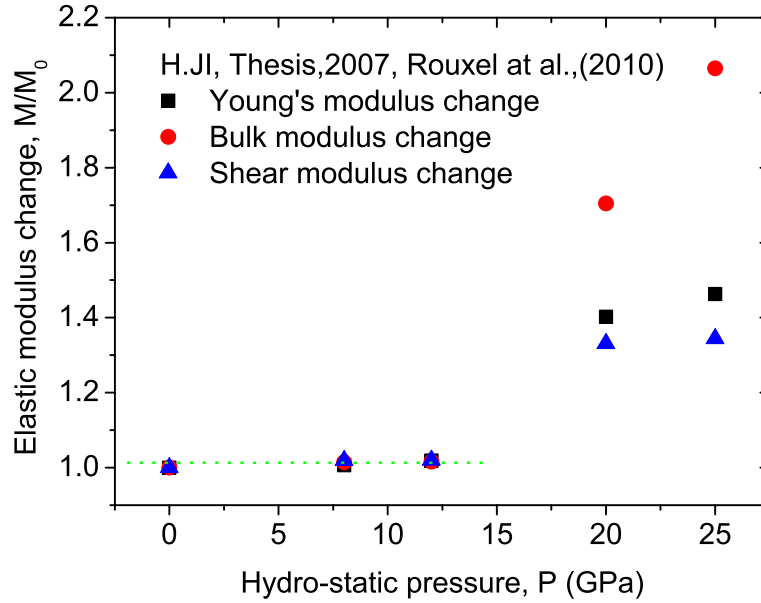


Figure 2.6 Elastic properties change with hydro-static pressure. Black square--Young's modulus; red point--bulk modulus; blue triangle--hear modulus.

In summary, we extracted the in-situ and ex-situ experiments' data carefully, and derive some important information, such as relative density vs pressure. Furthermore, we confirmed the threshold of densification pressure around 8-10 GPa, and the saturation pressure around 20 to 25 GPa, which may help us to establish our model and for further discussion.

## 2.3 Models

### 2.3.1 Deformation process

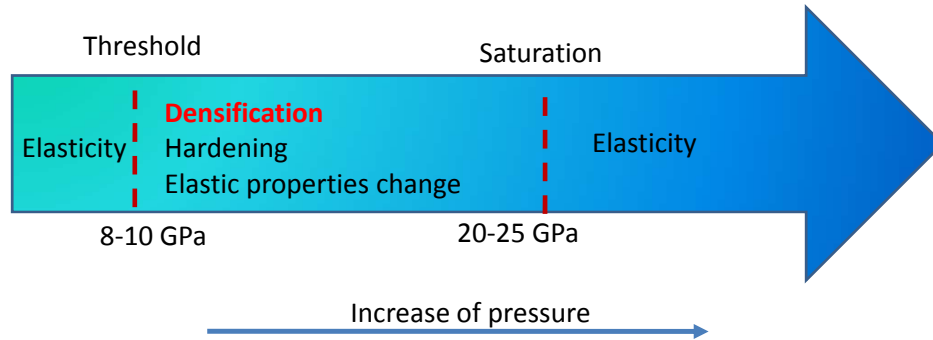


Figure 2.7 Deformation behavior of silica under high pressure.

Based on the reports on silica under hydro-static pressure, especially from the literature of Murakami et al.[Murakami 2010], and Sato et al.[Sato 2008, Sato 2010], their comments and results, we can portray the anomalous deformation behavior of silica under high pressure. We can summarize its deformation process as below:

- (i) For high pressures lower than the threshold densification pressure ( $P_0$ , about 8-10sGPa), silica shows an elastic behavior. In this stage, the main structure of silica is four-fold coordination structure.
- (ii) For pressures higher than  $P_0$ , but lower than the saturation densification pressure ( $P_1$ , about 20-25 GPa), silica shows a densification process combined with hardening and plasticity. In this stage, four-fold coordinated silica, five-fold coordinated silica and six-fold coordinated structures exist together.
- (iii) For pressures higher than  $P_1$ , the densification behavior disappeared and phase changes from four-fold coordination structure to six-fold coordination structure silica become predominate. And about 40-45 GPa, the polymorphism phenomenon ends.
- (iv) According to Murakami's investigation, the stability of six-fold-coordinated Si over a broad pressure interval from ~40-140 GPa. An anomalous increase in the effect of pressure on acoustic velocities at 140 GPa is most likely linked to the onset of structural densification associated with an increase in coordination number six to a higher coordination state, but it's not clear yet.

In order to focus on the role of densification behavior of silica, we select the maximum pressure levels up to 25 GPa where no phase changes are likely to occur.

### 2.3.2 Constitutive equations (small strains assumption)

The traditional plasticity theory, like shear flow theory, cannot describe the plastic behavior of fused silica because the densification is so large that its effect cannot be neglected. Lambropoulos et al., suggested a new constitutive law to describe the evolution of permanent strains after initial densification, and a hardening rule describing the dependence of the incremental densification on the levels of applied stresses [Lambropoulos 1996, Xin 2000]. They use their model to estimate the extent of the densified layer during the mechanical interaction of an abrasive grain and a flat surface under polishing and grinding conditions. Xin and Lambropoulos, incorporate the effects of shear and compression into a new yield function to interpret nanoindentation tests on fused silica via 3D finite element simulation of indentations of Berkovich indenter [Xin 2000]. Furthermore, they use a spherical cavity expansion model to show the densification of silica contributes to lower removal rate and less subsurface damage upon grinding and nanoindentation [Xin 2003]. Recently, Kermouche et al., developed an ellipse criterion to interpret the indentation-induced densification in amorphous silica [Kermouche 2008]. They determined the densification map under the indent compared with experimental indentation-induced densification maps obtained by Perriot et al [Perriot 2006]. Recently, Gaderlraab et al., using a linear Drucker-Prager model to describe fused deformation especially their results show a slight pile up at the face of the tip [Gaderlraab 2012].

However, oddly, there still no constitutive law to interpret the deformation mechanism of amorphous silica under hydrostatic pressure, i.e. without the influence of shear. Moreover, the saturation of densification as well as the changes in elastic modulus has not been considered in the previous models. In order to overcome the limitations due to incomplete and imprecise knowledge, we develop a new constitutive law to interpret the densification induced deformation mechanisms of silica under pure hydro-static pressure.

Densification has a strong dependence on pressure which is the main characteristic of the anomalous deformation behavior [Yasui 1982, Zeng 1995]. In the present case, under pure hydro-static pressure, we assume there were no shear flow, no evidence of frictional effects and ignore the negative hydrostatic pressure effect in tension.

#### 2.3.2.1 Yield function

In the general case, the multi-axial state of stress is described by the stress tensor

$\sigma_{ij}$ . The mean hydrostatic stress  $\sigma_m$  and the equivalent shear stress  $\tau_e$ , are defined as

$$\begin{aligned}\sigma_m &= \frac{1}{3} \sigma_{kk} = \frac{1}{3} (\sigma_{11} + \sigma_{22} + \sigma_{33}) \\ \tau_e &= \sqrt{\frac{s_{ij}s_{ij}}{2}} \quad s_{ij} = \sigma_{ij} - \sigma_m \delta_{ij}\end{aligned}\tag{2.9}$$

where the summation convention is used.  $\delta_{ij}$  is Kronecker's donation for the second order tensor. For pure hydrostatic stress, where  $\sigma_{11} = \sigma_{22} = \sigma_{33} = -p$ , the mean hydrostatic stress  $\sigma_m = -p$  and  $\tau_e = 0$ . For pure shear, where  $\sigma_{12} = \sigma_{21} = \tau$ ,  $\sigma_m = 0$  and  $\tau_e = |\tau|$ . For uniaxial tension  $\sigma_{11} = \sigma$ ,  $\sigma_m = \sigma/3$  and  $\tau_e = \sigma/\sqrt{3}$  [Giannakopoulos 1997, Lambropoulos 1996, Xin 2000].

Here, we assume that during the compression process with pressure  $p$ , without shear and hardening, the deformation process can be divided into two stages: i) elastic stage; and ii) elastic with densification. Then we can deduce the yield function under pure densification condition is

$$f(\sigma_{ij}) = p - p_0\tag{2.10}$$

Where  $\sigma_{ij}$  denotes the Cauchy stress tensor,  $p_0$  denotes the threshold pressure where densification occurs.

Following, we consider the hardening but without shear and saturation of densification, the deformation process can be divided into three stages: i) elastic; ii) elastic, densification and hardening; and iii) elastic, and no densification saturation. Then we can deduce the yield function based on densification with hardening as below (here we use linear hardening assumption):

$$f(\sigma_{ij}) = \begin{cases} p - p_0 & p \leq p_0 \\ p - (p_0 + \xi(p_1 - p_0)) & p_0 < p \leq p_1, \xi \in [0, 1] \\ p - p_1 & p > p_1 \end{cases}$$

Let's combine stage i) and ii), then we can get

$$f(\sigma_{ij}) = \begin{cases} p - (p_0 + \xi(p_1 - p_0)) & p \leq p_1, \xi \in [0, 1] \\ p - p_1 & p > p_1 \end{cases}\tag{2.11}$$

Here, we introduce two parameters,  $p_1$  as the saturation densification pressure and  $\xi$  as the hardening parameter, which will be explained later. Furthermore, we consider the elastic, densification, hardening, and saturation of densification, we can divide the deformation of silica under hydro-static pressure into three stages: i) elastic; ii) elastic, densification and hardening; iii) densification saturation, elastic and hardening. Then we can get the yield function as below

$$f(\sigma_{ij}) = \begin{cases} p - (p_0 + \xi'(p_1 - p_0)) & p \leq p_1, \xi' \in [0,1] \\ p - p_1 & p > p_1 \end{cases} \quad (2.12)$$

Here, the hardening parameter  $\xi'$  is related to the saturation of densification will be explained after.

Finally, considering of the elastic properties change during the deformation process, we introduce some assumption to build the relationship between elastic modulus, such as bulk modulus  $B$ , Young's modulus and shear modulus.

In summary, the deformation model of silica under hydro-static pressure can be illustrated in figure 2.8. There are three zones in figure 2.8, zone I represents pressure below  $p_0$ , only elastic dominate silica's deformation; zone II represents the main densification process in company with hardening, densification; zone III show the pressure higher than saturation pressure  $p_1$ , densification saturation together with elastic properties changes. The blue line is the yield surface where pressure equal to  $p_0$ , densification happens. The green line is the yield surface where densification saturation with pressure  $p_1$ . In all, this framework portrays the densification mechanism of amorphous under pure hydro static pressure.

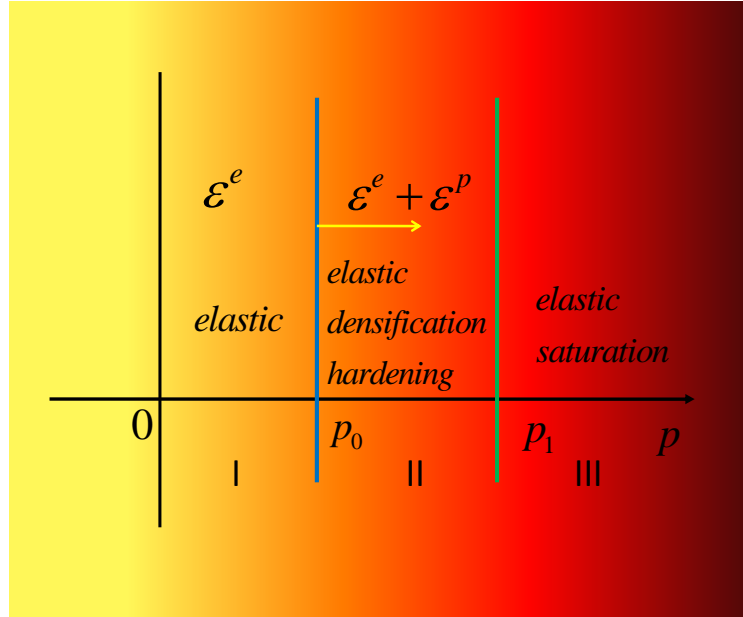


Figure 2.8 Illustration of pure hydro-static pressure deformation model.

### 2.3.2.2 Flow rule (associativity)

The yield function describes the yield surface in stress space. The normal to the yield surface ( $f=0$ ) can be expressed as

$$\mu_{ij} = \frac{\partial f}{\partial \sigma_{ij}} = \frac{\partial f}{\partial p} \cdot \frac{\partial p}{\partial \sigma_{ij}} + \frac{\partial f}{\partial \tau} \cdot \frac{\partial \tau}{\partial \sigma_{ij}} \quad (2.13)$$

Where when the inner product  $\mu_{ij}d\sigma_{ij} > 0$ , the small change of stress tensor  $d\sigma_{ij}$  causes further loading. When  $\mu_{ij}d\sigma_{ij} < 0$ , the material is under unloading conditions. The permanent strains  $\varepsilon_{ij}^p$  evolve as

$$d\varepsilon_{ij}^p = \begin{cases} 0, & \text{if } \mu_{ij}d\sigma_{ij} \leq 0 \\ \neq 0, & \text{if } \mu_{ij}d\sigma_{ij} > 0 \end{cases} \quad (2.14)$$

When the pressures below  $p_0$  ( $p \leq p_0$ ), the yield function is  $f(\sigma) = p - p_0$ .

Especially when the pressure reach  $p_0$  ( $p = p_0$ ), the yield function turns to be zero ( $f(\sigma) = 0$ ), where densification and hardening occurs (blue line in figure 2.8).

If the pressure between  $p_0$  and  $p_1$ ,  $p_0 < p < p_1$ , the yield function is  $f(\sigma_{ij}) = p - (p_0 + \xi(p_1 - p_0))$ . This yield function denotes the zone II in figure 2.8. In this state, we need to introduce two parameter:  $\xi$  and  $\gamma$ . We define  $\xi = \frac{-tr(\varepsilon^p)}{\gamma}$  as the hardening parameter, and  $\gamma = -tr(\varepsilon_{saturation}^p)$  as the saturation state's plastic volume change.  $\gamma$  is the maximum value of densification. when there is no densification,  $\xi = 0$ , if the densification saturates  $\xi = 1$ , then we can get the variable zone of  $\xi \in [0, 1]$ .

For pure pressure and no shear condition:  $\frac{\partial f}{\partial p} = 1$ ;  $\frac{\partial f}{\partial \tau} = 0$ ;  $\frac{\partial p}{\partial \sigma} = -\frac{1}{3}\delta_{ij}$ ;  $\frac{\partial \tau}{\partial \sigma} = 0$ .

Now let's consider the volume change and densification process under pressure,

$$\frac{\Delta V}{V} = tr \varepsilon = tr(\varepsilon^e + \varepsilon^p) = tr \varepsilon^e + tr \varepsilon^p \quad (2.15)$$

Where  $tr \varepsilon^e$  denotes the reversible volume change, and  $tr \varepsilon^p$  denotes the densification induced irreversible volume change, which related to the permanent densification. The superscript  $e$  and  $p$  are used to denote the elastic and plastic part respectively in the following text.

- i) As we know, in zone I only elastic strain, that means  $\dot{\varepsilon}^p = 0$ , extend it as  $\dot{\varepsilon}_{ij}^p = 0$  and densification  $\alpha = 0$ .

For the second stage, zone II, elasticity, densification and hardening all exist. The yield function as  $f(\sigma_{ij}) = p - (p_0 + \xi(p - p_0))$   $p_0 < p \leq p_1, \xi \in [0, 1]$ . In associated plasticity the plastic rate of deformation is normal to the yield surface [Hill 1950].  $\dot{\varepsilon}_{ij}^p = \dot{\lambda} \frac{\partial f}{\partial \sigma_{ij}}$ , where  $\dot{\lambda}$  is the plastic multiplier which can be determined from the consistency condition [Lemaitre 1996]. According to classical phenomenological visco-plasticity models for small strains, we define the kinematic viscosity of the material parameter  $\dot{\lambda} = \left(\frac{f}{k}\right)^n$ . Where  $f$  denotes the load function,  $n$  is a fitting parameter based on Norton-Hoff model. Here,  $n$  and  $k$  are chosen to give a rate-independent response.

Then we can get  $\dot{\varepsilon}^p = \dot{\lambda} \frac{\partial f}{\partial \sigma} = \dot{\lambda} \cdot \left( \frac{\partial f}{\partial p} \frac{\partial p}{\partial \sigma} + \frac{\partial f}{\partial \tau} \frac{\partial \tau}{\partial \sigma} \right) = -\dot{\lambda} \cdot \frac{i}{3}$ . Then we introduce a densification factor  $\alpha$ , here  $\dot{\alpha} = -tr \dot{\varepsilon}^p = \dot{\lambda} \cdot tr\left(\frac{1}{3}\right)i = \dot{\lambda}$ .

ii) When pressure higher than  $p_1$ ,  $p > p_1$ , in zone III in figure 2.8, we can simplify the constitution model to be

$$f(\sigma) = p - p_0 \quad p > p_1,$$

In this stage, we consider it as a new multiply state where elastic turn to a second state, densification saturated, and densification induced hardening finished. Then we can get

$$\frac{\partial f}{\partial p} = 1; \frac{\partial f}{\partial \tau} = 0, \frac{\partial p}{\partial \sigma_{ij}} = -\frac{1}{3}i; \frac{\partial \tau}{\partial \sigma_{ij}} = 0 \text{ and then get}$$

$$\dot{\varepsilon}^p = \dot{\lambda} \frac{\partial f}{\partial \sigma} = \dot{\lambda} \cdot \left( \frac{\partial f}{\partial p} \frac{\partial p}{\partial \sigma} + \frac{\partial f}{\partial \tau} \frac{\partial \tau}{\partial \sigma} \right) = -\dot{\lambda} \cdot \frac{i}{3} \text{ and } \dot{\alpha} = -tr \dot{\varepsilon}^p = \dot{\lambda} \cdot tr\left(\frac{1}{3}\right)i = \dot{\lambda}.$$

Moreover, in this stage, there were no plastic, so  $\dot{\lambda} = 0$ . Then we can get simply results as:

$$\begin{aligned} \dot{\varepsilon}_{ij}^p &= 0 \\ \dot{\alpha} &= -tr \dot{\varepsilon}^p = -tr \dot{\varepsilon}_{saturation}^p = \gamma \end{aligned}$$

In summary, this part we use a linear hardening rule to introduction our constitutive equation and how to deduce the stress-strain relation which relate to densification. This method also can be used to other hardening rules, such as atan function and Avrami function hardening rules, which will be discussed later.

### 2.3.3 Implementation

#### 2.3.3.1 Numerical model

Since we established the constitutive equation, we need to develop a numerical model to solve this problem. Newton's iteration method is used for numerical integration. In general the yield stress is a function of permanent deformation history. According to Hooke's law, writing in tensor form we have

$$d\sigma_{ij} = D_{ijkl} d\varepsilon_{kl}^e \quad (2.16)$$

Where the fourth-order tensor  $D_{ijkl}$  is the material's elastic stiffness tensor. The elastic behavior is assumed to be linear and isotropic.

By coding the numerical model to the subroutine UMAT provided by ABAQUS, we have the ability to study this material by using the finite element method.

#### 2.3.3.2 Co-rotational framework

The experimental data of maximum densification, as well as the molecular dynamics simulations, are in essential as large as 21%, that means the permanent volume change ( $\Delta V$ ) will as high as ~19.3% compared to its original volume ( $V_0$ ). The material's deformation turns to be large in a deformation state. An approach to the solution of this problem is presented under the assumption that the sampling can be made prior to the execution of the simulation under co-rotation framework. In figure 2.9,  $\Omega_0$  denotes the initial configuration of a physical body.  $\Omega_t$  denotes the deformed state of a physical body.  $\Omega_c$  denotes the corotational frame of a physical body. The mapping function from  $\Omega_0$  to  $\Omega_t$  is  $\underline{x} = \chi(\underline{X})$  and the deformation

gradient function is  $\underline{\tilde{F}} = \frac{\partial \underline{x}}{\partial \underline{X}}$ . In a rectangular Cartesian coordinate, the components

of the deformation gradient tensor are  $F_{ij} = \frac{\partial x_i}{\partial X_j}$ . In matrix form,

$$[\underline{\tilde{F}}] = \begin{bmatrix} \frac{\partial x_1}{\partial X_1} & \frac{\partial x_1}{\partial X_2} & \frac{\partial x_1}{\partial X_3} \\ \frac{\partial x_2}{\partial X_1} & \frac{\partial x_2}{\partial X_2} & \frac{\partial x_2}{\partial X_3} \\ \frac{\partial x_3}{\partial X_1} & \frac{\partial x_3}{\partial X_2} & \frac{\partial x_3}{\partial X_3} \end{bmatrix}. \text{ The rotation matrix } \underline{\tilde{Q}}, \text{ between } \Omega_0 \text{ and } \Omega_c \text{ is defined as}$$



$$\dot{\tilde{Q}} \cdot \tilde{Q}^T = 0.$$

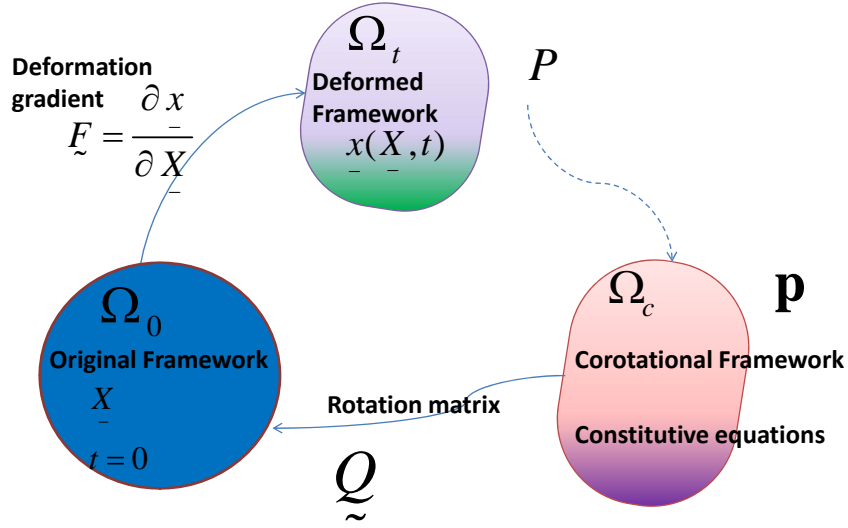


Figure 2.9 A sketch of co-rotation frame.

Volume strain: in this section on the deformation gradient, the ratio of deformed to initial volumes equals the Jacobian  $J = \frac{V}{V_0}$ . As we know, the mass of physical body is an conservation value  $m = \rho_0 V_0 = \rho V$ , then we can obtain the Jacobian in a density form  $J = \frac{\rho_0}{\rho}$ .

The use of local objective frames, has proved to be an efficient method to develop constitutive models at finite strain, which automatically fulfill the material frame indifference requirement [Forest 1994]. Local objective frames can be used to extend, in a straightforward manner, constitutive equations that have been developed at small strains, to be finite strain framework. The choice of the local objective reference frame in which the constitutive equations are written, then becomes a major issue in the modeling [Forest 1999]. In our Lab LIMATB, there is a software SiDoLo developed by Prof. Pilvin et al., can be used to write constitutive equation at small strain in corotational frame and then evaluate the stress in deformational framework. Basing on this software with ABAQUS UMAT, we have the ability to simulate large deformation case by using mass infinity small deformation cases. This is summarized in the following steps: i) coding constitutive law in corotational framework; ii) using rotation matrix to get original framework data by SiDoLo; (iii) using finite element software ABAQUS simulate the deformation process; iv) using SiDoLo to get the corotational data from deformation framework results; v) circulation.

### 2.3.4 Verification

The material model was tested extensively before used to solve more complex problems. In this verification, three simple cases are studied: pure tension, pure shear and pure compression. The finite element model is a simple 8-node 3D solid element. The material properties were chosen as: initial bulk modulus  $B=35.5$  GPa, initial shear modulus  $G=31.9$  GPa. Densification and hardening are considered, and no amorphous state change in the deformation process.

- **Pure tension case**

For the first pure tension case, we impose the tension  $\sigma_{33} = \sigma$  and keep the transverse surface free of stress, so  $\sigma_{11} = \sigma_{22} = 0$ .

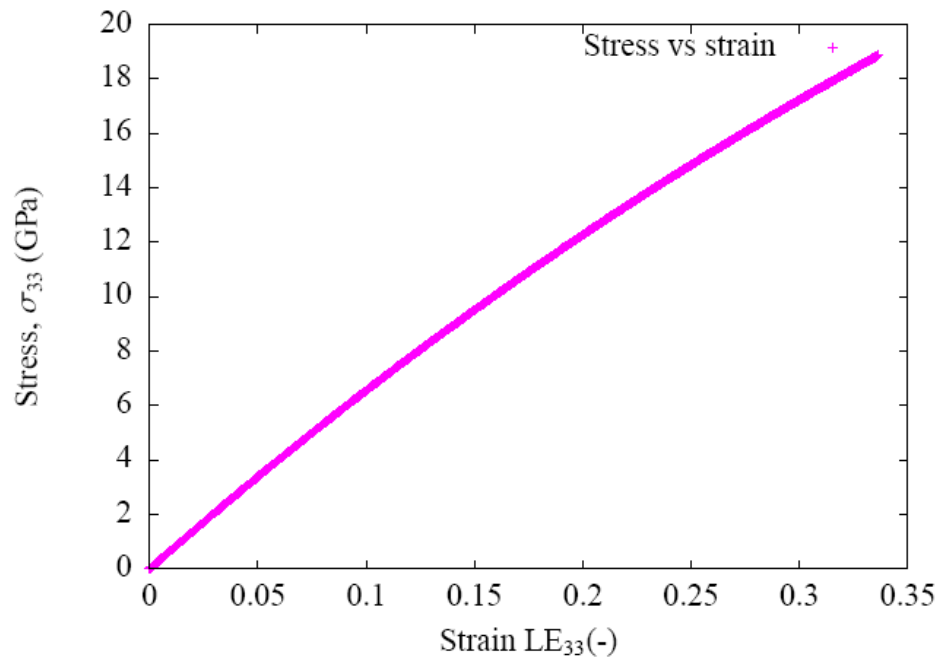


Figure 2.10 Simple tension test: stress vs strain.

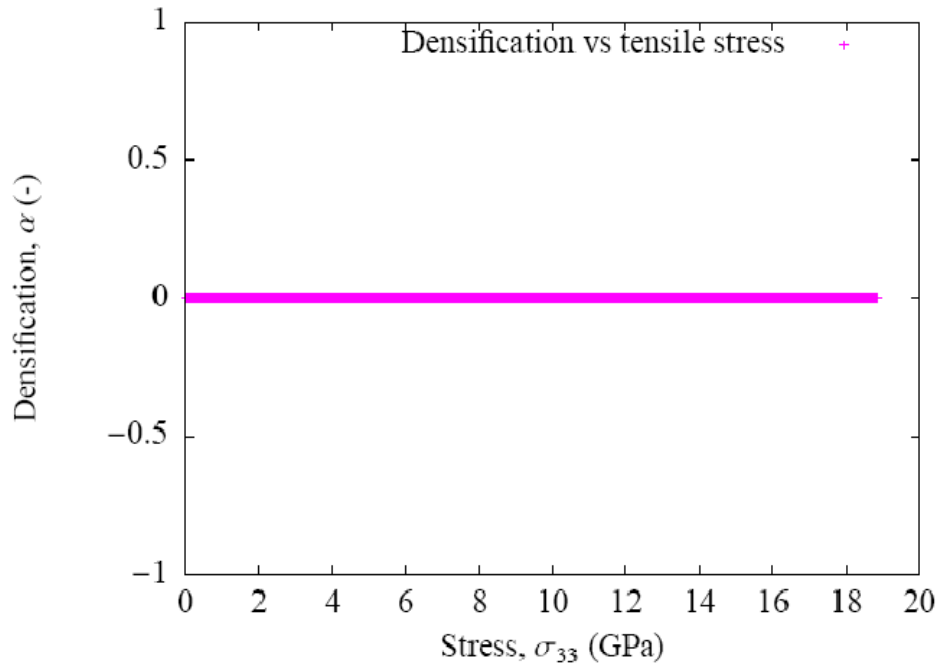


Figure 2.11 Simple tension test: densification vs tensile stress.

The finite element results are plotted in figure 2.10 and figure 2.11, the yield stress almost line increase with strain and densification keep the value of 0. For von Mises yield theory the densification  $\alpha = 0$ . Therefore, analytic and numerical results agree exactly.

### ● Pure shear case

For the second pure shear case, we impose the shear  $\sigma_{13} = \sigma$ .

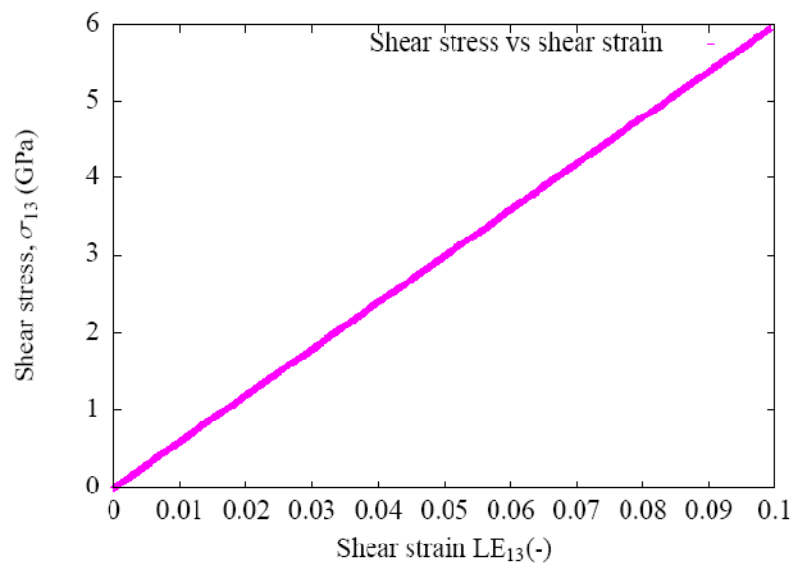


Figure 2.12 Simple shear test: stress vs strain.

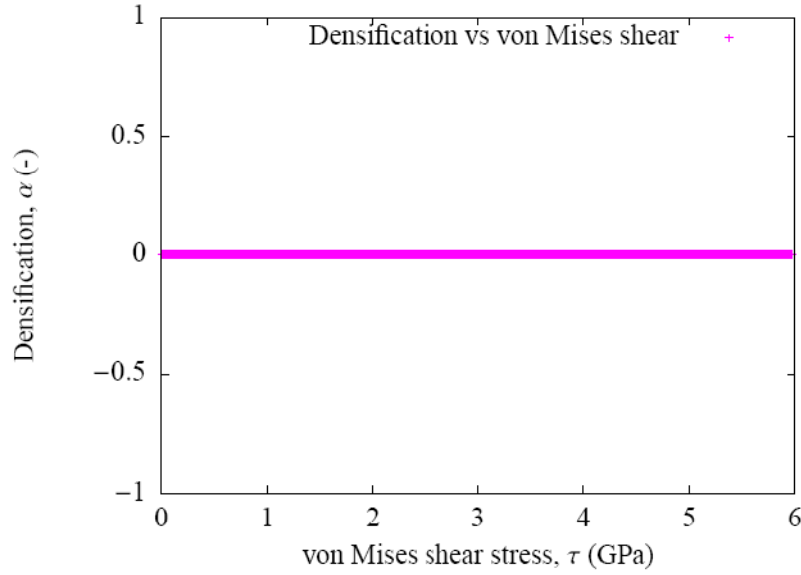


Figure 2.13 Simple shear test: densification vs von Mises shear stress.

The finite element results are plotted in figure 2.12 and figure 2.13, the shear stress line increase with strain and densification keep the value of 0. Therefore, analytic and numerical results agree exactly.

### ● Pure compression case

For the third pure compression case, we impose the compression  $\sigma_{33} = \sigma$  and keep the transverse surface free of stress, so  $\sigma_{11} = \sigma_{22} = 0$ .

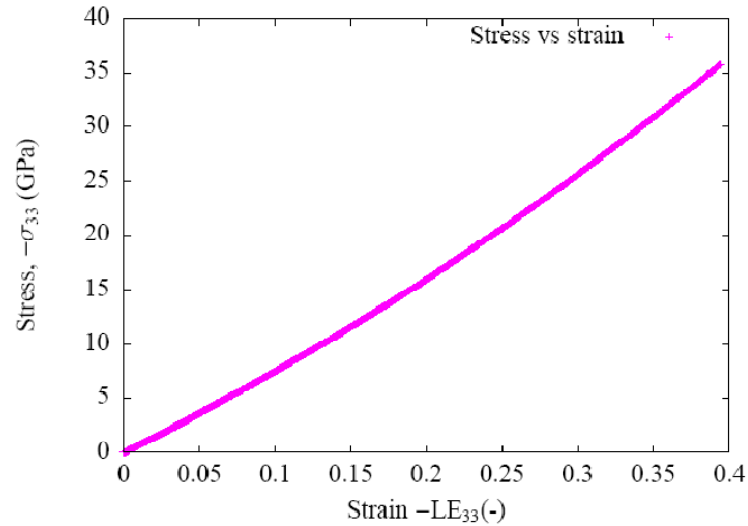


Figure 2.14 Simple compression test: stress vs strain.

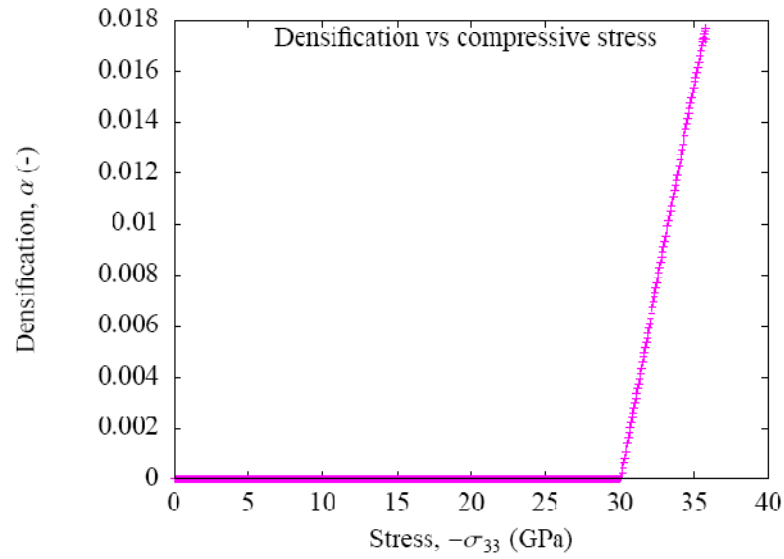


Figure 2.15 Simple compression test: densification vs compressive stress.

The finite element results are plotted in figure 2.14 and figure 2.15, the shear stress line increase with strain. Interestingly, it shows that densification increase when the hydrostatic pressure beyond its densification critical pressure. Therefore, analytic and numerical results agree exactly.

## 2.4 Identification and numerical results

### 2.4.1 Numerical tools

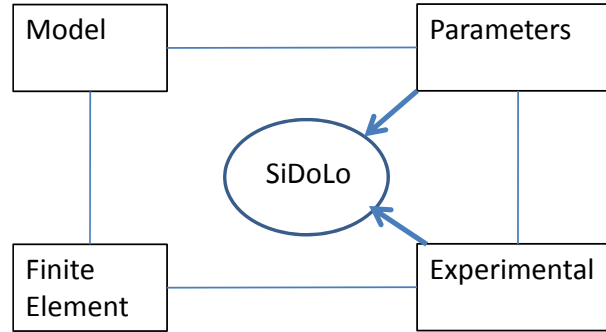


Figure 2.16 The sketch of identification process.

An approach to the solution of this problem is using SiDoLo to verify the numerical results and the experimental data. The sketch of this identification process as shown in figure 2.16. We program our model by ABAQUS UMAT, submit the job to execute finite element simulation. After the first circulation we obtained the numerical results. We extract the data from ABAQUS odb file by using the software Python. Then we use SiDoLo to compare with the original parameters as given in a Coe file [material parameters' file in SiDoLo] and experimental data. After calculating the residuals (minimization function) by SiDoLo, it will produce new parameters to minimize the discrepancy between experimental and simulated curves, which will be used in the next circulation. Many attempts will be operated until reaching the best fitting results from finite element results and experimental data.

### 2.4.2 Strategy of identification

First of all, we have to determine the parameters. In our models, we mainly consider the invariable parameters as the initial bulk modulus  $B_0$  and the initial shear modulus  $G_0$ , these two parameters are given from the experiment data of Ji. The variable parameters such the densification factor, the threshold of pressure  $P_0$ , the saturated pressure for densification  $P_1$ , the maximum of bulk modulus  $B_{\max}$  and the maximum of shear modulus  $G_{\max}$ , these 4 parameter we need to determine with experimental results. Secondly, we give the parameters a range of its values in order to make sure of the physical meaning of the parameters. Thirdly, we start from the simplest model only to consider densification, then consider the saturation of densification, after that we consider the changing in moduli. Using this way, we can step by step to fix the data and realize our identification. Finally, we fix the parameters of  $B_0$ ,  $G_0$ ,  $B_{\max}$ ,  $G_{\max}$ , and the maximum of densification  $\gamma$  (21.6% in

deformed framework, and 19.3% in corotational framework) to get the proper data of  $P_0$  and  $P_1$ .

### 2.4.3 Assumptions and results

#### 2.4.3.1 Linear assumption and results

Here, we assume the densification process to follow a linear change with pressure as shown as in figure 2.17. That means the densification induced hardening follow the relationship of a linear way between hydrostatic pressure and densification:

$$f(\sigma_{ij}) = p - (p_0 + \xi(p_1 - p_0)) \quad p_0 < p \leq p_1, \xi \in [0,1].$$

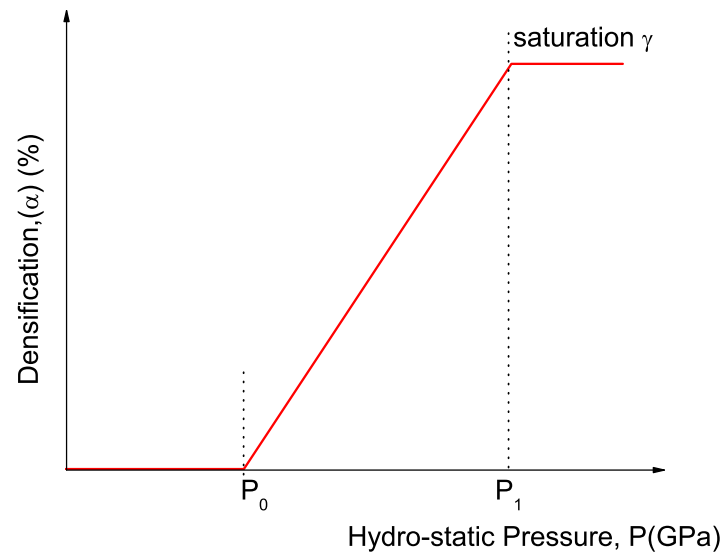


Figure 2.17 Linear assumption of densification.

#### ● In-situ experiments simulation and reverse analysis

In figure 2.4, we extract the data of Sato [Sato 2008, Sato 2011] and Wakabayashi [Wakabayashi 2011] showing loading and unloading of the in-situ experimental process. In order to compare with ex-situ experiment results, we set the maximum load  $P_{\max}$  equal to 25 GPa in ABAQUS file and insert a data for Sato's in-situ loading to 25 GPa by a linear way from his data. Reverse analysis results as shown in table 2.4 and figure 2.18.

Table 2.4 Simulation results of in-situ experiments.

Known values					Unknown values	
$B_0$ (GPa)	$G_0$ (GPa)	$B_{\max}$ (GPa)	$G_{\max}$ (GPa)	$\gamma$	$P_0$ (GPa)	$P_1$ (GPa)
35.5	31.9	74.5	43.7	0.21	9.7	20.6

From figure 2.18, we find our simulation can fit the experiment data very well. For the simulation data, there are three main characters: 1) below 9.7 GPa, the pressure has a linear relationship to volumes change; 2) pressure increase more sharply after 10 GPa; 3) after 20.6 GPa the loading and unloading data of became following the same tendency, and the pressure increase slope is higher than ever before.

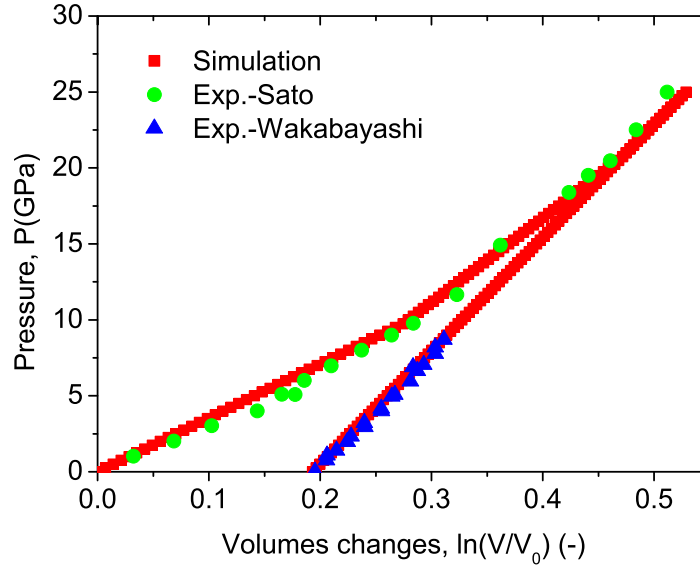


Figure 2.18 Hydrostatic pressure test: Pressure vs Volumes change. Simulation (loading and unloading) vs experiments (Sato, pristine sample; Wakabayashi, fully densified sample).

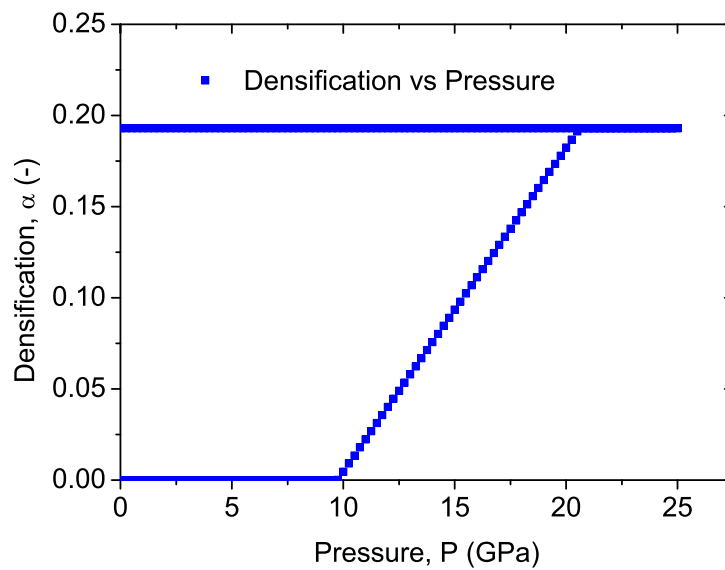


Figure 2.19 Hydrostatic pressure test: Pressure vs Densification.



Since the simulation can fit the experiments' data very well, we can read more information from the simulation results. Figure 2.19 show the densification changes with pressure in the deformed framework.

From figure 2.19, the densification change in a linear way with pressure. the threshold pressure is 9.7 GPa in deformed framework. The saturate pressure is about 20.7 GPa in Euler framework and 12.9 GPa in corotational framework. The maximum densification will reach 21.3%, which is consistent with Wakabayashi's fully densified initial data [Wakabayashi 2011].

As we assume the bulk modulus and shear modulus have linear relation to the densification, our simulation can give us a prediction of the elastic modulus change with pressure, shown in figure 2.20.

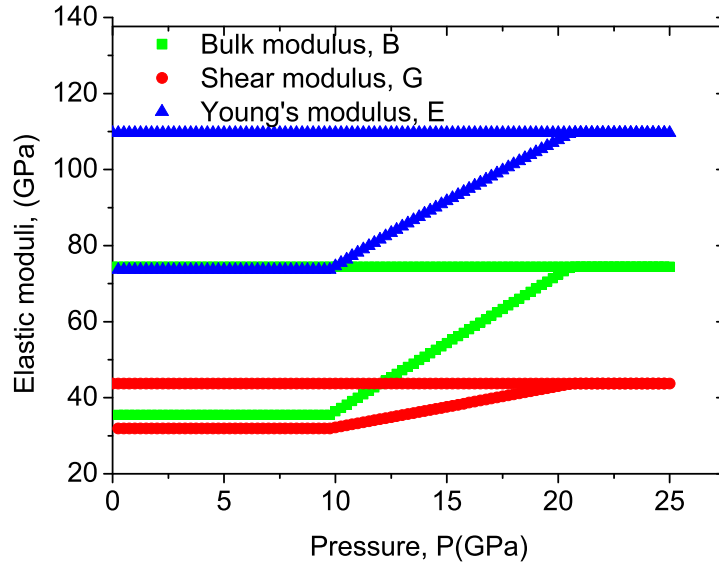


Figure 2.20 Hydrostatic pressure test: Predictions of elastic moduli with pressure.

The permanent bulk modulus will increase after  $P_0$  and reach a maximum value about 74.5 GPa. Similarly, the permanent shear modulus will reach 43.7 GPa and the Young's modulus will reach 109.7 GPa.

Moreover, according to the classic relationship of Poisson's ratio to modulus,  $\nu = \frac{3B - 2G}{6B + 2G}$ , we can predict the changes in Poisson's ratio with pressure, as shown in figure 2.21. From figure 2.21, we can find that the permanent Poisson's ratio starts to increase above the threshold pressure  $P_0$ , then reach a maximum value about 0.255 at the saturation pressure  $P_1$ , then keeps constant at higher pressure and during the unloading process.

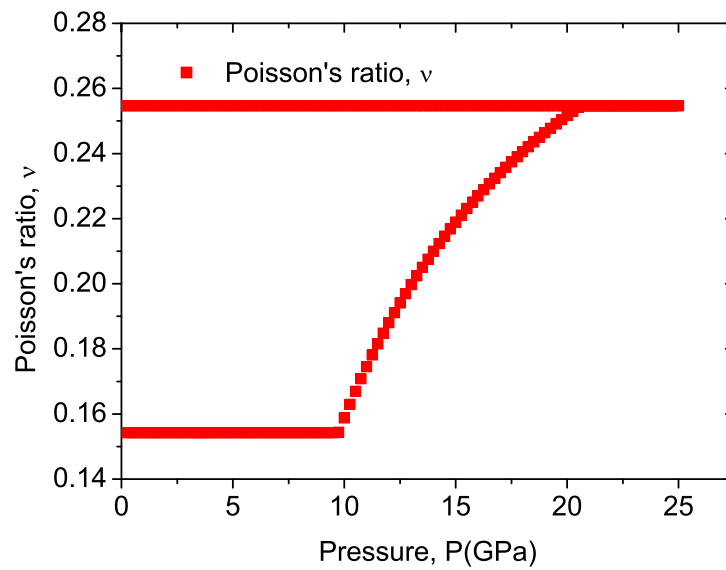


Figure 2.21 Hydrostatic pressure test: Predictions of Poisson's ratio with pressure.

Now let's check the Jacobian ( $J = \frac{V}{V_0}$ ) vs applied pressure, as shown in figure

2.22. we can find that with the applied pressure increase the volume decreases fast, then densification happens, the volume changes slow down. When unloading, the volume change linearly back to its permanent volume about 82.3% of its original. The simulation fits the experimental data very well.

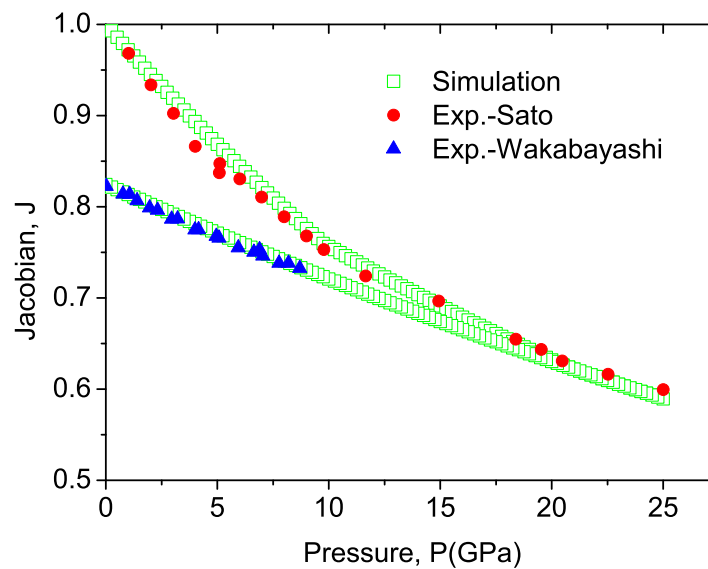


Figure 2.22 Hydrostatic pressure test: Jacobian vs Applied pressure.

### ● Ex-situ experiments simulation and reverse analysis

We use the maximum pressure to do reverse analysis to compare with Ji's ex-situ permanent densification data. For example in figure 2.23a is the loading and unloading process with the maximum pressure to 20 GPa. Figure 2.23b shows the densification changes during the loading and unloading process.

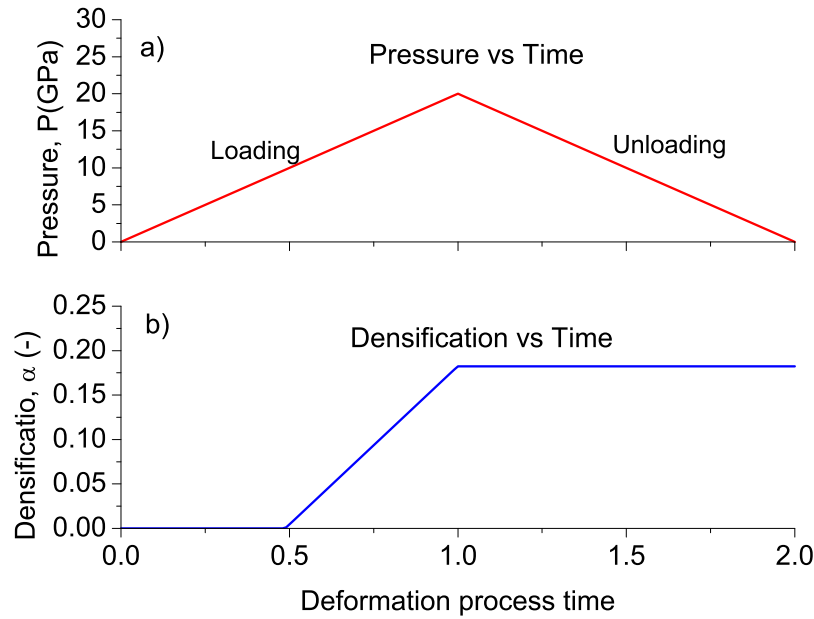


Figure 2.23 Reverse analysis: (a) Pressure vs time; (b) Densification vs Time.

As pictured in figure 2.23, we used four different maximum pressures, 8 GPa, 12 GPa, 20 GPa, and 25 GPa, corresponding to Ji's experimental data. The densifications level changes with different pressures are shown in figure 2.24. In figure 2.24a, use maximum pressure 8 GPa, and the densification is 0. In figure 2.24b, the maximum pressure is 12 GPa, and the densification starts to increase after the threshold, and reach 0.041. Similarly, in figure 2.24c, the maximum pressure is 20 GPa, and the

Table 2.5 Simulation results of ex-situ experiments.

$B_0$ (GPa)	$G_0$ (GPa)	Parameters fixed				Parameters free		
		$B_{\max}$ (GPa)	$G_{\max}$ (GPa)	$\gamma$	$P_{\max}$ (GPa)	$\alpha$	$P_0$ (GPa)	$P_1$ (GPa)
35.5	31.9	74.5	43.7	0.21	8	0	9.7	20.6
35.5	31.9	74.5	43.7	0.21	12	0.041	9.7	20.6
35.5	31.9	74.5	43.7	0.21	20	0.201	9.7	20.6
35.5	31.9	74.5	43.7	0.21	25	0.213	9.7	20.6

densification starts to increase after the threshold, and reach 0.20. Finally, we impose

the maximum pressure to 25 GPa, densification turns to be saturate after the saturation pressure (here  $P_1=20.6$  GPa) and the saturation densification is 0.213. These data are shown in table 2.5.

In order to check our simulation results, we portray the final densification with Ji's experiments data (error is  $\pm 0.005$ ) as shown in figure 2.25. Although, there is a slightly higher of the data at 25 GPa and a little lower at 8 GPa compared to Ji's experimental data, it is reasonable when we consider the error from experimental data. Therefore, we can conclusion that the densification data obtained from simulation fit Ji's experimental data very well.

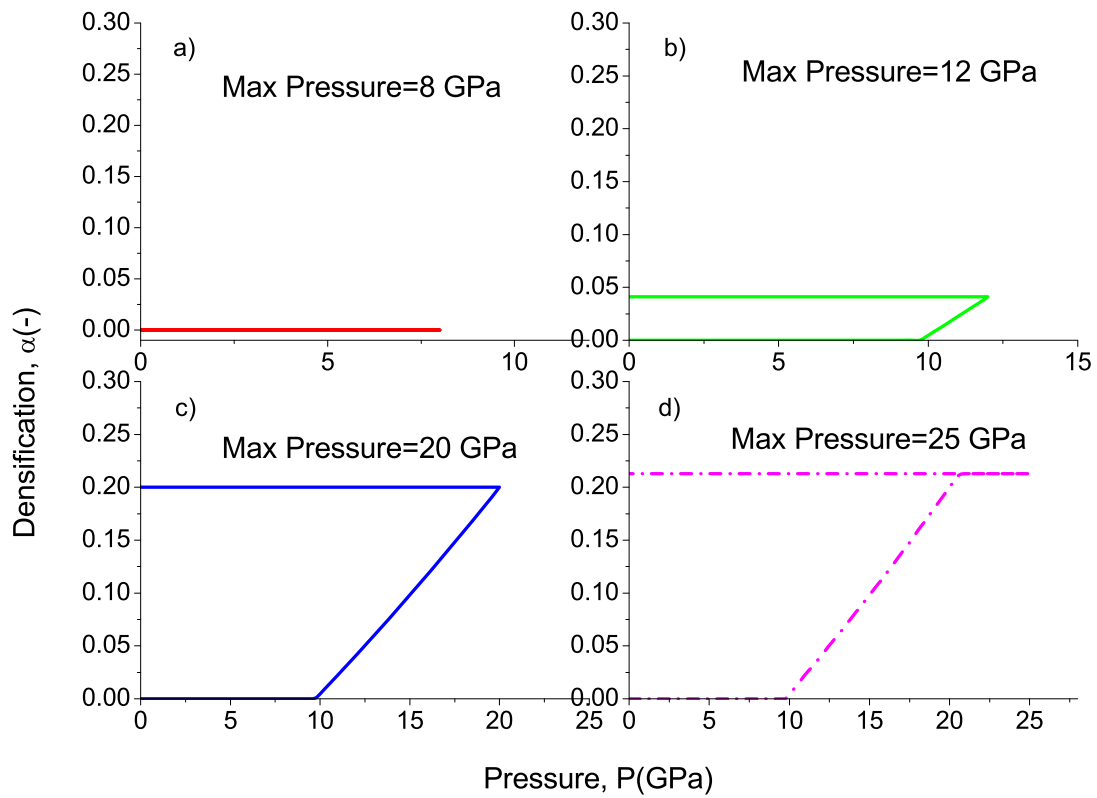


Figure 2.24 Densification at different maximum pressure (8 GPa, 12 GPa, 20 GPa, and 25 GPa, corresponding to Ji's experimental data).

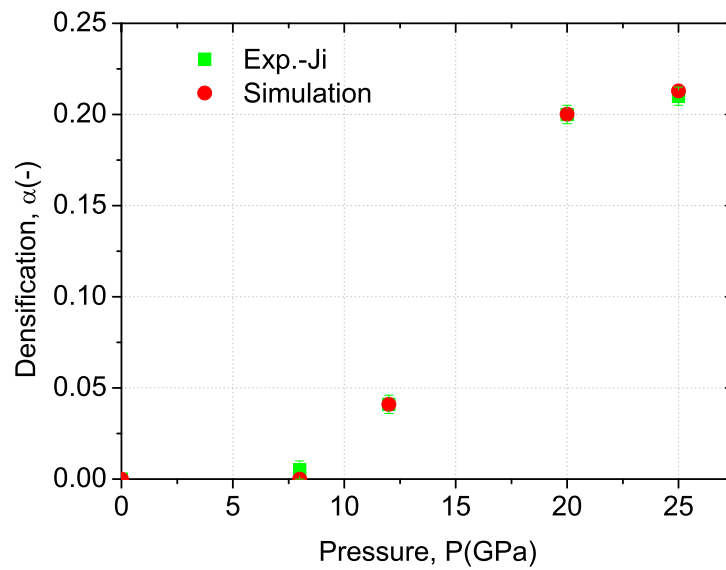


Figure 2.25 Hydrostatic pressure test: Densification vs Maximum applied pressure (Ji's experimental data, error is  $\pm 0.005$ ), Euler framework.

Figure 2.26 and 2.27 show the prediction of elastic moduli and Poisson's ratio with applied maximum pressure. In figure 2.26, it is worth pointing that the bulk modulus can't fit Ji's experimental data at 12 GPa and 20 GPa, but fit the final bulk modulus very well. Besides, shear modulus and Young's modulus all show good agreement with Ji's experimental data.

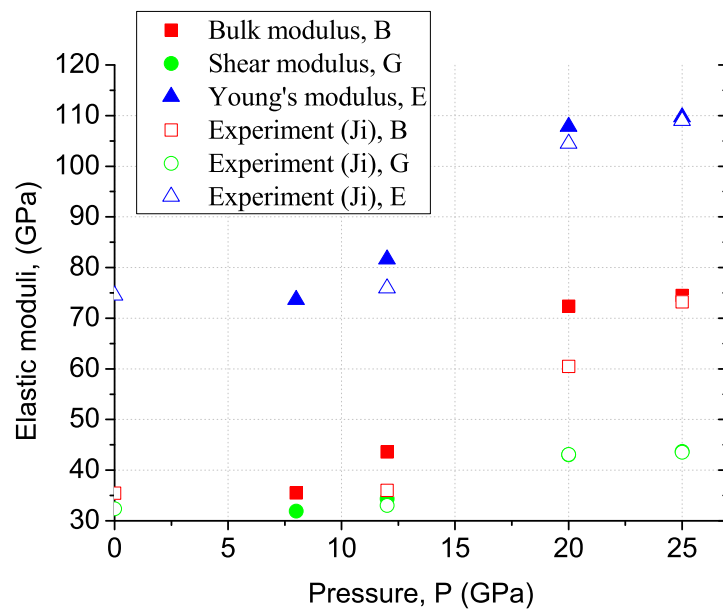


Figure 2.26 Hydrostatic pressure test: Elastic moduli vs Maximum applied pressure (Ji's experimental data).

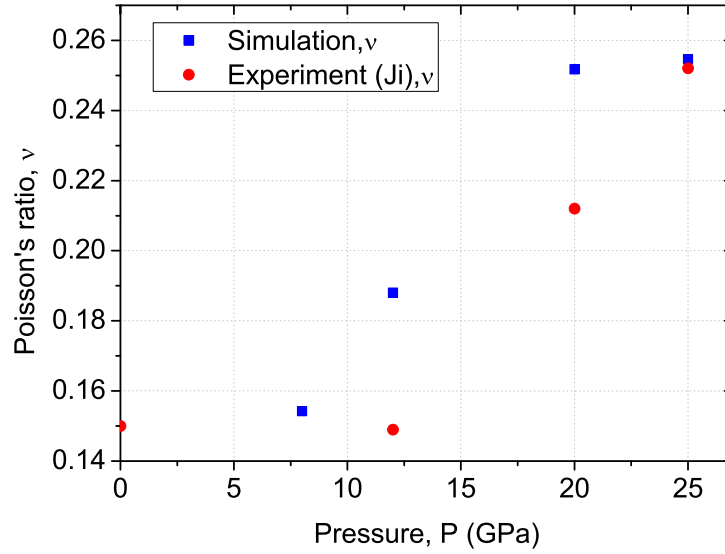


Figure 2.27 Hydrostatic pressure test: Poisson's ratio vs Maximum applied pressure (Ji's experimental data).

In figure 2.27, the Poisson's ratios show a great discrepancy at 12 GPa and 20 GPa, but the final Poisson's ratio at 25 GPa shows very good agreement. This discrepancy may come from the physical relationship between modulus and Poisson's ratio which has been changed after densification or the uncertainty from experimental data.

#### ● Summary

In general, based on a linear assumption, and using the in-situ and ex-situ experimental data, we have succeeded in the reverse analysis. We achieved the excellent densification value which show a good agreement to the published densification, especially for the maximum value of 0.20~0.21, as shown in table 2.6. Moreover, the threshold densification pressure and saturation pressure we obtained are about 9.7 GPa, and 20.6 GPa, respectively, which show good consistency with literature data.

Table 2.6 Reverse analysis results basing on linear hardening rule.

	$P_0$ (GPa)	$P_1$ (GPa)	$\gamma$
Simulation	9.7	20.6	0.213
Ji's EXP	~8	~20	0.20~0.21

Furthermore, we tried to predict the changes of elastic modulus and Poisson's ratio with pressure. The changes of moduli vs densification are shown in figure 2.28. Bulk modulus, shear modulus and Young's modulus all follow a linear relationship with densification. It seems that, shear modulus and Young's modulus show a good agreement with Ji's experimental data, while the bulk modulus and Poisson's ratio show a big discrepancy at the pressure of 12 GPa and 20 GPa.

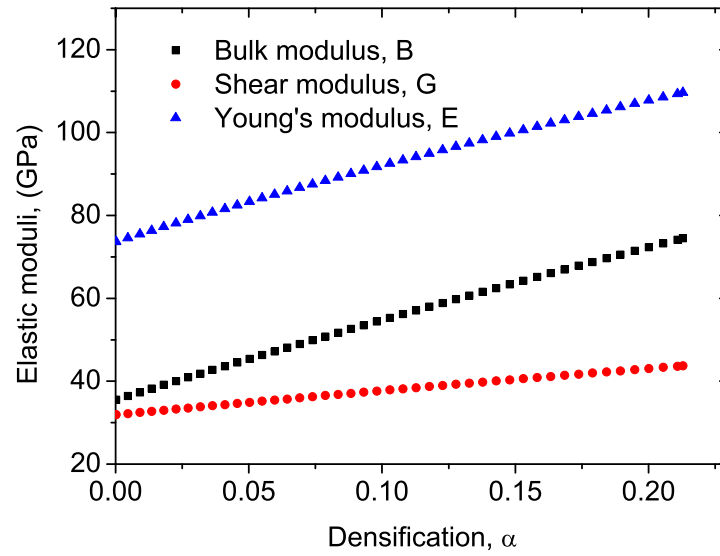


Figure 2.28 The changes of moduli vs densification.

### 2.4.3.2 *Atan(P) function assumption and Results*

The linear assumption gives good values of  $P_0$  and  $P_1$ , but there exist a discrepancy when we use it to predict the bulk modulus and Poisson's ratio, therefore we turn to use an  $\text{atan}(P)$  assumption to portray the hardening rule, as shown in figure 2.29. This assumption means that the densification versus pressure follows an  $\text{atan}(P)$  function  $\alpha = F(\text{atan}(P))$ . In order to check the assumption we try to fit with Ji's ex-situ densification data, as shown in figure 2.30. Obviously,  $\text{atan}(P)$  function can fit Ji's experimental data very well as long as we use proper mathematical parameters.

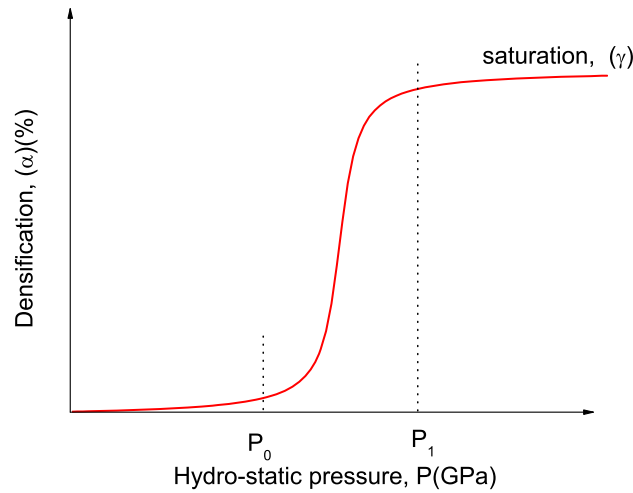


Figure 2.29 Illustration of Atan (P) assumption.

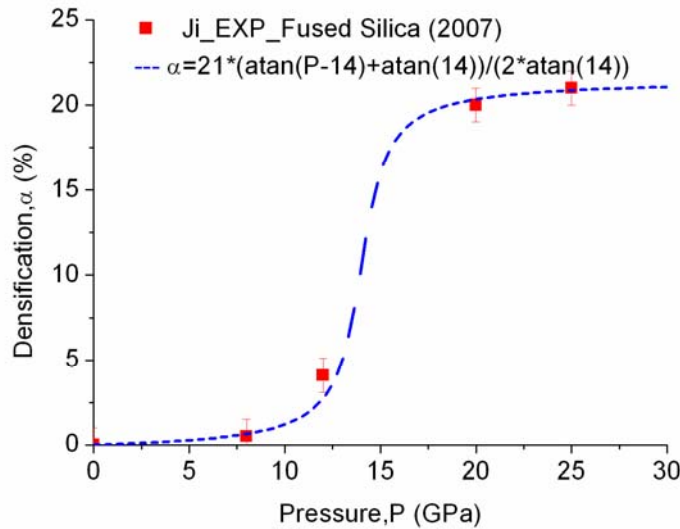


Figure 2.30 Use Atan (P) function to fit Ji's permanent densification vs pressure.



### ● In-situ experiments simulation and reverse analysis

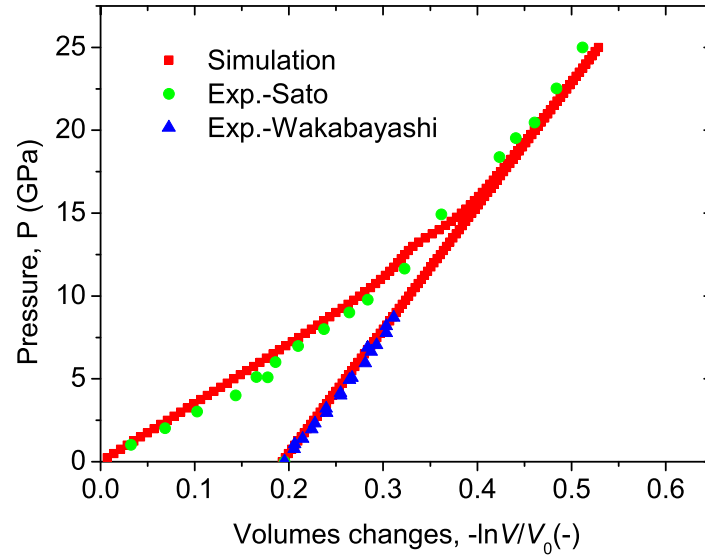


Figure 2.31 Hydrostatic pressure test: Pressure vs Volumes change. Simulation (loading and unloading) vs experiments (Sato, pristine sample; Wakabayashi, fully densified sample).

Using the  $\text{atan}(P)$  function, we program our model and execute reverse analysis. Figure 2.31 show the in-situ reverse analysis results for hydrostatic pressure case: pressure versus volumes changes. From figure 2.31, we can find that, our simulation has a good agreement to in-situ experiments. For loading process, our simulation can fit Sato's experimental data [Sato 2008, Sato 2011]. It is interesting that around 12 GPa, there exists an unexpected abrupt, then turns to another slope. For unloading process, our simulation can fit Wakabayashi's fully densified silica behavior. Figure 2.32 show the densification changes under pressure. As  $\text{atan}(P)$  function presents a very slowly increase at the start, the densification occurs at 1.0 GPa, and finish at 25.0 GPa. That means  $P_0$  and  $P_1$  is 1.0 GPa and 25.0 GPa, respectively. We take densification equal 0.001 as the starting threshold where  $P_0^*$  is 9.1 GPa, and the saturation take the densification to 0.210 where the pressure  $P_1^*$  is 21.8 GPa in deformed framework.

Our simulation predicts the elastic modulus changes and Poisson's ratio changes with pressure as shown in figure 2.33 and 2.34. The permanent bulk modulus ( $B$ ) will reach 74.5 GPa, and the permanent shear modulus and Young's modulus will reach 43.7 GPa and 109.7 GPa, respectively. The Poisson's ratio will reach 0.255 after saturation.

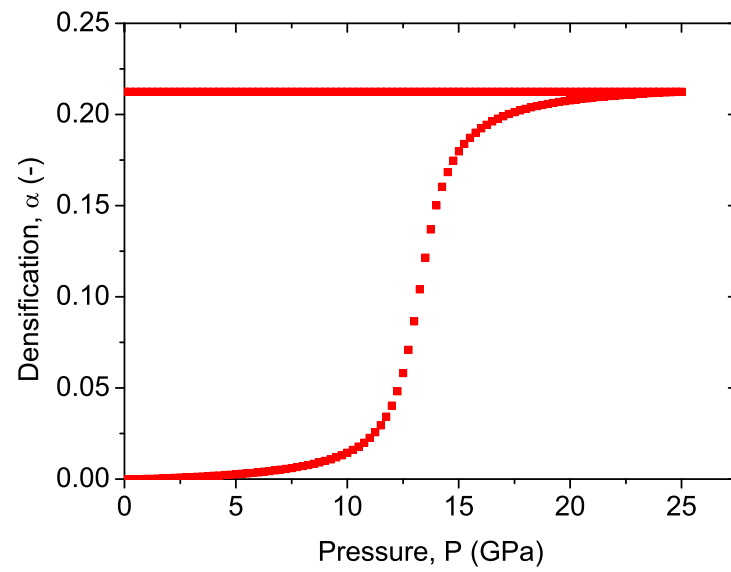


Figure 2.32 Hydrostatic pressure test: Pressure vs Densification.

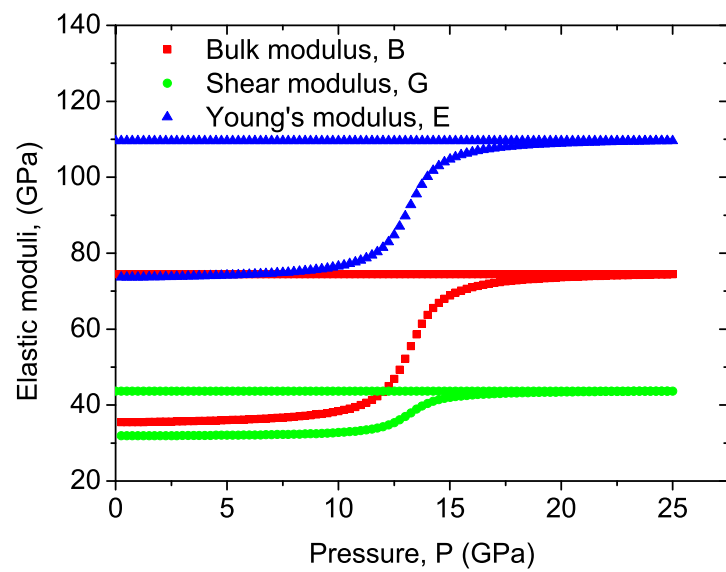


Figure 2.33 Hydrostatic pressure test: Predictions of elastic moduli with pressure.

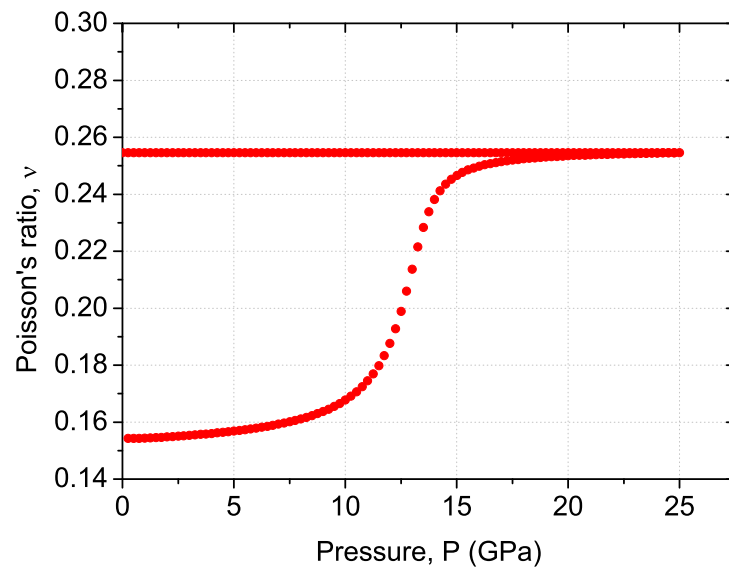


Figure 2.34 Hydrostatic pressure test: Predictions of Poisson's ratio with pressure.

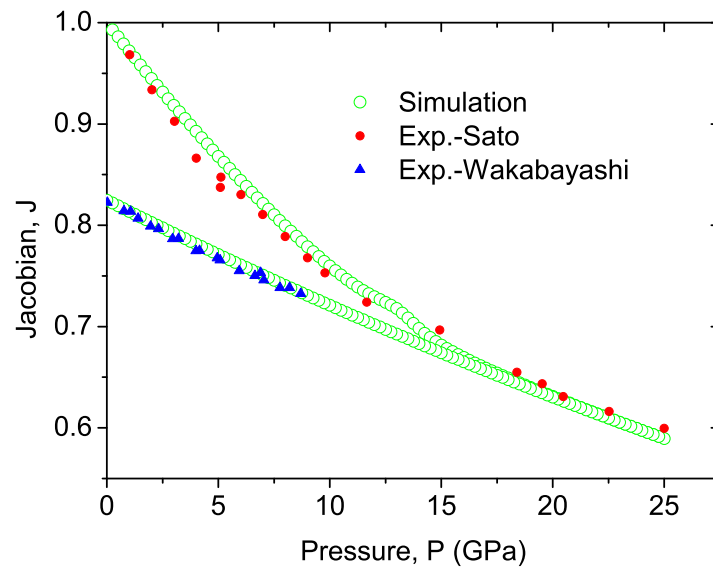


Figure 2.35 Hydrostatic pressure test: Jacobian vs Applied pressure.

In order to verify our simulation, we plot the Jacobian versus applied pressure, as shown in figure 2.35. In figure 2.35, it is clear that our simulation can fit experiments' data very well. The permanent value of Jacobian after decompression is 0.822.

### ● Ex-situ experiments simulation and reverse analysis

We use  $\text{atan}(P)$  assume to do reverse analysis of ex-situ experiments data of Ji's thesis work [Ji 2007]. In order to get the proper parameter of  $P_0$  and  $P_1$ , we free  $P_0$  and  $P_1$ , fix  $B_0, G_0, G_{\max}, B_{\max}, \gamma$ , the results as shown in the following figures.

We use ABAQUS DLOAD way to carry out our simulation, which means we use the maximum applied pressure to 25 GPa for loading and unloading. Figure 2.36 shows the results of densification at different applied pressure.  $\text{Atan}(P)$  function presents slow increase at first, so it gives a very low of densification below the pressure 8 GPa, which Ji's experiment get densification of 0.005. the very fast increase of densification is around 13 GPa, then it reaches saturation state at the high pressure of 20 GPa.

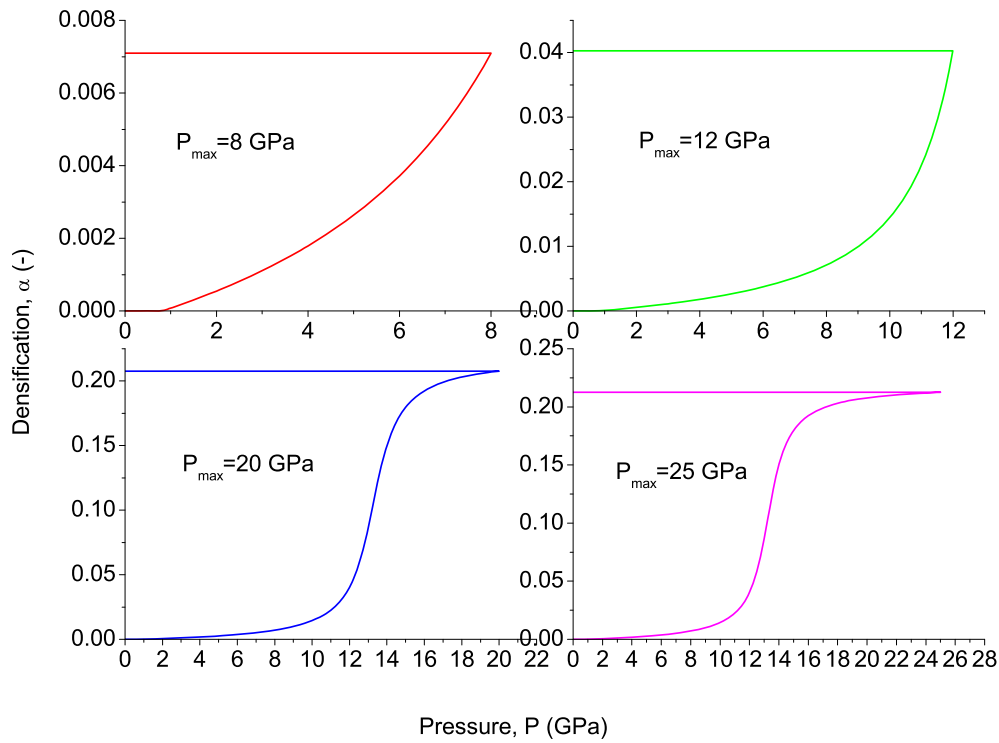


Figure 2.36 Densification at different maximum pressure ( $\text{Atan}(P)$  assumption. 8 GPa, 12 GPa, 20 GPa, and 25 GPa, corresponding to Ji's experimental data).

Figure 2.37 shows the permanent densification compared with Ji's data. The error of Ji's experiment is 0.005. From figure 2.36, we can find that, our simulation results fit Ji's data very well. Figure 2.38 presents the predictions of the changes in elastic moduli with pressure. The bulk modulus, at 20 GPa, presents a discrepancy with experiments data. It is almost 13 GPa higher than Ji's tests. Except this point, the others seems all fit well, that's means our model can predict the changes in elastic properties under high pressure of silica.

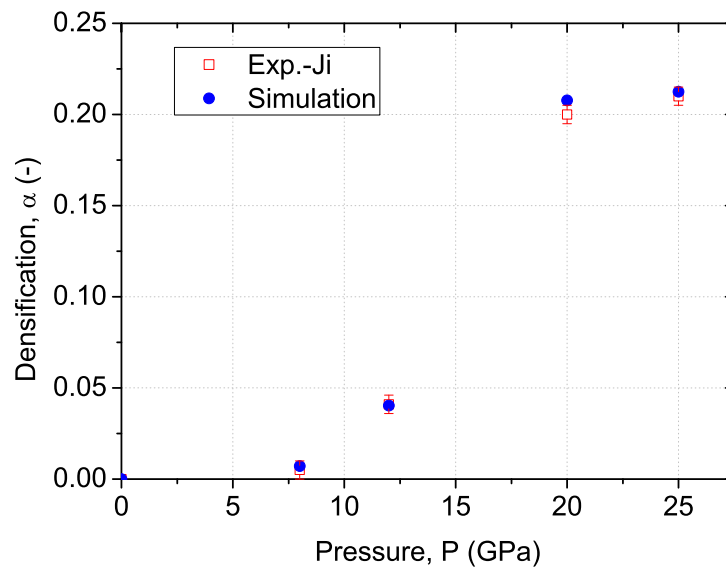


Figure 2.37 Hydrostatic pressure test: Densification vs Maximum applied pressure (Ji's experimental data, error is  $\pm 0.005$ ).

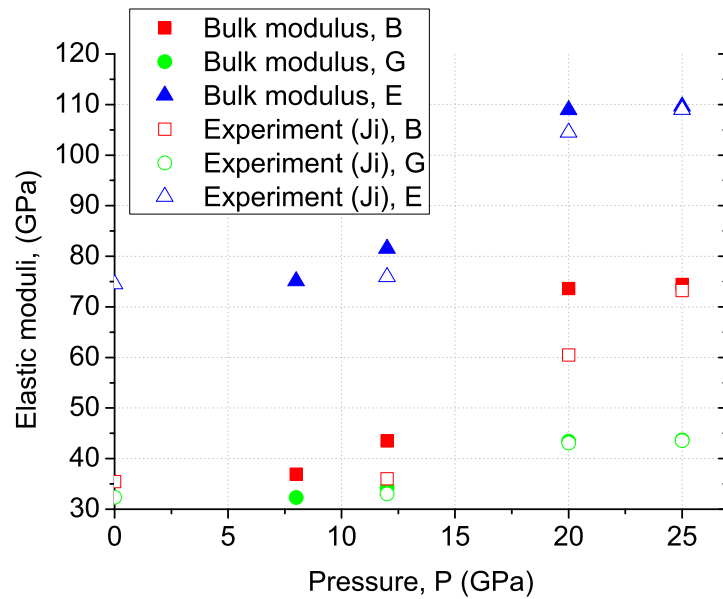


Figure 2.38 Hydrostatic pressure test: Elastic moduli vs Maximum applied pressure.

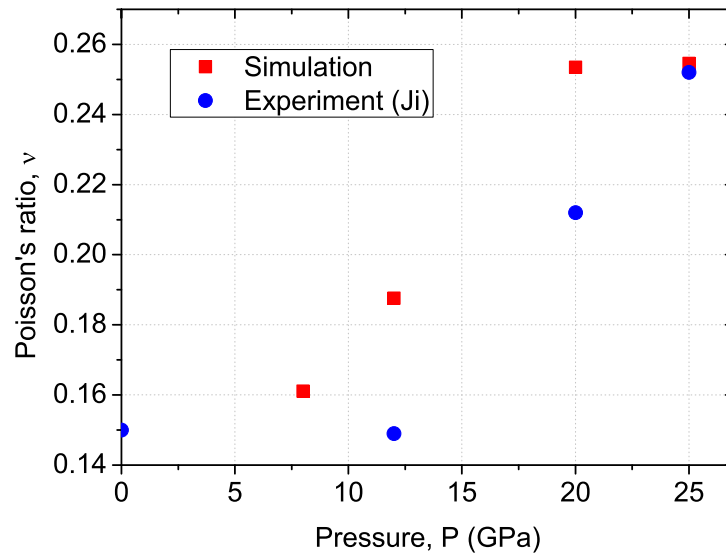


Figure 2.39 Hydrostatic pressure test: Poisson's ratio vs Maximum applied pressure, Euler framework.

Figure 2.39 shows our model predictions of Poisson's ratio at different applied pressure. there exist a big discrepancy at the pressure of 12 GPa and 20 GPa compared with Ji's data. However, it predicts the permanent Poisson's ratio will reach 0.255 which can fir Ji's experimental data 0.252.

### ● Summary

Table 2.7 Reverse analysis results basing on Atan(P) hardening rule.

	$P_0$ (GPa)	$P_0^*$ (GPa)	$P_1$ (GPa)	$P_1^*$ (GPa)	$\gamma$ (%)	$B_{\max}$ (GPa)	$G_{\max}$ (GPa)
Simulation	1.0	9.1	25.0	21.8	21.3	74.4	43.7
Ji's EXP	~8		~20		20~21	73.3	43.5

- i) We have succeeded using Atan(P) assumption to simulate the densification phenomenon of silica under high pressure.
- ii) The threshold pressure of densification is around 8-10 GPa. At 9.1 GPa, the densification value reaches 0.001 in our simulation. The saturation pressure is around 21.8 GPa, as shown in table 2.7.
- iii) Our simulation has a good agreement with in-situ experimental data [Sato 2008, Sato 2011, Wakabayashi 2011].
- iv) We predict the permanent changes in elastic modulus and Poisson's ratio, most of them can fit ex-situ experimental data [Ji 2007, Rouxel 2008, Rouxel 2010] very well.

### 2.4.3.3 Avrami equation assumption and Results

#### a. General

The Avrami equation, also known as Johnson-Mehl-Avrami-Kolmogorov (JMAK) equation, describes how solids transform from one phase (state of matter) to another at constant temperature. It can specifically describe the kinetics of crystallization, can be applied generally to other phase changes in materials, like chemical reaction rates, and can even be meaningful in analyses of ecological systems. Avrami type plots show a linear fit over all conversions but have non-integer values of slope as shown in figure 2.40. [ [http://en.wikipedia.org/wiki/Avrami\\_equation](http://en.wikipedia.org/wiki/Avrami_equation) ]

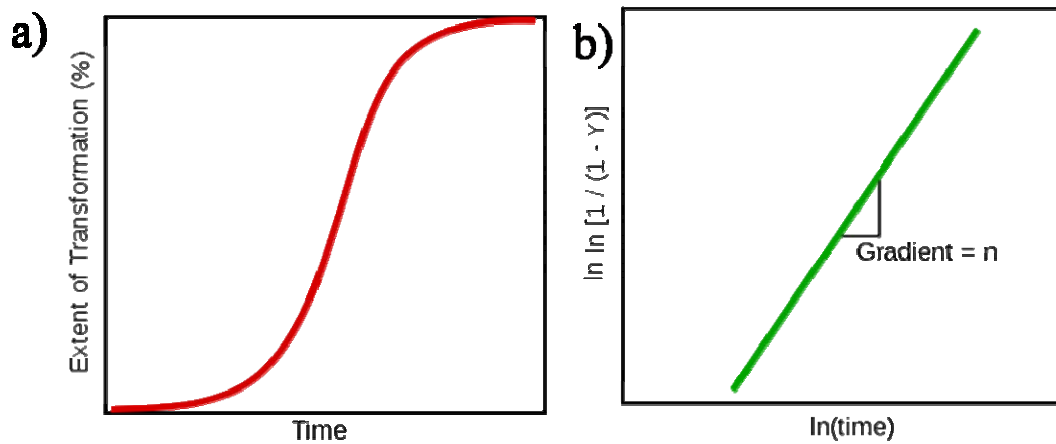


Figure 2.40 Avrami type plots. [ [http://en.wikipedia.org/wiki/Avrami\\_equation](http://en.wikipedia.org/wiki/Avrami_equation) ]

In general,

$$x(t) = 1 - \exp\left[-\left(\frac{t}{\tau}\right)^m\right] \quad (2.17)$$

-- Johnson-Mehl-Avrami-Kolmogorov equation

The parameter 'm' depends on shape of  $\beta$ -phase particles (the Dimension):

spherical  $\rightarrow m=3$ ; disk-shaped  $\rightarrow m=2$ ; rod-shaped  $\rightarrow m=1$

(3D)

(2D)

(1D)

If nucleation occurs concurrently with growth, for 3D spherical particle, m can be 4 or 5 under various conditions.

#### b. Application to densification

The initial slow rate and the transformation of density ( $\alpha/\gamma \in [0.0001, 0.9999]$ ) of silica under hydro-static pressure seems origin from the inner structure change. Then we use this mathematical function to our pressure and densification, we can use as

below function:

$$P(\alpha/\gamma) = P_0 + (P_1 - P_0) * \left( -\frac{\ln(1 - \alpha/\gamma)}{\tau} \right)^m \quad (2.18)$$

For the density permanent change in 3D structure of silica, we determine  $m=4$  and  $\tau=2$  to fit Ji's data.

### ● In-situ experiments simulation and reverse analysis

We use JMAK assumption for the hardening rule to simulate the densification behavior of silica under hydrostatic pressure and execute reverse analysis to compare with experimental data. We present our simulation with the in-situ experimental data as below.

Figure 2.41 show the result of pressure versus volume changes for in-situ experiments [Sato 2008, Sato 2011, Wakabayashi 2011]. From figure 2.41, we can find that our results satisfy the in-situ experimental data very well.

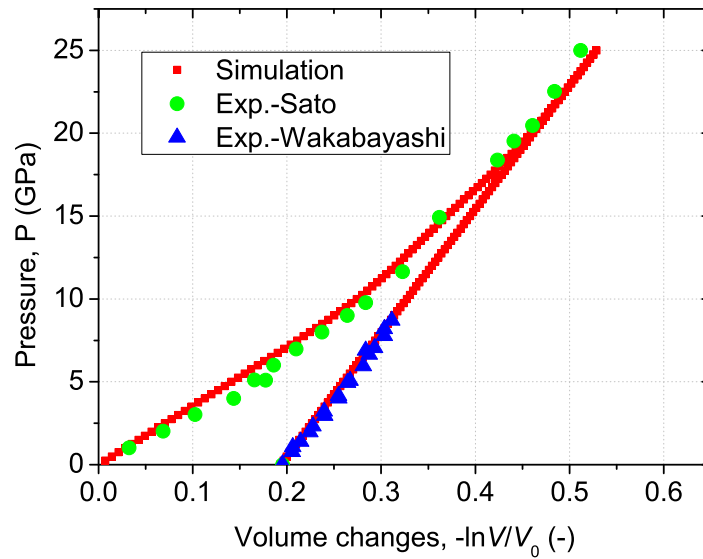


Figure 2.41 Hydrostatic pressure test: Pressure vs Volumes change. Simulation (loading and unloading) vs experiments (Sato, pristine sample; Wakabayashi, fully densified sample).

Figure 2.42, shows the densification changes with pressure. It starts very slowly at first at 3.0 GPa, then increase sharply after 9.25 GPa, where the densification reaches 0.011. At 20.2 GPa, the densification reach 0.20 and then increase very slowly, until 25.0 GPa reach the maximum. So we take 3.0 GPa and 25 GPa as the threshold pressure  $P_0$  and saturation pressure  $P_1$ , and 9.25 GPa and 20.2 GPa as the approximate threshold pressure  $P_0^*$  and approximate saturation pressure  $P_1^*$ .



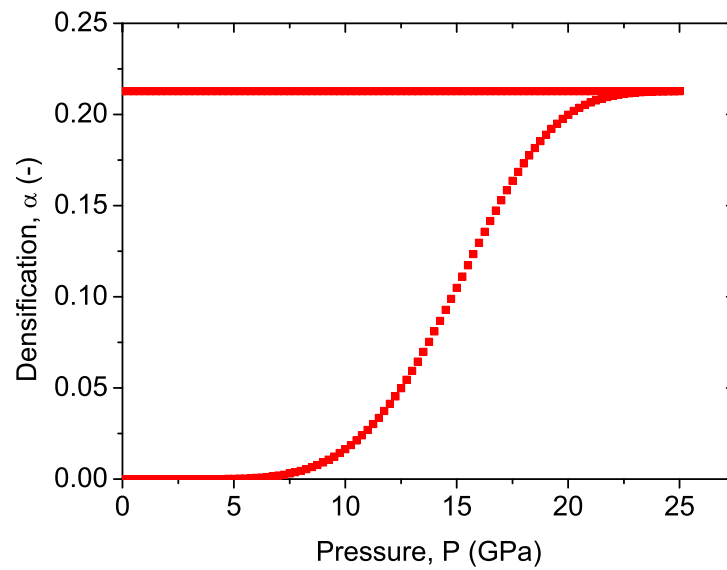


Figure 2.42 Hydrostatic pressure test: Pressure vs Densification.

Figure 2.43 and figure 2.44 show the changes in elastic moduli and Poisson's ratio, respectively. From figure 2.43 we can find that all the data changes smoothly follow JMAK assumption. The permanent changes of bulk modulus, shear modulus and Young's modulus will reach 74.5 GPa, 43.7 GPa and 109.7 GPa. The Poisson's ratio will reach 0.255 after saturation.

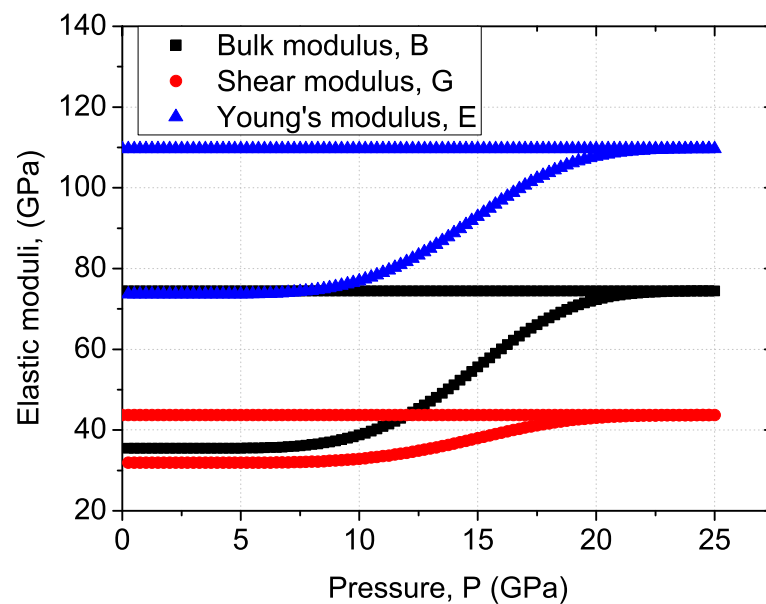


Figure 2.43 Hydrostatic pressure test: Elastic moduli vs Pressure.

Figure 2.45 shows the Jacobian changes with pressure both for loading and

unloading. It is clear that, our simulation can satisfy the in-situ experimental data from Sato and Wakabayashi et al.

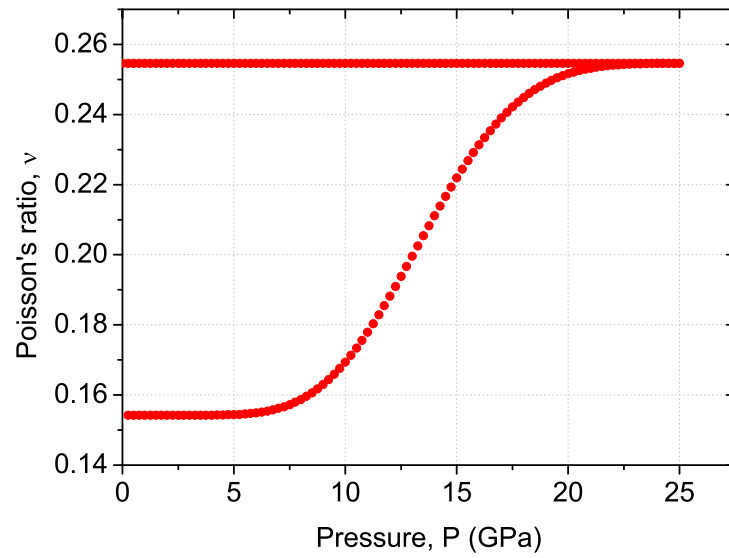


Figure 2.44 Hydrostatic pressure test: Predictions of Poisson's ratio with pressure.

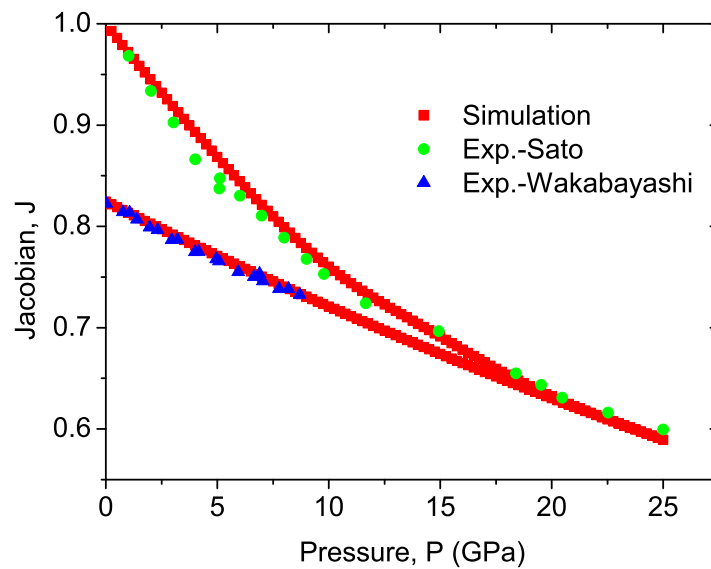


Figure 2.45 Hydrostatic pressure test: Jacobian vs pressure.

### ● Ex-situ experiments simulation and reverse analysis

According to Ji's experimental maximum pressure ( $P_{\max}$ ), we simulate at different  $P_{\max}$  (8 GPa, 12 GPa, 20 GPa and 25 GPa) the densification behavior and verify it with Ji's experimental data.

The densification versus pressure results as shown in figure 2.46. When pressure reaches 2.85 GPa, densification happens. Then, densification slowly increases until 9.25 GPa to reach 0.011. After that, densification increase sharply, to reach near saturation. At the pressure of 20.25 GPa densification reach 0.202, where saturation begins.

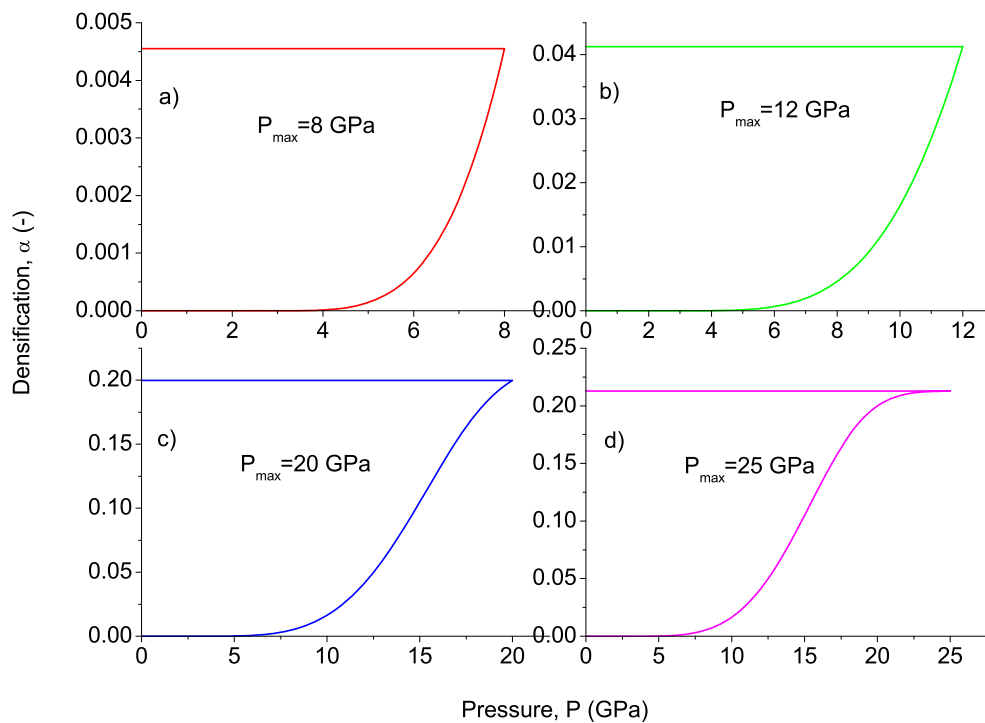


Figure 2.46 Densification at different maximum pressure (8 GPa, 12 GPa, 20 GPa, and 25 GPa, corresponding to Ji's experimental data).

Figure 2.47 presents the densification of simulation and experimental data at different applied pressures. Simulation results can fit experimental data very well. Figure 2.48 shows the elastic moduli at different applied maximum pressure. We need to point out that shear modulus can fit all experimental data. Interestingly, bulk modulus presents the biggest discrepancy at 20 GPa, but Young's modulus fit well at this pressure. Figure 2.49 shows the predictions of Poisson's ratio at different pressure. It seems that our simulation only can predict the permanent Poisson's ratio at 25 GPa, and there exist a difference with Ji's data.

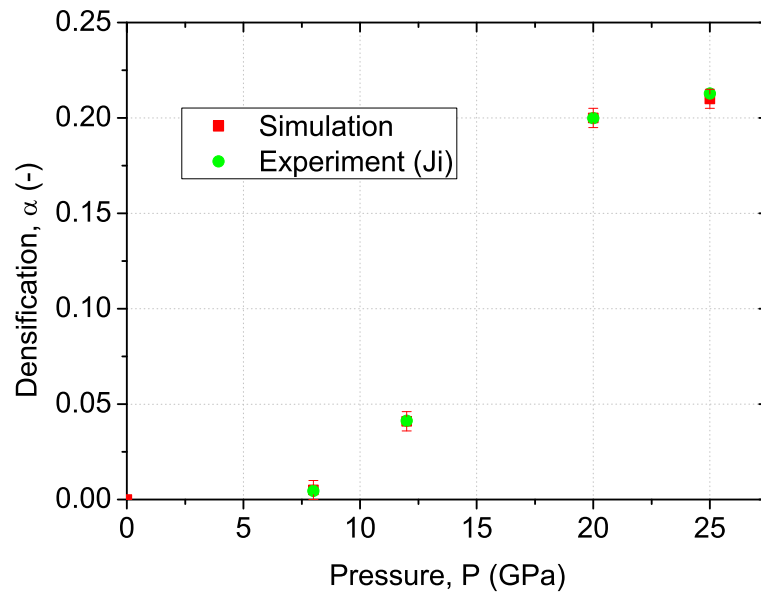


Figure 2.47 Hydrostatic pressure test: Densification vs Maximum applied pressure (Ji's experimental data, error is  $\pm 0.005$ ).

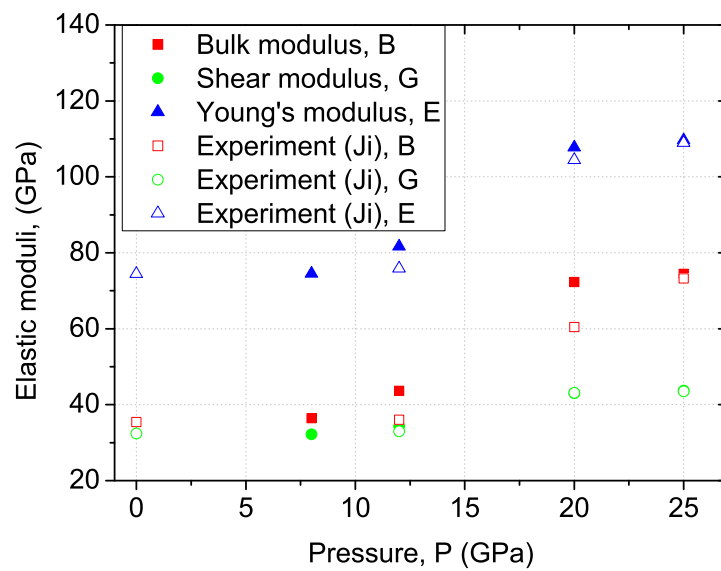


Figure 2.48 Hydrostatic pressure test: Elastic moduli vs Maximum applied pressure (Ji's experimental data).

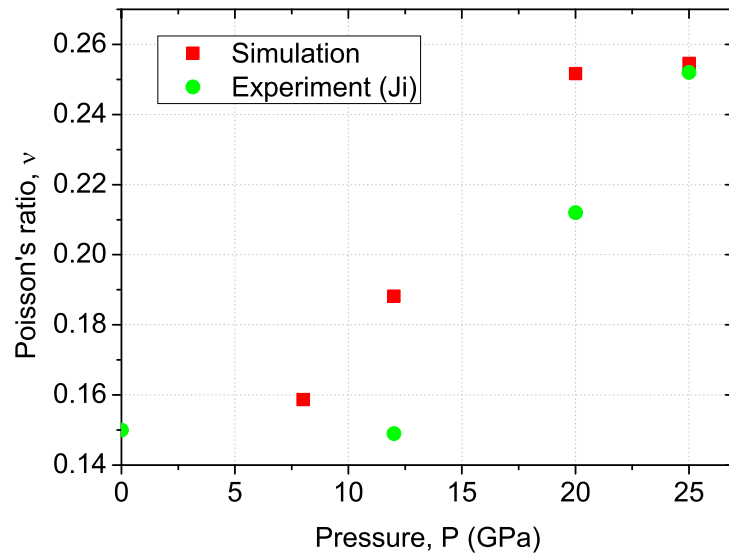


Figure 2.49 Hydrostatic pressure test: Poisson's ratio vs Maximum applied pressure.

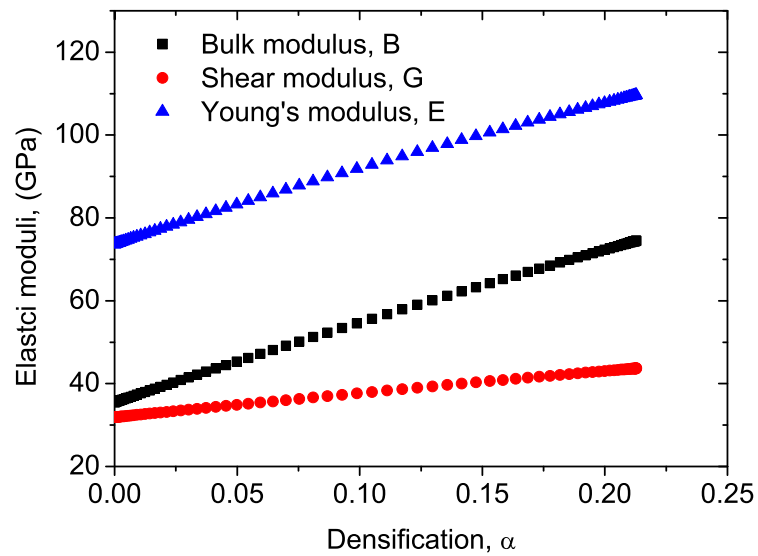


Figure 2.50 Elastic moduli vs densification.

Figure 2.50 shows the elastic moduli versus densification. It shows that all the moduli follow a linear relationship to densification, that means the results follow our linear assumption used between elastic moduli and densification. However, a not linear relationship turns out between Poisson's ratio and densification, as shown in figure 2.51.

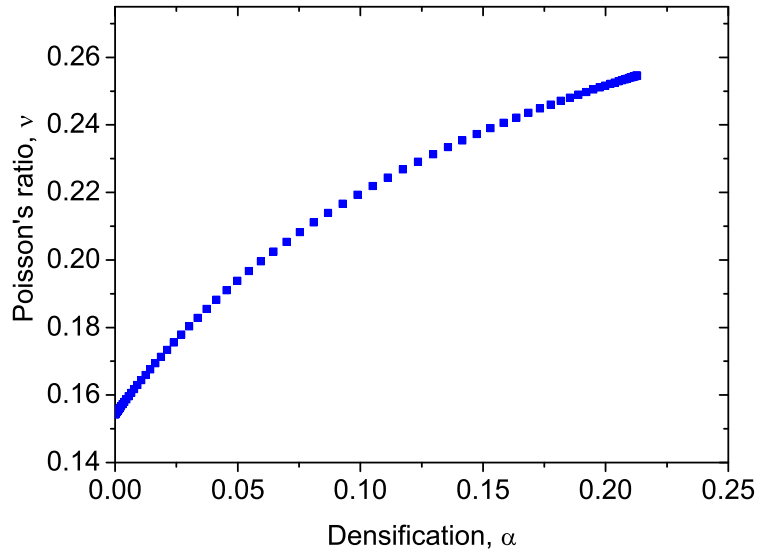


Figure 2.51 Poisson's ratio vs densification.

### ● Summary

Table 2.8 Reverse analysis results basing on JMAK hardening rule.

	$P_0$ (GPa)	$P_0^*$ (GPa)	$P_1$ (GPa)	$P_1^*$ (GPa)	$\gamma$ (%)	$B_{\max}$ (GPa)	$G_{\max}$ (GPa)
Simulation	3.0	9.25	25.0	20.2	21.3	74.4	43.7
Ji's EXP	~8		~20		20~21	73.3	43.5
Wakabayashi					21	75.4	

In general, using Avrami equation assumption our simulation can fit both ex-situ and in-situ experiment well. The results are shown in table 2.8 and can be categorized as below:

- i) The starting rate of densification is very slowly, the initial densification pressure starts from 3.0 to 9.25 GPa.
- ii) There exist great change rate after the pressure 9 GPa and stop at around 20 GPa.
- iii) For densification factor, our model can fit the densification with pressure very well.
- iv) Furthermore, we succeed in using linear assumption to predict the changes of elastic moduli. Although there is a little difference at some pressure for bulk modulus and Young's modulus, most of the results can fit experimental data.
- v) This model can predict the saturation Poisson's ratio.

## 2.5 Conclusion and discussion

In order to see the difference among the different assumptions for the hardening rule, we plot those simulation results and experimental data in figure 2.49. It shows that the volume changes with pressure, linear assumption, atan(P) assumption and JMAK assumption simulation results all have good agreement to Sato and Wakabayashi's in-situ experimental data. The residual of the simulation are 30.9 for linear assumption, 50.7 for atan(P) assumption and 5.9 for JMAK assumption, therefore, JMAK assumption gives us the best fit.

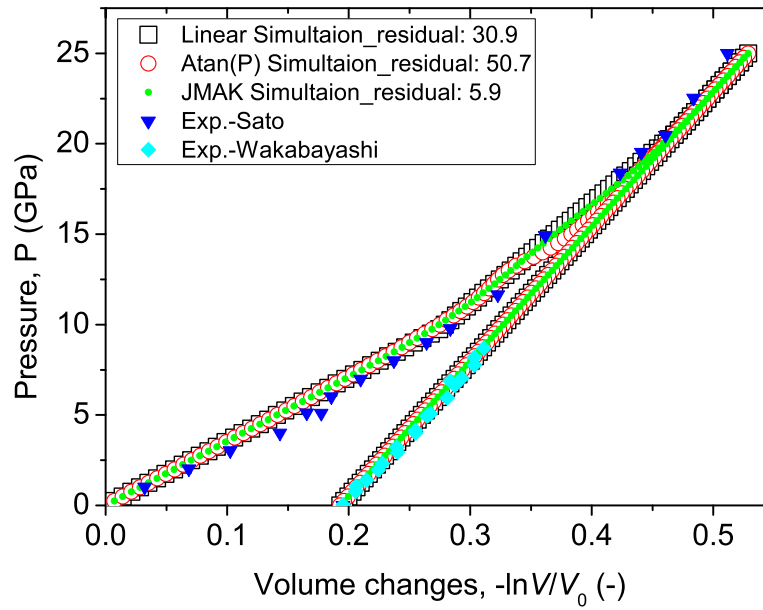


Figure 2.52 Hydrostatic pressure test: Volume changes vs Pressure.

Figure 2.50 show the densification versus pressure, it is clear that, all simulation give excellent fit to ex-situ experimental data. For linear hardening rule, the threshold pressure is 9.7 GPa, and the saturate pressure is around 20.6 GPa. As atan(P) and assumption and JMAK have a very slow increase at low pressure, we take the threshold pressure at densification reach 0.01, then  $P_0$  is 9.25 GPa. Simarily, we take the saturation pressure for densification reach 0.201, then  $P_1$  is 20.25 GPa.

We assume bulk modulus and shear modulus have a linear relationship with densification to predict the changes of elastic modulus. Figure 2.53 shows our predictions of bulk modulus changes with pressures. It seems that, our simulation can not predict the whole process. The permanent bulk modulus after decompression from 25 GPa is 74.4 GPa, which can fit Ji's 73.3 GPa and Wakabyashi's 75.4 GPa.

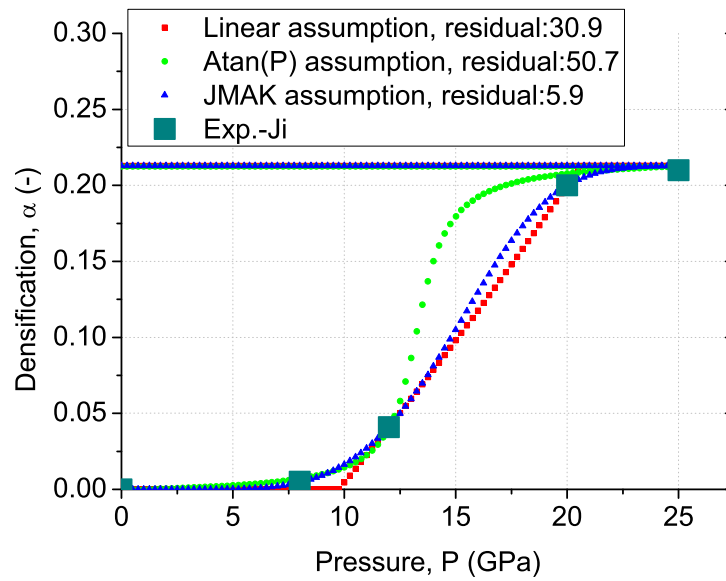


Figure 2.53 Hydrostatic pressure test: Densification changes vs Pressure.

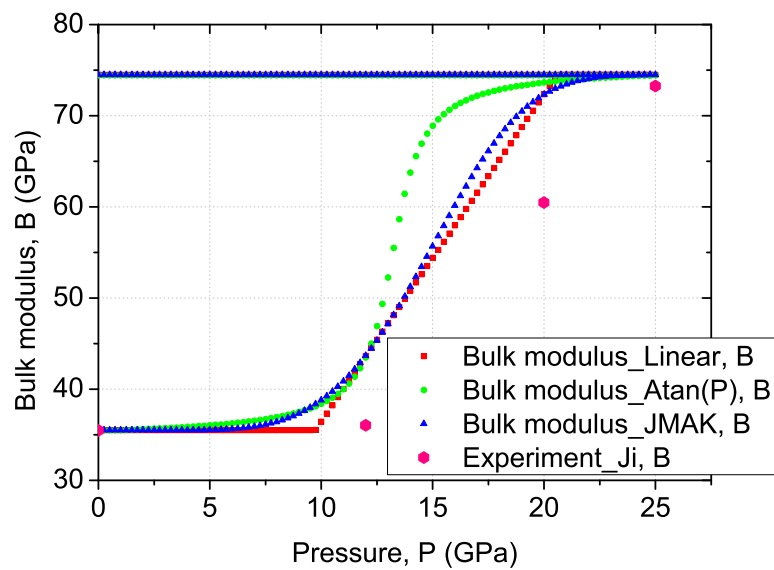


Figure 2.54 Hydrostatic pressure test: Bulk modulus changes vs Pressure.

Figure 2.55 shows the changes of shear modulus for the three assumptions with pressure. From the figure, we found that all the simulation can satisfy Ji's ex-situ experimental results, especially JMAK assumption simulation can fit the Ji's data best. The permanent shear modulus will reach 43.7 GPa after decompression.



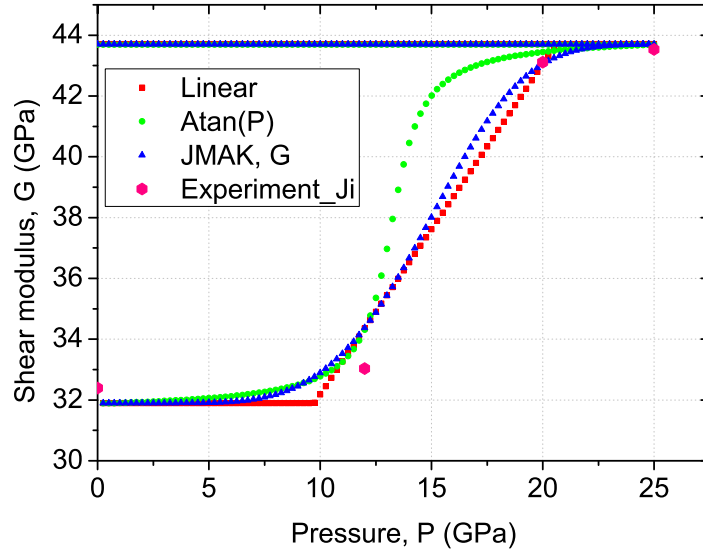


Figure 2.55 Hydrostatic pressure test: Shear modulus changes vs Pressure.

According to the classic relationship  $E = \frac{9BG}{3B + G}$ , we predict the changes of Young's modulus with pressure as shown in figure 2.56. It is interesting to point out that our simulations all give a little bit higher value compared to Ji's data at the pressure of 12 GPa and 20 GPa. However, the permanent Young's modulus can fit Ji's data very well.

According to the classic relationship  $\nu = \frac{3B - 2G}{6B + 2G}$ , we predict the changes of Poisson's ratio with pressure as shown in figure 2.57. Comparing with Ji's ex-situ data and Zha's [Zha 1994] in-situ decompression data from 57.5 GPa, we found that Ji's Poisson's data at the pressure of 20 GPa almost equal Zha's result around 0.21. The Poisson's ratios from our simulation higher than Ji's data at 20 GPa, but fit well at 25 GPa. The difference may come from the inaccuracy of experiments at slow change rate state or the hardening rule will be more complex than what we have assumed. Furthermore, shear flow, as a promotion factor has a great impact during the densification process, which may impact the hardening rule especially at higher pressure.

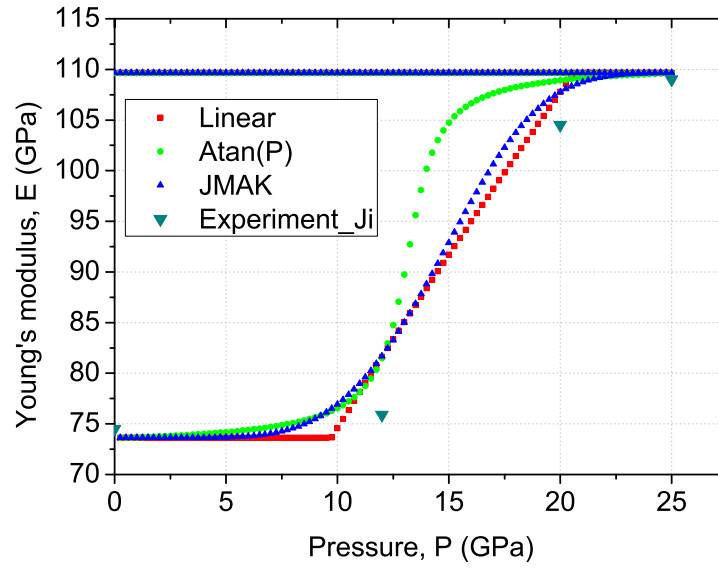


Figure 2.56 Hydrostatic pressure test: Young's modulus changes vs Pressure.

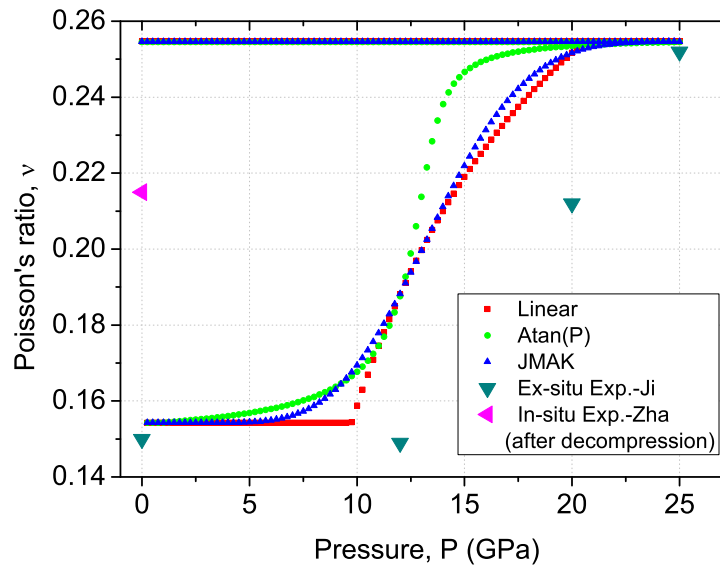


Figure 2.57 Hydrostatic pressure test: Poisson's ratio changes vs Pressure.

Based on the information we collected for the change of Raman shifts, we found that it seems has the same tendency as densification as shown in figure 2.58 [Wakabayashi 2011, Sato 2011, Deschamps 2011, Huang 2004, Rouxel 2008, Sugiura 1997, Benmore 2010]. The Raman shift has a direct relation to the inner structure, which means the densification phenomenon stems from the permanent changes of

structure, especially the changes in coordination rings number of silica. Figure 2.59 shows the changes of 4<sup>th</sup>, 5<sup>th</sup> and 6<sup>th</sup> coordination rings [Liang 2007]. With the pressure increase, the 4<sup>th</sup> rings will decrease and 5<sup>th</sup>, 6<sup>th</sup> rings will increase. The increase percent of 6<sup>th</sup> rings may have a linear relationship to the densification.

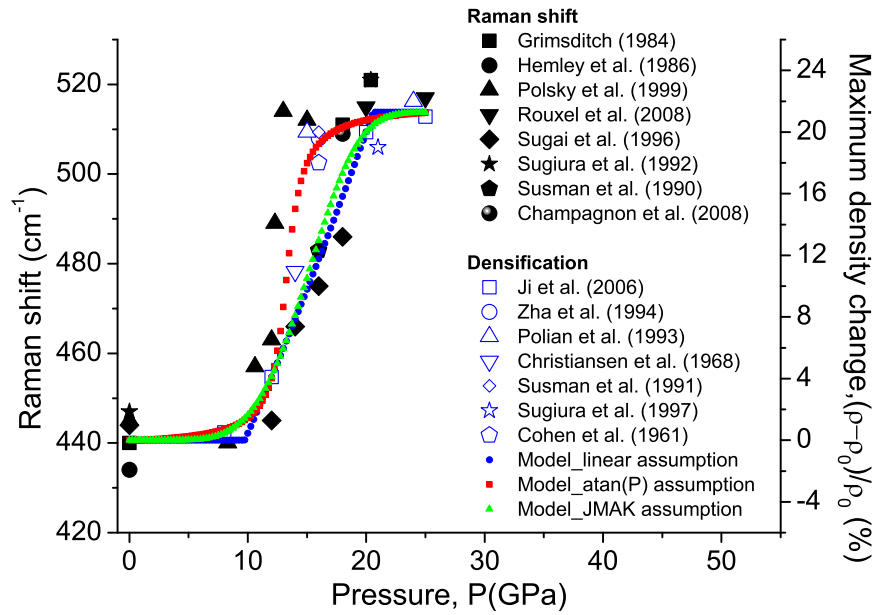


Figure 2.58 Hydrostatic Pressure Case: Densification and Raman shift change with pressure.

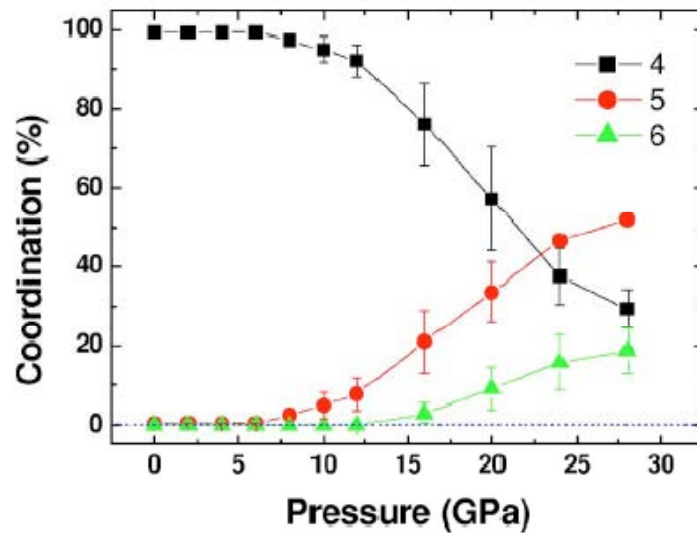


Figure 2.59 Percentages of Si atoms coordinated four (squares), five (circles), and six (triangles), to oxygen. The cutoff distance for coordination was set to 2.1 Å and error bars were evaluated by changing the cutoff distance by  $\pm 0.1$  Å. [Liang 2007]

● Summary

All in all, our model can simulate the densification phenomenon under hydrostatic pressure and predicts the changes of densification, the changes in elastic properties and Poisson's ratio with pressure. The main achievements as below:

- i) Establish a new constitutive equation to portray the densification behavior of silica under hydrostatic pressure. Proposed three linear, atan(P) and JMAK hardening rule to portray the densification induced permanent hardening.
- ii) Succeed in executing reverse analysis and get the characteristic parameters, as shown in table 2.9. Densification versus pressure process for loading and unloading all show good agreement to the experimental data both in in-situ and ex-situ case.

Table 2.9 Reverse analysis results.

	P <sub>0</sub> (GPa)	P <sub>1</sub> (GPa)	Residual	γ (%)	B <sub>max</sub> (GPa)	G <sub>max</sub> (GPa)
Linear Simulation	9.7	20.6	30.9	21.3	74.4	43.7
Atan(P) Simultaion	1.0	20.2	50.9	21.3	74.4	43.7
JMAK Simulation	3.0	25.0	5.9	21.3	74.4	43.7
Ji's EXP	~8	~20		20~21	73.3	43.5
Wakabayashi				21	75.4	

- iii) Assume there is a linear relationship of bulk modulus and shear modulus to densification. We get the permanent bulk modulus, shear modulus and Young's modulus after fully densified. Those data all fit experimental data very well.
- iv) The predictions of elastic modulus during the loading and unloading process present a discrepancy for bulk modulus between simulation and experimental data.
- v) Predict the changes of Poisson's ratio basing the classic elastic formulation  $\nu = \frac{3B - 2G}{6B + 2G}$ , get the permanent value of Poisson's ratio about 0.255 after fully densified, which fit Ji's data but higher than Zha's value.
- vi) Pointing out the permanent densification has a linear relationship with the Raman shift in silica under high pressure. Furthermore, we proposed that the permanent densification may be induced by the permanent increase of six-fold coordination rings in silica under high pressure.

## References

- 1) [Arndt 1969] J. Arndt. *Effect of impurities on densification of silica glass*. J. Am. Ceram. Soc. **52**, 285 (1969).
- 2) [Benmore 2010] C. J. Benmore, E. Soignard, S. A. Amin, M. Guthrie, S. D. Shastri, P. L. Lee, and J. L. Yarger. *Structural and topological changes in silica glass at pressure*. Phys. Rev. **B**, 81, 054105 (2010).
- 3) [Bridgman 1953] P. W. Bridgman, and I. Simon. *Effects of very high pressures on glass*. J. Appl. Phys., **24**, 405 (1953).
- 4) [Christiansen 1962] E. B. Christiansen, S. S. Kistler, and W. B. Gogarty. *Irreversible compressibility of silica glass as a means of determining the distribution of force in high-pressure cells*. J. Amer. Ceram. Soc., **45**, 172 (1962).
- 5) [Cohen 1961] H. M. Cohen, and R. Roy. *Effects of ultrahigh pressure on glass*. J. Amer. Ceram. Soc., **44**, 523 (1961).
- 6) [Cohen 1962] H. M. Cohen, and R. Roy. *Reply to “comments on ‘Effects of ultrahigh pressure on glass’ ”*. J. Am. Ceram. Soc., **45**, 398 (1962).
- 7) [Deschamps 2011] T. Deschamps, C. Martinet, J. L. Bruneel and B. Champagnon. *Soda-lime silicate glass under hydrostatic pressure and indentation: a micro-Raman study*. J. Phys : Condens. Mater, **23**, 035402 (2011).
- 8) [Forest 1994] S. Forest, and P. Pilvin. *Large deformation of solids with microstructure*. Internal report ENSMP (1994).
- 9) [Forest 1999] S. Forest, and P. Pilvin. *Modelling finite deformation of polycrystals using local objective frames*. Z. Angew. Math. Mech., **79**, 199 (1999).
- 10) [Gadelrab 2012] K. R. Gadelrab, F. A. Bonilla, M. Chiesa. *Densification modeling of fused silica under nanoindentation*. J. Non-cry. Solids, **358**, 392 (2012).
- 11) [Giannakopoulos 1997] A. E. Giannakopoulos, P. L. Larsson. *Analysis of indentation of pressure-sensitive hard metals and ceramics*. Mech. Mater., **25**, 1-35 (1997).
- 12) [Grimasditch 1984] M. Grimasditch. *Polymorphism in amorphous SiO<sub>2</sub>* Phys. Rev. Lett., **52**, 2379 (1984).
- 13) [Hill 1950] R. Hill. *The mathematical theory of plasticity*. (Oxford: Oxford University press; 1950).
- 14) [Huang 2004] L. P. Huang, and J. Kieffer. *Amorphous-amorphous transitions in silica glass. II. Irreversible transitions and densification limit*. Phys. Rev. B, **69**,

- 224204 (2004).
- 15) [Ji 2007] H. Ji. *Mecanique et physique de l'indentation du verre*. Thesis, Devant l'Universite de Rennes 1, No d'ordre: 3686 (2007).
  - 16) [Katayama 2005] Y. Katayama, Y. Inamura. *Structure studies on liquids and glass under high pressure and high temperature*. Nuclear Instruments and Methods in Physics Research B, **238**, 154 (2005).
  - 17) [Kermouche 2008] G. Kermouche, E. Barthel, D. Vandembroucq, P. Dubujet. *Mechanical modeling of indentation-induced densification in amorphous silica*. Acta Mater., **56** 3222 (2008).
  - 18) [Lambropoulos 1996] J. C. Lambropoulos, S. Xu, and T. Fang. *Constitutive law for the densification of fused silica, with applications in polishing and microgrinding*. J. Am. Ceram. Soc., **79** [6], 1441 (1996).
  - 19) [Lemaitre 1996] J. Lemaitre, J-L Chaboche. *Mechanics of Solid Materials*. (Cambridge: Cambridge University Press; 1996).
  - 20) [Liang 2007] Y. Liang, C. R. Miranda, and S. Scandolo. *Mechanical strength and coordination defects in compressed silica glass: Molecular dynamic simulations*. Phys. Rev. B, **75**, 024205 (2007).
  - 21) [Mackenzie 1963a] J. D. Mackenzie. *High-pressure effects on oxide glasses: I, Densification in rigid state*. J. Amer. Ceram. Soc., **46**, 461 (1963).
  - 22) [Mackenzie 1963b] J. D. Mackenzie. *High-pressure effects on oxide glasses: II, Subsequent heat treatment*. J. Amer. Ceram. Soc., **46**, 470 (1963).
  - 23) [Meade 1987] C. Meade, and R. Jeanloz. *Frequency-dependent equation of state of fused silica to 10 GPa*. Phys. Rev. B, **35**, 236 (1987).
  - 24) [Meade 1992] C. Meade, R. J. Hemley, and H. K. Mao. *High-pressure x-ray diffraction of SiO<sub>2</sub> glass*. Phys. Rev. Lett., **69**, 1387 (1992).
  - 25) [Murakami 2010] M. Murakami, and J. D. Bass. *Spectroscopic evidence for ultrahigh-pressure polymorphism in SiO<sub>2</sub> glass*. Phys. Rev. Lett., **104**, 025504 (2010).
  - 26) [Perriot 2006] A. Perriot, D. Vandembroucq, and E. Barthel, V. Martinez, L. Grosvalet, C. Martinet, and B. Champagnon. *Raman microspectroscopic characterization of amorphous silica plastic behavior*. J. Am. Ceram, Soc., **89** [2] 596 (2006).
  - 27) [Peter 1970] K. W. Peter. *Densification and flow phenomena of glass in indentation experiments*. J. Non-Cryst. Solids, **5**, 103 (1970).
  - 28) [Polian 1993] A. Polian, and M. Grimsditch. *Sound velocities and refractive index*

- of densified  $\alpha$ -SiO<sub>2</sub> to 25 GPa*. Phys. Rev. B, **47**, 13979 (1993).
- 29) [Rouxel 2008] T. Rouxel, H. Ji, T. Hammouda, and A. Moréac. *Poisson's ratio and the densification of glass under high pressure*. Phys. Rev. Lett., **100**, 225501 (2008).
  - 30) [Rouxel 2010] T. Rouxel, H. Ji, J. P. Guin, F. Augereau, and B. Rufflé. *Indentation deformation mechanism in glass: densification versus shear flow*. J. Appl. Phys., **107**, 094903 (2010).
  - 31) [Roy 1961] R. Roy, and H. M. Cohen. *Effects of high pressure on glass: a possible piezometer for the 100-kilobar region*. Nature, **190**, 798 (1961).
  - 32) [Sampath 2003] S. Sampath, C. J. Benmore, K. M. Lantzky, J. Neuefeind, K. Leinenweber, D. L. Price, and J. L. Yarger. *Intermediate-range order in permanently densified GeO<sub>2</sub> glass*. Phys. Rev. Lett., **90**, 115502, (2003).
  - 33) [Sato 2008] T. Sato, and N. Funamori. *Sixfold-coordinated amorphous polymorph of SiO<sub>2</sub> under high pressure*. Phys. Rev. Lett., **101**, 25502 (2008).
  - 34) [Sato 2010] T. Sato, and N. Funamori. *High-pressure structural transformation of SiO<sub>2</sub> glass up to 100 GPa*. Phys. Rev. B, **82**, 184102 (2010).
  - 35) [Sato 2011] T. Sato, N. Funamori, and T. Yagi. *Helium penetrates into silica glass and reduces its compressibility*. Nature Commun., **2**, 345 (2011).
  - 36) [Sugiura 1997] H. Sugiura, R. Ikeda, K. Kondo, and T. Yamadaya. *Densified silica glass after shock compression*. J. Appl. Phys., **81** (4), 1651 (1997).
  - 37) [Valle 1996] R. G. D. Valle, and E. Venuti. *High-pressure densification of silica glass: A molecular-dynamics simulation*. Phys. Rev. B, **54**, 3809 (1996).
  - 38) [Wakabayashi 2011] D. Wakabayashi, N. Funamori, T. Sato, and T. Taniguchi. *Compression behavior of densified SiO<sub>2</sub> glass*. Phys. Rev. B, **84**, 144103 (2011).
  - 39) [Weir 1962] C. E. Weir, and S. Spinner. *Comments on "Effects of ultrahigh pressure on glass"*. J. Am. Ceram. Soc., **45**, 196 (1962).
  - 40) [Xin 2000] K. Xin, and J. C. Lambropoulos. *Densification of fused silica: effects on nanoindentation*. Proc. SPIE., **4102**, 112 (2000).
  - 41) [Xin 2003] K. Xin, and J. C. Lambropoulos. *Spherical cavity expansion in densifying material*. J. App. Phys., **94**, 6437 (2003)
  - 42) [Yasui 1982] I. Yasui, and M. Imaoka. *Finite element analysis of indentation on glass (II)*. J. Non-Cryst. Solids, **50**, 219 (1982).
  - 43) [Zha 1994] C. S. Zha, R. J. hemley, H. K. Mao, T. S. Duffy, and C. Meade. *Acoustic velocities and refractive index of SiO<sub>2</sub> glass to 57.5 GPa by Brillouin scattering*. Phys. Rev. B **50**, 13105 (1994).

- 44) [Zeng 1995] K. Zeng, A. E. Giannakopoulos, and D. J. Rowcliffe. *Vickers indentations in glass-II. Comparison of finite element analysis and experiments*. Acta Metall. Mater., **43**, 1945 (1995).



# Conclusion

High pressures induce permanent densification in inorganic glasses, such as amorphous silica, silicate glasses, boric oxide glass, germinate glasses, chalcogenide and chalcogen halide glasses, and bulk metallic glasses. Different kinds of glasses have different atomic packing densities, different atomic coordination numbers, hence, present different densification behavior and various maximum values of densification under high pressure at room temperature. However, there remain unknowns and controversies in this special field.

In order to understand the deformation behavior of silica under high pressure, we have reviewed carefully for the abounded literatures. In general, the densification behavior of silica may be depicted as follows:

- i) There is a threshold pressure around 8-10 GPa where densification happens.
- ii) Density increases with the increase in pressure up to 20~25 GPa to reach a saturation value of densification about 20~21%.
- iii) During the densification process, the elastic properties, such as bulk modulus, shear modulus, and Young's modulus, increase.
- iv) Si atomic coordination number changes with pressures from 4 to 6 during the compression process.

Permanent densification in silica is uneasy to investigate via unconstrained macroscopical testing (such as the compression test) because of the material brittleness. We have developed a constitutive framework to model the response of silica glass under hydrostatic compression with pressures up to 25 GPa. This model is based on relevant series of experimental data and takes into account the progressive densification process that exists in between two threshold pressures, the onset of densification and its saturation. In addition, we consider the changes in elastic parameters with densification. The material parameters involved in this model have been determined straightforwardly from *ex situ* experimental from Ji and Rouxel et al. [Ji 2007, Rouxel 2010].

The model has been implemented in a finite-element software to simulate the hydrostatic compression. Our results are compared with the *ex situ* experimental data and *in situ* experimental data. (*In situ* data from Sato and Wakabayashi et al. [Sato

2008, Sato 2010, Wakabayashi 2011]) Three different hardening rules (one linear hardening and two non-linear hardening laws) are used in our simulation. Reverse analysis is employed to identify some parameters of the models.

All in all, our model succeeds in simulating the densification phenomenon under hydrostatic pressure and predicting the changes in densification, the changes in elastic properties and Poisson's ratio with pressure. Densification increases with high pressures after a threshold and then reaches a saturation value of 21.3% around 20 GPa. Bulk modulus, shear modulus increase with pressure, and reach maximum values about 74.4 GPa and 43.7 GPa, respectively. As for Young's modulus, it reaches 108 GPa while Poisson's ratio reaches level of 0.25. Furthermore, we found the relationship between Raman shift and densification. It may conclude that the key to control densification is the inherent Si atom coordination numbers changes with high pressures.

This constitutive framework, restricted to the sole pressure, is expected to pave the way for future developments where pressure plays a major role but is not the sole actor. The incidence of an adequate modeling of densification process triggered by pure pressure, as it proposed in this work, on constrained deformation modes, such as surface damage, is a next natural step.

- 1) [Ji 2007] H. Ji. *Mecanique et physique de l'indentation du verre*. Thesis, Devant l'Universite de Rennes 1, No d'ordre: 3686 (2007).
- 2) [Rouxel 2010] T. Rouxel, H. Ji, J. P. Guin, F. Augereau, and B. Rufflé. Indentation deformation mechanism in glass: densification versus shear flow. *J. Appl. Phys.*, **107**, 094903 (2010).
- 3) [Sato 2008] T. Sato, and N. Funamori. *Sixfold-coordinated amorphous polymorph of SiO<sub>2</sub> under high pressure*. *Phys. Rev. Lett.*, **101**, 25502 (2008).
- 4) [Sato 2010] T. Sato, and N. Funamori. *High-pressure structural transformation of SiO<sub>2</sub> glass up to 100 GPa*. *Phys. Rev. B*, **82**, 184102 (2010).
- 5) [Wakabayashi 2011] D. Wakabayashi, N. Funamori, T. Sato, and T. Taniguchi. *Compression behavior of densified SiO<sub>2</sub> glass*. *Phys. Rev. B*, **84**, 144103 (2011).

## Résumé

Le comportement à haute pression du verre de silice a été largement étudié dans de différents domaines pour ses propriétés mécanique et physiques, tels que la mécanique non-linéaire, la physique de haute pression, la physique non-cristalline, la physique appliquée, la géophysique, etc. La densification permanente est la propriété la plus fondamentale obtenue à partir de la haute pression. Nous discutons un modèle constitutif décrivant le mécanisme de déformation permanente par la densification sous haute pression de verre de silice. La loi de comportement proposée dans cette étude considère que la pression est hydrostatique pure. Elle est composée d'une partie élastique et d'autre partie un écoulement décrivant l'évolution des déformations permanentes après l'initiation de la densification. Dans cette loi, trois critères d'écrouissage sont discutés à l'égard de la dépendance de la densification incrémentale (*progressive*) aux niveaux de contraintes appliquées. Les mesures expérimentales ex-situ et in-situ sont utilisées pour évaluer notre modèle. En misant en œuvre de notre modèle dans Abaqus et SiDoLo (corotational logiciel), l'analyse inverse est utilisée pour déterminer le seuil de la pression de densification, la pression à la saturation et le taux de densification saturée. Les calculs numériques montrent un excellent accord avec les données expérimentales. Il est à noter que notre modèle non seulement réussit à déterminer les propriétés de densification, mais aussi pour prédire les changements de propriétés élastiques, telles que le module de compressibilité, le module de cisaillement, module d'élasticité et le coefficient de Poisson, sous la pression hydrostatique. Dans les perspectives, notre modèle fournit une nouvelle loi pour analyser le comportement à la déformation de silice sous l'état de contraintes complexes.

## Mots clés:

Verre, Déformation, Densification, Haute pression, Mécanisme, Méthode des éléments finis

## Abstract

High-pressure behavior of  $\text{SiO}_2$  glass has been studied extensively because it has attracted considerable attention in various fields of mechanical and physical sciences, such as non-linear mechanics, high-pressure physics, noncrystalline physics, applied physics, geophysics, etc. Permanent densification is the most fundamental property obtained from very high pressure. We discussed a constitutive model which describing the permanent densification induced deformation mechanism of silica. The constitutive law is assumed to be pure hydrostatic pressure, and uses a yield function and a flow rule describing the evolution of permanent strains after initial densification, and three hardening rules discussing the dependence of the incremental densification on the levels of applied stresses. Ex-situ and in-situ experiments are both considered to evaluate our model. Implementing our model to a finite software Abaqus and a corotational framework software SiDoLo, inverse analysis is used to determine the threshold densification pressure, the saturate densification pressure and the saturate value of densification. Numerical results show an excellent agreement to experimental data. It should be noted that our model not only succeeding in determine the densification properties, but also in predicting the changes of elastic properties, such as Bulk modulus, Shear modulus, Young's modulus and Poisson's ratio, under hydrostatic pressure. Seen in perspective, our model provides a new rule to analyze the deformation behavior of silica under complex stress states.

## Key words:

Glass, Deformation, Densification, High pressure, Mechanism, Finite element method